12-2017

USArray Imaging of North American Continental Crust

Xiaofei Ma
Utah State University

USARRAY IMAGING OF NORTH AMERICAN CONTINENTAL CRUST

by

Xiaofei Ma

A dissertation submitted in partial fulfillment
of the requirements for the degree

of

DOCTOR OF PHILOSOPHY

in

Geology

Approved:

_____ Anthony R. Lowry, Ph.D. Major Professor	_____ James P. Evans, Ph.D. Committee Member
_____ John W. Shervais, Ph.D. Committee Member	_____ Susanne U. Jänecke, Ph.D. Committee Member
_____ James A. Bay, Ph.D. Committee Member	_____ Mark McLellan, Ph.D. Vice President for Research and Dean of the School of Graduate Studies

UTAH STATE UNIVERSITY
Logan, Utah

2017

ABSTRACT

USArray Imaging of North American Continental Crust

By

Xiaofei Ma, Doctor of Philosophy

Utah State University, 2017

Major Professor: Dr. Anthony R. Lowry
Department: Geology

The layered structure and associated bulk composition of continental crust contains important clues about the tectonic evolution and modern dynamics of continental lithosphere. Gravity anomalies, surface elevation, large-scale deformation and lithospheric strength are all directly related to these crustal properties. The North America continental crust records billions of years of continental evolution, including accretion, break-up and modification by magmatism and volatile flux processes. Mobile lithosphere of the western United States has experienced a diversity of dynamic processes including hotspot modification, shortening and back-arc extension related to Farallon subduction, and accretion and translation of terranes along a transform boundary. The eastern U.S. is relatively stable and preserves a record of multiple cycles of continental collision and breakup as the type-locality for Wilson cycle tectonism. This project images North America's continental crust using data collected by

EarthScope's USArray, the FlexArrays and regional seismic networks across the continental United States. Here I improve upon a methodology for joint inversion of Bouguer gravity anomalies and seismic receiver functions by using parameter-space stacking of cross-correlation coefficients of synthetic and observed receiver functions instead of standard H-κ amplitude stacking. The new method is applied to estimate thickness and seismic velocity ratio of the bulk continental crust as well as separately for upper and lower crustal layers. Thicknesses of both the one-layer and two-layer models are reasonably consistent with results from other studies and exhibit interesting relationships with the physiographic and basement provinces of North America. Seismic velocity ratios, v_P/v_S, derived from this method are more consistent with lab experiment results than from other approaches, and hint at large-scale variations in composition of continental crust including very low v_P/v_S in the lower crust under the mountainous western U.S. Cordillera. Seismic velocity ratios of the lower crust in the central and eastern U.S. average ~0.15 to 0.2 higher than those in the western United States. To interpret the results, I model the pressure/temperature-dependent thermodynamics of mineral formation for various major-element crustal chemistries, with and without volatile constituents. My results suggest that hydration lowers bulk crustal v_P/v_S and density, and releases heat in the shallow crust but absorbs heat in the lowermost crust. The mid-crustal impedance boundary may represent a change in bulk chemistry rather than a phase boundary. Simulations of the conductive thermal response to temperature changes caused by hydration reactions suggest that perturbations in surface heat flow and Moho temperature would subside by ~15–20 Myr, suggesting that modern observed discrepancies require either continuing hydration or an additional contribution from advection of heat by

volatile or melt flux. Therefore, I hypothesize that small amounts of post-Laramide partial melt may remain in the lower crust of the western U.S. Cordillera, resulting from hydration and high lithospheric temperature. Advection of these melts contributes to high surface heat flow and consumption of lower crustal garnets by melting may contribute up to ~400 m of the total post-Laramide uplift.

(205 pages)

PUBLIC ABSTRACT

USArray Imaging of North American Continental Crust

Xiaofei Ma

The layered structure and bulk composition of continental crust contains important clues about its history of mountain-building, about its magmatic evolution, and about dynamical processes that continue to happen now. Geophysical and geological features such as gravity anomalies, surface topography, lithospheric strength and the deformation that drives the earthquake cycle are all directly related to deep crustal chemistry and the movement of materials through the crust that alter that chemistry.

The North American continental crust records billions of years of history of tectonic and dynamical changes. The western U.S. is currently experiencing a diverse array of dynamical processes including modification by the Yellowstone hotspot, shortening and extension related to Pacific coast subduction and transform boundary shear, and plate interior seismicity driven by flow of the lower crust and upper mantle. The midcontinent and eastern U.S. is mostly stable but records a history of ancient continental collision and rifting.

EarthScope's USArray seismic deployment has collected massive amounts of data across the entire United States that illuminates the deep continental crust, lithosphere and deeper mantle. This study uses EarthScope data to investigate the thickness and composition of the continental crust, including properties of its upper and lower layers. One-layer and two-layer models of crustal properties exhibit interesting relationships to the history of North

American continental formation and recent tectonic activities that promise to significantly improve our understanding of the deep processes that shape the Earth's surface. Model results show that seismic velocity ratios are unusually low in the lower crust under the western U.S. Cordillera. Further modeling of how chemistry affects the seismic velocity ratio at temperatures and pressures found in the lower crust suggests that low seismic velocity ratios occur when water is mixed into the mineral matrix, and the combination of high temperature and water may point to small amounts of melt in the lower crust of Cordillera.

ACKNOWLEDGMENTS

When I came to Utah State University five years ago as an international student with a physics background, the change to a graduate life studying geophysics was a little tough for me at the beginning. Here I want to thank the faculty and staff of the Department of Geology for all the help they've given during my graduate studies. I am grateful to Joel Pederson and Tammy Rittenour for their guidance in progress of my studies program. Thanks also to the accounting department for helping with all of my tax paperwork each year, and to the IT department for patiently solving my computing problems. Thanks to all of my friends for helping to take care of me when I tore my Achilles tendon. I have enjoyed my Ph.D. life here in Logan.

I want to express my great thanks to my committee, John Shervais, James Evans, Susanne Jänecke and Jim Bay for their support and discussion to guide my studies here. I especially thank my advisor, Tony Lowry. I always felt free to bug him whenever I had any thoughts or questions, whether for my research or other questions. He always patiently answered all of my questions and carefully edited all of my papers. I know how painful it is to edit a paper written by a non-native English speaker since I also occasionally helped with editing the English in papers by my friends from China. I also want to thank Ravi Kanda for help me to code my crustal thermal model.

My research was supported by National Science Foundation grants EAR-0955909, EAR-1246977, and EAR-1358622 from the Geophysics and EarthScope science programs.

Lastly, I want to thank my parents. Their support and encouragement were always there when I needed it. I am lucky to have all of them in my life.

Xiaofei Ma

CONTENTS

LIST OF TABLES

LIST OF FIGURES

GLOSSARY OF ACRONYMS

AH	Appalachian Highlands
B&R	Basin and Range
CB	Cheyenne Belt
CP	Columbia plateau
EARS	EarthScope Automated Receiver Survey
GF	Grenville Front
IP	Interior Plains
Mz	Mazatzal Province
OI	Optimal Interpolation
RGR	Rio Grande rift
SRM	Southern Rocky Mountains
SRP	Snake River plain
TH	Trans Hudson orogen
Yv	Yavapai Province

CHAPTER 1

1.1 Introduction

The Earth is unique in our solar system as having both continents and plate tectonics. Tectonism and deformation affects climate, hazards, and many other aspects of life on Earth. Plate tectonics conceptualizes the lithosphere, a strong outer shell of the Earth, as broken into several dozen plates that move in different directions over a weaker, ductile asthenosphere. The relative motion of the plates builds mountains, causes rifting, and drives earthquake and volcanic activity at the plate boundaries, and classically has been conceptualized as driven by negative thermal buoyancy of subducted slabs and positive thermal buoyancy of mid-ocean ridges (Forsyth & Uyeda, 1975).

To fully understand the continental crust and lithosphere, one needs to address how it forms and how it evolves through geological history. The continental crust of North America consists largely of Archean and Proterozoic continental lithosphere which is collectively called cratonic. Most of the North American craton has been relatively stable through the Phanerozoic, and seismic imaging shows relatively high velocities (interpreted as lower temperatures) to depths of more than 200 km (Artemieva & Mooney, 2002) collocated with layered anisotropy directions that do not match plate motion directions as observed in deeper asthenospheric mantle (Yuan & Romanowicz, 2010).

Continental crust forms from cooling and fractionation of melts derived from the underlying mantle, but some processes of mass flux from the mantle to the crust

are enigmatic—particularly those relating to volatile transfer. Some recent studies infer that surface tectonism of the western U.S. Cordillera has been significantly influenced by hydration processes that occurred during flat-slab subduction of the Farallon oceanic plate during late Cretaceous (Humphreys et al., 2003; Jones et al., 2015), but the processes by which volatiles are transferred from the mantle up through the lithospheric column are hotly debated. The nature of buoyancy responsible for Cenozoic uplift and modern elevation of the western U.S. Cordillera is also debated, with some calling on primarily thermal support (e.g., Roy et al., 2009; Hyndman & Currie, 2011) and others invoking buoyancy related to hydration processes (Porter et al., 2012; Jones et al., 2015). Some fraction of surface elevation is supported by asthenospheric mantle buoyancy (Becker et al*.,* 2014*;* Lowry et al*.,* 2000), but there also it is unclear how much of the buoyancy variation is related to temperature versus composition or hydration state.

With the explosion of computing capabilities and collection of large data sets from EarthScope, our knowledge of the Earth has changed dramatically over the past decade. The dense sampling of a 3D continental transect by EarthScope's Transportable Array makes it possible to image comprehensively the Earth's interior. Joint inversion of related types of geophysical data greatly reduces the uncertainty associated with modeling parameters and increases resolution of deep Earth images. An important research goal of the geosciences is to understand the dynamics of geophysical processes of the solid Earth well enough to create

numerical models that have predictive power, analogous to e.g. weather models of the atmosphere.

Figure 1: Geological map of North America. Geological basement terranes that have assembled to form the North American continent (from Whitmeyer & Karlstrom, 2007).

1.2 Tectonic Background of North America

The goal of modeling multiple-layer crustal thickness and composition is to better understand active lithospheric processes and past evolution of the continent. Surface geological features also provide clues to tectonic history, including useful information about deeper crustal structure and composition. North America was assembled from a core of three Archean cratonic shields (all formed before 2.5 Ga) with peripheral accretion of Proterozoic belts (Figure 1) (Whitmeyer & Karlstrom, 2007). The 1.85–1.78 Ga collision of the two oldest Archean blocks, the Wyoming and Superior provinces, formed the Trans-Hudson orogenic belt (Hoffman, 1988). During the Paleoproterozoic, the core of the continent progressively grew to the southeast with accretion of juvenile volcanic arcs and oceanic terranes. The northeast-trending Yavapai province welded to Laurentia between 1.71–1.68 Ga, followed by addition of the Mazatzal province between 1.65–1.60 Ga. The Grenville province was added to North America between 1.3–1.0 Ga (Whitmeyer & Karlstrom, 2007). Final assembly of Rodinia occurred with accretion of the Grenville province, accompanied by voluminous mafic magmatism and formation of the Midcontinent rift (Green, 1983). The Midcontinent rift is expressed now primarily as a lineament of strong gravity and magnetic anomalies in the midcontinent region, with basalts and mafic intrusives exposed only in the northern Great Lakes region (Green, 1983; Green et al., 1989).

Another interesting and poorly understood region is the Tennessee-Indiana-Kentucky lineament or TIKL (Ravat, 1985), stretching northwest-southeast for ~400

km from St. Louis, Missouri, to central Tennessee. It has been suggested that the Laurentian proto-continent may have attempted to separate at this site after accretion of the Eastern Granite-Rhyolite province and prior to accretion of the Grenville Province at 1.1 Ga (Ravat, 1984). The northwest-trending TIKL is characterized by a ~400 km-long linear zone of magnetic anomalies starting at the Grenville front and terminating near the 1.55 Ga mid-Proterozoic boundary. Portions of the magnetic anomaly signature are inversely correlated with gravity anomalies (Ravat, 1984).

The Appalachian orogen formed over the course of a complete Paleozoic Wilson cycle. The early stage of the Wilson cycle corresponded to the breakup of Rodinia at the eastern margin of Laurentia, creating the Iapetus Ocean (Mac Niocaill et al., 1997). This was followed by subduction of the western Iapetus beneath an island arc at an ocean-ocean boundary and eventual closure of the ocean basin by collision of Laurentia with the island arcs and Gondwana, forming the Appalachian orogeny and Pangea (Hatcher, 2010; Bally et al., 1989). At the beginning of the Mesozoic, the Pangean supercontinent rifted and subduction of the oceanic Farallon and Kula plates began beneath western North America (Haeussler, 2003).

There are two main orogenic events associated with Farallon subduction. The Sevier orogeny occurred from middle Jurassic to Eocene and was characterized by thin-skinned thrust deformation postulated to have formed an orogenic plateau analogous to the modern Andes (Armstrong, 1972). The Laramide orogeny, from late Cretaceous to early Paleocene, deformed the crust as much as 1500 km inland

from the active plate boundary, reaching as far inland as the Great Plains states (Bird, 1984). Several models have been hypothesized to explain this extremely widespread, thick-skinned continental deformation event. The most likely suggests that the angle of subduction of the Farallon slab shallowed, resulting in a “flat slab” that interacted with the base of the North American lithosphere and deformed the crust to distances very far from the plate boundary (Bird, 1998; Humphreys, 2003). Thick-skinned thrust faulting and folding related to the Laramide event is observed from southern Montana and western South Dakota south to New Mexico (Tikoff & Maxson, 2001). These features are subtle when compared to the coeval Cordilleran fold and thrust belt to the west, and occur in the Colorado Plateau and Great Plains from South Dakota to Texas. Monoclinal folding over smaller-offset, basement-involved thrusts are the main structure of this Laramide province.

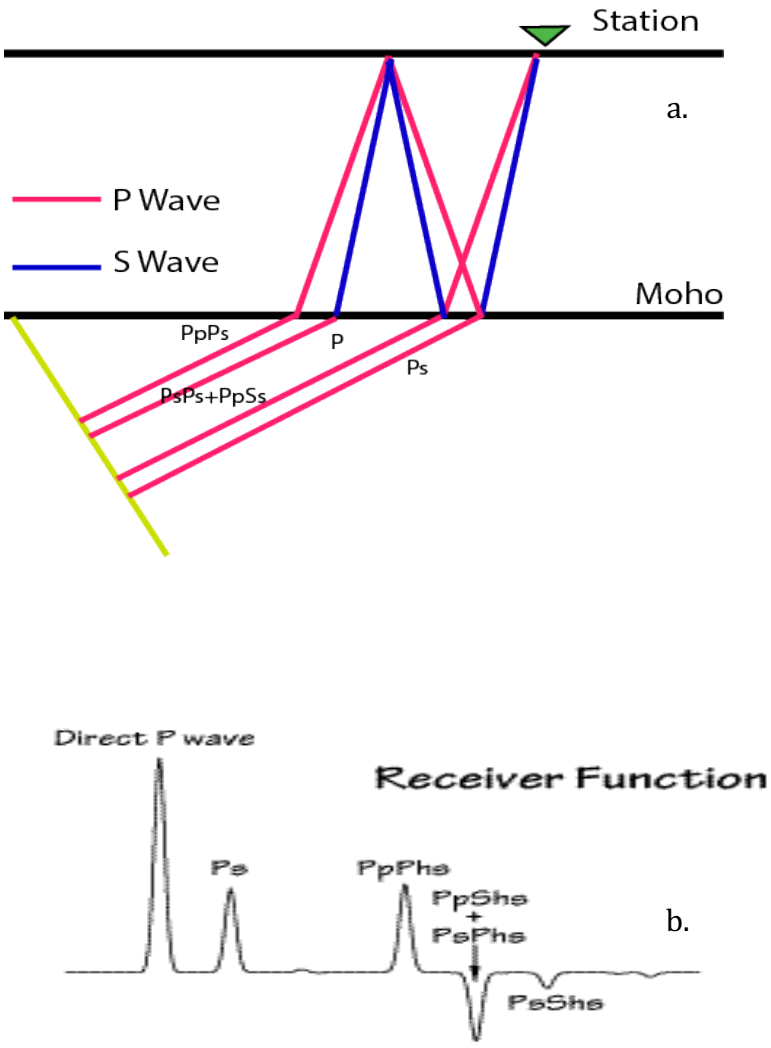

Figure 2: Illustration of seismic receiver functions. (a): Sketch of seismic ray paths that contribute to a receiver function generated by a mantle P wave arrival at the Moho. Ps denotes a seismic P wave converted to an S wave at the Moho seismic impedance boundary. (b): Example of a seismic receiver function with phase arrivals corresponding to the travel paths shown on top (after Ammon et al., 1990).

1.3 Overview of Receiver Function Imaging

Seismic receiver functions are widely used for passive-source imaging of impedance structure of the crust, lithosphere and mantle transition zone. The theory was first developed by Phinney (1964) and expanded over the next few decades (Burdick & Langston, 1977; Vinnik, 1977; Langston, 1979). Two types of receiver functions are commonly used: P receiver functions (used in this project) and S receiver functions, corresponding to the original incoming wave from the mantle. The P waves that travel through the mantle from an angular distance greater than 30° typically split into transmitted P and converted Ps phases at large impedance boundaries that arrive at the surface at different times. These also can reflect off the surface and Moho impedance boundaries resulting in later arrivals such as PpPs, PsPs, and PpSs phases, called reverberations. The arrival time difference between the P, Ps and the reverberations can be used to estimate crustal thickness and v_P/v_S (Zhu et al., 2000; Andrews & Deuss, 2008; Levander & Miller, 2012).

Receiver functions are Earth impulse response functions derived from seismic records. Modern broadband seismometers record seismic waves in three components corresponding to the vertical, north-south and east-west directions. For receiver function analysis, the horizontal components of motion are transformed to radial (i.e., in the direction from the earthquake source to the station) and tangential directions. The waveform $D(t)$ in each component can be represented as a time-domain convolution of the instrument's impulse response, $I(t)$; a source-time function, $S(t)$; and the impulse response due to Earth impedance structure, $E(t)$; via:

$$D_V(t) = I(t) * S(t) * E_V(t)$$
$$D_R(t) = I(t) * S(t) * E_R(t)$$
$$D_T(t) = I(t) * S(t) * E_T(t) \qquad (1.1)$$

where subscripts *V, R,* and *T* represent the vertical, radial and tangential components respectively. At large source-receiver distances, body waves propagate nearly vertically, so the P arrival is expressed mostly in the vertical component whereas Ps and the reverberations have negligible vertical motion. Hence the vertical component $D_V(t)$ approximates $I(t)*\delta(t)*S(t)$ where $\delta(t) = E_V(t)$ is an impulse response or "delta function" at the time of arrival of the P phase. Thus, the radial response to Earth impedance structure can be calculated by deconvolving the vertical from the radial waveform in the frequency domain using:

$$E_R(\omega) = \frac{D_R(\omega)\overline{D}_V(\omega)}{\varphi(\omega)} G(\omega) \qquad (1.2)$$

$$\varphi(\omega) = \max\left\{D_V(\omega)\overline{D}_V(\omega), C\right\} \qquad (1.3)$$

where the overbar denotes a complex conjugate, *C* is a water-level to dampen numerical singularity associated with near-zero amplitudes of the vertical component, and $G(\omega)$ is a Gaussian filter to simulate the expectation operator and reduce noise. $E_R(\omega)$ calculated in this manner is the radial P wave receiver function. The P wave receiver function for a single layer over a half space is expected to show three impulsive phase arrivals following the initial *P* arrival, which are conventionally denoted Ps, PpPs, PpSs+PsPs (with propagation paths depicted in Figure 2).

The receiver function represents the arrival times of S waves generated by mode conversions and reverberations at large impedance contrasts, so these times are sensitive primarily to the thicknesses and velocities of layers that the seismic phases traveled through. Amplitudes depend only on the impedance change in a 1D isotropic Earth, but dipping layer boundaries or anisotropic layering can change the amplitude or even the sign of receiver functions from different azimuths (Schulte-Pelkum & Mahan, 2014), which complicates interpretation. The analyses in this dissertation assume 1D, isotropic crustal layering under each seismic station. Also, receiver functions generate an impulse response at every boundary with strong impedance contrast, so I tested the effect of an unconsolidated soil layer on synthetic receiver functions. Soils typically have a high Poisson's ratio, and in Figure 3 I modeled synthetic crustal seismic receiver functions that assume soil layer thicknesses of 50 and 400 m (Pelletier et al., 2016; James Bay, personal communication, 2017) with v_P/v_S = 3.25 (v_P = 1500 m/s, v_S = 400 m/s and density 1700 kg/m^3, which is representative for saturated unconsolidated soil (Mavko, 2017)). The presence of a soil layer noticeably increases the amplitude of arrivals and decreases signal to noise level. Crustal thickness and v_P/v_S are determined from the time difference between the direct P arrival and later arrivals, and in the example shown these changes are less than 2%. However, most broadband stations (including TA sites) designed for deep seismic imaging are either sited on bedrock or installed in boreholes at depths of several meters or more, to minimize the effects of shallow reverberations in the data.

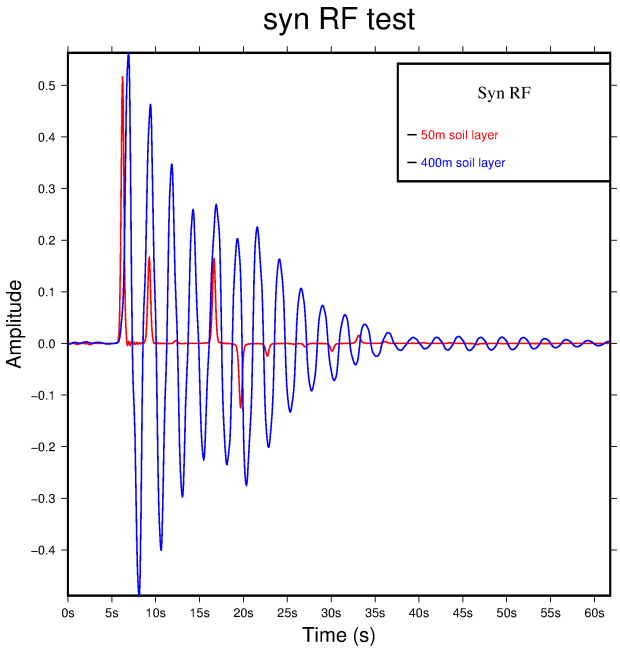

Figure 3: Synthetic receiver functions with and without an unconsolidated soil layer. Red curve is the receiver function including a 50 m unconsolidated soil layer; blue line is synthetic receiver function with 400 m soil layer.

1.4 Likelihood Functions

The goal of any modeling exercise is to find the model that best reproduces a given set of data or observations as a step toward interpreting what the model tells us about the physical universe. In this project, I performed a joint inversion of seismic receiver functions with gravity and other observables in order to constrain thickness and velocity properties of the crust. Joint data inversion problems are

generally challenging because simple minimization of data misfits may not be optimal when different types of observables with different physics are combined. To overcome this challenge, I use a Bayesian approach in which I calculate probability density functions or "likelihoods" calculated for the parameter space from one minimization problem and multiply these by likelihoods derived from a different set of observables.

Taking gravity modeling as an example, I would like to know the probability density of a model of Bouguer gravity given the observed Bouguer gravity $\vec{B}_o$ as a function of crustal thickness and v_P/v_S model parameters (H_b, κ_b). In practice, this is calculated from the root-mean square model misfit:

$$R = \sqrt{\frac{\left(B_{\text{obs}} - B_{\text{mod}}\right)^2}{N}} \qquad (1.4)$$

using the *F* cumulative distribution via the likelihood ratio method (Becker & Arnold, 1977). Assuming zero-mean, uncorrelated errors, the confidence region with probability $1-\alpha$ of containing the solution is the volume of the model parameter space for which:

$$R^2 \le R_{\text{min}}^2 \left[1 + \frac{M}{N-M} F_\alpha^{-1}\left(M, N-M\right)\right] \qquad (1.5)$$

where *M* is the number of model parameters, *N* is the number of observations and R_{min} is the minimum root-mean square misfit over all models. Strictly speaking, the

confidence probabilities α as a function of parameters (H_b, κ_b) represent a probability density function only after normalization such that the integral of the functional over all of the parameter volume is equal to one. However, Bayes' theorem uses the likelihood functions in multiplicative series, and after multiplication the parameters corresponding to the maximum of the functional are independent of the constant multipliers that would normalize each of the likelihoods. Consequently, we use the probabilities without normalization. An example gravity likelihood function is shown for site TA.R48A in Figure 4.

1.5. Overview of the Dissertation

For my dissertation, I use EarthScope data to model the averaged one-layer and two-layer thickness and compositional properties of the continental crust of the United States with joint inversion of gravity and space statistic. The results are interpreted with the aid of mineral physics modeling and other geophysical observations.

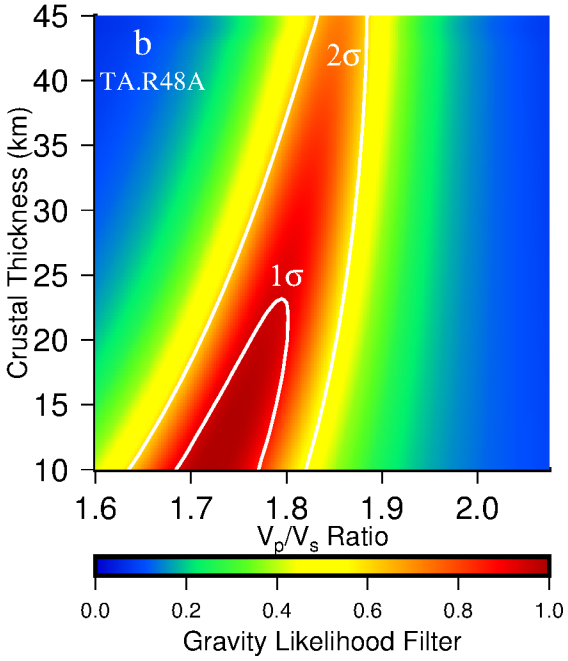

Figure 4: Example of a likelihood filter calculated from root-mean square misfits to gravity using the likelihood ratio method.

Chapter 2 (a paper already accepted for publication in a special issue of the journal *Tectonics*) describes thickness and bulk v_P/v_S of a single-layer crustal model over the entire United States. In this first step of my research, I generate synthetic receiver functions for a wide range of crustal thickness and v_P/v_S parameterizations, and I calculate the cross-correlation coefficients of observed receiver functions compared with synthetic models. The parameter-space cross-correlations, stacked over multiple earthquake events, are jointly inverted in a Bayesian approach with probability density functions derived from gravity modeling and spatial statistics. Individual site estimates are updated iteratively over hundreds of iterations. The gravity anomalies modeled from the resulting estimates of crustal variation are also

evaluated. Thermodynamical modeling was also performed to aid in interpretation of the likely mineral assemblages associated with observed v_P/v_S variations.

Chapter 3 describes modeling of the crust as a two-layer medium, in a continuation of effort begun for the one-layer model. Using the total thickness and v_P/v_S estimated from joint inversion of a one-layer model as a starting point, I build synthetic receiver functions for each seismic station for a range of possible upper-layer thickness and v_P/v_S (with thickness and v_P/v_S of the lower layer then determined by the total). Similar to the one-layer inversion, parameter-space cross-correlation stacks are jointly inverted with probability density functions derived from gravity modeling and spatial statistics in an iterative fashion. Vertical cross-sections of the cross-correlation stack energy are also examined, and I calculate 2D cross-correlation of the model results with other types of geophysical data to illuminate the possible mineralogical implications of the results.

Chapter 4 describes a simulation of reaction thermodynamics and heat transfer due to hydration in the crust. The goal of this chapter is to examine possible mechanisms for a previously-observed discrepancy between high heat surface heat flow and anomalously cold Moho in the western U.S. Cordilleran footprint of Laramide deformation (Berry et al., 2015). I model the thermal diffusion of a crustal hydration reaction enthalpy anomaly predicted by mineral thermodynamics, and examine the evolution predicted for surface heat flow and Moho temperature as a function of time after hydration.

Chapter 5 summarizes the results and conclusions of the previous chapters, including the implications for evolution and particularly hydration history of the U.S. continental crust. I hypothesize that volatile flux, and especially hydration history, has played an important role in dynamism, tectonism and elevation of the western U.S. Cordillera, and that thermal perturbations may indicate partial melt is still present in the lower crust under the Cordillera. In this context, I propose that v_P/v_S can be used as a valuable new tool for examining hydration processes related to subduction globally.

1.5 References

Ammon, C. J., Randall, G. E., & Zandt, G. (1990). On the nonuniqueness of receiver function inversions. *Journal of Geophysical Research*, *95*(B10), 15,303-15,318. https://doi.org/10.1029/JB095iB10p15303

Armstrong, R. L. (1972). Low-angle (denudation) faults, hinterland of the Sevier orogenic belt, eastern Nevada and western Utah. *Geological Society of America Bulletin, 83*(6), 1729-1754. https://doi.org/10.1130/0016-7606(1972)83[1729:LDFHOT]2.0.CO;2

Andrews, J., & Deuss, A. (2008). Detailed nature of the 660 km region of the mantle from global receiver function data. *Journal of Geophysical Research*, *113*(B6). https://doi.org/10.1029/2007JB005111

Artemieva, I. M., & Mooney, W. D. (2002). On the relations between cratonic lithosphere thickness, plate motions, and basal drag. *Tectonophysics*, *358*(1), 211-231. https://doi.org/10.1016/S0040-1951(02)00425-0

Bally, A. W. (1989). Phanerozoic basins of North America. *The Geology of North America*, 397-446. https://doi.org/10.1130/DNAG-GNA-A.397

Becker, T. W., C. Faccenna, E. D. Humphreys, A. R. Lowry, & M. S. Miller (2014). Static and dynamic support of western United States topography, *Earth and Planetary Science Letters*, 402, 234-246. https://doi.org/10.1016/j.epsl.2013.10.012

Beck, J. V., & Arnold, K. J. (1977). *Parameter estimation in engineering and science*. (Willey, 1977).

Berry, M. A., A. R. Lowry, D. L. Schutt, R. V. S. Kanda, & J. S. Buehler (2015), Cold and wet at the roots of U.S. Cordilleran high elevation, Abstr. #T11C-2910, *AGU Fall Meeting*, San Francisco CA.

Bird, P. (1984). Laramide crustal thickening event in the Rocky Mountain foreland and Great Plains. *Tectonics, 3*(7), 741-758. https://doi.org/10.1029/TC003i007p00741

Bird, P. (1998). Kinematic history of the Laramide orogeny in latitudes 35°–49°N, western United States. *Tectonics, 17*(5), 780-801. https://doi.org/10.1029/98TC02698

Burdick, L. J., & Langston, C. A. (1977). Modeling crustal structure through the use of converted phases in teleseismic body-wave forms. *Bulletin of the Seismological Society of America*, *67*(3), 677-691.

Forsyth, D., & Uyeda, S. (1975). On the relative importance of the driving forces of plate motion. *Geophysical Journal International*, *43*(1), 163-200. https://doi.org/10.1111/j.1365-246X.1975.tb00631.x

Mavko, G. (accessed 2017). Unpublished course notes, available at https://pangea.stanford.edu/courses/gp262/Notes/8.SeismicVelocity.pdf

Green, J. C. (1983). Geologic and geochemical evidence for the nature and development of the Middle Proterozoic (Keweenawan) Midcontinent Rift of North America. *Tectonophysics*, 94(1), 413-437. https://doi.org/10.1016/0040-1951(83)90027-6

Green, A. G., Cannon, W. F., Milkereit, B., Hutchinson, D. R., Davidson, A., Behrendt, J. C., Spencer, C., Lee, M. W., Morel-á-LáHuissier, P. & Agena, W. F. (1989). A “Glimpce“ of the Deep Crust Beneath the Great Lakes. In R. F. Mereu, S. Mueller, D. M. Fountain (Eds.). *Properties and Processes of Earth's Lower Crust*, American Geophysical Union, Washington, D. C. https://doi.org/10.1029/GM051p0065

Hatcher, R. D. (2010). The Appalachian orogen: A summary. *Geological Society of America Memoirs, 206*, 1-19. https://doi.org/10.1130/2010.1206(01)

Hoffman, P. F. (1988). United plates of America, the birth of a craton: Early Proterozoic assembly and growth of Laurentia. *Annual Review of Earth and Planetary Sciences*, *16*(1), 543-603. https://doi.org/10.1146/annurev.ea.16.050188.002551

Humphreys, E., E. Hessler, K. Dueker, G. L. Farmer, E. Erslev, & T. Atwater (2003), How Laramide-age hydration of North American lithosphere by the Farallon slab controlled subsequent activity in the western United States. *International Geology Review, 45*(7), 575-595. http://dx.doi.org/10.2747/0020-6814.45.7.575

Hyndman, R. D., & Currie, C. A. (2011). Why is the North America Cordillera high? Hot backarcs, thermal isostasy, and mountain belts. *Geology*, *39*(8), 783-786. http://dx.doi.org/10.1130/G31998.1

Levander, A., & Miller, M. S. (2012). Evolutionary aspects of lithosphere discontinuity structure in the western US. *Geochemistry, Geophysics, Geosystems, 13*(7). https://doi.org/10.1029/2012GC004056

Lowry, A. R., N. M. Ribe, & R. B. Smith (2000). Dynamic elevation of the Cordillera, western United States. *Journal of Geophysical Research*, *105*, 23,371-23,390. https://doi.org/10.1029/2000JB900182

Lowry, A. R., & Pérez-Gussinyé, M. (2011). The role of crustal quartz in controlling Cordilleran deformation. *Nature, 471*(7338), 353-357. http://dx.doi.org/10.1038/nature09912

Mac Niocaill, C., Van der Pluijm, B. A., & Van der Voo, R. (1997). Ordovician paleogeography and the evolution of the Iapetus ocean. *Geology, 25*(2), 159-162. https://doi.org/10.1130/0091-7613(1997)025%3C0159:OPATEO%3E2.3.CO;2

Pelletier, J. D., Broxton, P. D., Hazenberg, P., Zeng, X., Troch, P. A., Niu, G. Y., ... & Gochis, D. (2016). A gridded global data set of soil, intact regolith, and sedimentary deposit thicknesses for regional and global land surface modeling. *Journal of Advances in Modeling Earth Systems*. *8*(1), 41-65. https://doi.org/10.1002/2015MS000526

Phinney, R. A. (1964). The structure of the Earth's crust from spectral behaviour of long-period body waves. *Journal of Geophysical Research, 69(14), 2997-3017* . https://doi.org/10.1029/JZ069i014p02997

Porter, R., H. Gilbert, G. Zandt, S. Beck, L. Warren, J. Calkins, P. Alvarado, & M. Anderson (2012). Shear wave velocities in the Pampean flat-slab region from Rayleigh wave tomography: Implications for slab and upper mantle hydration. *Journal of Geophysical Research. 117*(B11). https://doi.org/10.1029/2012JB009350

Ravat, D. N. (1984). Magnetic Investigations in the St. Louis Arm of the New Madrid Rift Complex, Purdue University (Doctoral dissertation, 102 pp).

Roy, M., Jordan, T. H., & Pederson, J. (2009). Colorado Plateau magmatism and uplift by warming of heterogeneous lithosphere. *Nature, 459*(7249), 978-982. http://doi.org/10.1038/nature08052

Schulte-Pelkum, V., & Mahan, K. H. (2014). A method for mapping crustal deformation and anisotropy with receiver functions and first results from USArray. *Earth and Planetary Science Letters, 402*, 221-233. https://doi.org/10.1016/j.epsl.2014.01.050

Tikoff, B., & Maxson, J. (2001). Lithospheric buckling of the Laramide foreland during Late Cretaceous and Paleogene, western United States. *Rocky Mountain Geology, 36*(1), 13-35. https://doi.org/10.2113/gsrocky.36.1.13

Van Schmus, W. R., Bickford, M. E., & Turek, A. (1996). Proterozoic geology of the east-central Midcontinent basement. Special Papers-Geological Society of America, 7-32. https://doi.org/10.1130/0-8137-2308-6.7

Van Schmus, W. R., & Hinze, W. J. (1985). The midcontinent rift system. Annual *Reviews of Earth and Planetary Sciences, 13*(1), 345-383. https://doi.org/10.1146/annurev.ea.13.050185.002021

Vinnik, L. P. (1977). Detection of waves converted from P to SV in the mantle*. Physics of the Earth and Planetary Interiors, 15*(1), 39-45. https://doi.org/10.1016/0031-9201(77)90008-5

Yuan, H., & Romanowicz, B. (2010). Lithospheric layering in the North American craton. Nature, 466(7310), 1063-1068. https://doi.org/10.1038/nature09332

Zhu, L., & H. Kanamori (2000), Moho depth variation in southern California from teleseismic receiver functions, *Journal of Geophysical Research*, *105*(B2), 2969-2980. https://doi.org/10.1029/1999JB900322

CHAPTER 2

USARRAY IMAGING OF CONTINENTAL CRUST IN THE CONTERMINOUS UNITED STATES

Abstract

The thickness and bulk composition of continental crust provide important constraints on the evolution and dynamics of continents. Crustal mineralogy and thickness both may influence gravity anomalies, topographic elevation and lithospheric strength, but prior to the inception of EarthScope's USArray, seismic measurements of crustal thickness and properties useful for inferring lithology are sparse. Here we improve upon a previously-published methodology for joint inversion of Bouguer gravity anomalies and seismic receiver functions by using parameter-space stacking of cross-correlations of modeled synthetic and observed receiver functions instead of standard H-κ amplitude stacking. The new method is applied to estimation of thickness and bulk seismic velocity ratio, v_P/v_S, of continental crust in the conterminous United States using USArray and other broadband network data. Crustal thickness variations are reasonably consistent with those found in other studies and show interesting relationships to the history of North American continental formation. Seismic velocity ratios derived in this study are more robust than in other analyses, and hint at large-scale variations in composition of continental crust. To interpret the results, we model the pressure/temperature-

dependent thermodynamics of mineral formation for various crustal chemistries, with and without volatile constituents. Our results suggest that hydration lowers bulk crustal v_P/v_S and density, and releases heat in the shallow crust but absorbs heat in the lowermost crust (where plagioclase breaks down to pyroxene and garnet, resulting in higher seismic velocity). Hence, v_P/v_S variations may provide a useful proxy for hydration state in the crust.

2.1. Introduction

The formation and evolution of Earth's continental crust has broad implications for tectonism, dynamics and mass transfer processes. Open questions regarding the tectonic, melt and volatile flux processes that form the crust remain among the outstanding challenges for research in the solid Earth sciences (DePaolo et al., 2008; Williams et al., 2010). Continental lithosphere is more resistant to subduction than oceanic lithosphere because of the greater buoyancy (due to greater thickness and lower density) of continental crust, resulting in a much longer and richer record of Earth history in continental lithosphere than is found in the oceans.

Seismic investigations are an important tool for assessing continental crustal composition and related evolution and dynamics (Miller & Christensen, 1994; Sobolev & Bakeyko, 1994; Christensen & Mooney, 1995; Kern et al., 1996; Musacchio et al., 1997; Hacker et al., 2015), along with sampling of exposed rocks (Rudnick & Fountain, 1995; Hacker et al., 2015) and xenoliths carried from the

middle and lower crust (Weber, 2002; Mengel, 1991). The bulk composition of the crust is andesitic, with averaged weight-% SiO_2 generally decreasing with depth (Rudnick & Fountain, 1995), reflecting the repeated melt fractionation and transport processes that form typical continental crust (e.g., Solano et al., 2012). Seismic velocity and density of crustal mineral assemblages are sensitive to the bulk chemistry but also reflect the metamorphic grade at time of formation (i.e., pressure and temperature thermodynamical state) and volatile state (e.g., Guerri et al., 2015; Jones et al., 2015).

The EarthScope Major Research Facilities and Equipment project, funded in 2002 with instrumentation first installed beginning in 2004, was designed to identify links between surface geology and deep-Earth processes. EarthScope's USArray seismic network, including 400 three-component broadband seismographs deployed in the Transportable Array (TA) rolling network covering the entire continental United States, serves as a principal data source for this project. The TA has now completed data collection in the lower 48 United States and is currently deployed in Alaska. Our imaging of the crust uses seismic receiver functions from USArray (including the TA) as well as FlexArray and other contributed seismic networks that have been analyzed for the EarthScope Automated Receiver Survey (EARS) (Crotwell & Owens, 2005; IRIS DMC, 2010).

Several studies have used EarthScope data to image thickness and velocity properties of continental crust within the USArray footprint, with most using receiver functions (e.g., Levander & Miller, 2012; Schulte-Pelkum & Mahan, 2014), ambient

noise surface wave tomography (e.g., Porter et al., 2016; Lin et al., 2012), regional first arrivals (Buehler & Shearer, 2014; 2017) or some combination of these (e.g., Schmandt et al., 2015; Shen & Ritzwoller, 2016). Our approach differs slightly from these in that we perform joint inversion of receiver functions and gravity, coupled with a thermal structure derived from Pn tomography (Schutt et al., 2017), to more robustly constrain density variations and seismic velocity ratios v_P/v_S in the crust. Lowry & Pérez-Gussinyé (2011), using a similar approach, previously interpreted variations imaged in bulk crustal v_P/v_S to primarily reflect variations in abundance of quartz based on petrophysical measurements compiled by Christensen (1996) (Figure 5). Further noting a strong correlation of low v_P/v_S to high surface heat flow and high Cordilleran elevations, they hypothesized a dynamical feedback that began with localization of crustal deformation where crust had low ductile strength owing to the presence of quartz, and that lithospheric viscosity was lowered further by advective warming and hydration resulting from the strain.

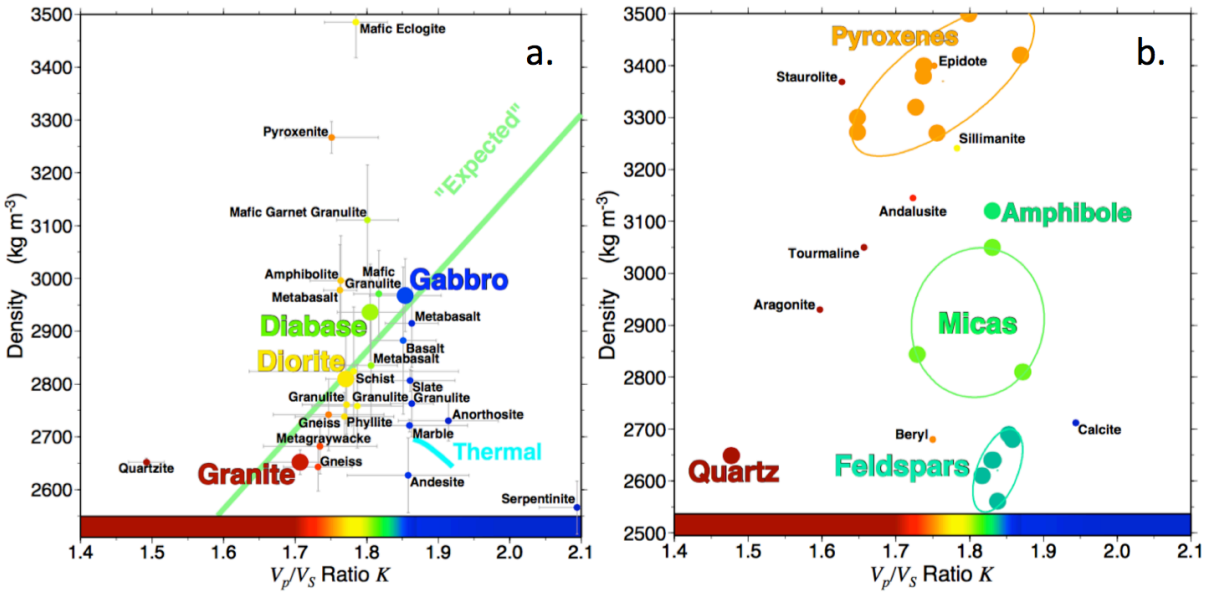

Figure 5: The relationship of v_P/v_S and density to mineral composition (after Lowry & Pérez-Gussinyé, 2011). (a) is rock density versus v_P/v_S for various rock types using data from Christensen (1996); the temperature dependence of v_P/v_S in anorthite for a 900°C range (cyan curve, after Kono et al. (2008)) is comparatively small. (b) shows geophysical properties for minerals and demonstrates that v_P/v_S variation in rocks is dominated by quartz content.

Water plays an important role in crustal formation by lowering the melting temperature of mantle rocks, and so seems to be a key ingredient in the seeding of thicker crust in ocean island arcs as well as the formation of more silica-rich continental crust. Water is also an important determinant for ductile rheological strength (Kohlstedt, 2006) and hence the mobility/stability of continental lithosphere. However, the distributions and history of hydration state in continental crust and

lithosphere are generally enigmatic because of ambiguities in separating effects of chemistry, temperature, hydration and melt in remote sensing by seismic and electrical imaging, coupled with the extremely sparse in-situ sampling by xenoliths (e.g., Jones et al., 2015). In this paper, we extend an improved inversion based on the approach of Lowry & Pérez-Gussinyé (2011) to imaging of the entire conterminous United States, and we expand upon earlier interpretations of the significance of bulk crustal v_P/v_S for crustal chemistry and crustal properties by modeling the pressure-, temperature-, chemistry- and hydration state-dependence of seismic velocities and density in the crust.

2.2. Methods

This paper extends an earlier analysis by Lowry & Pérez-Gussinyé (2011) that covered only the western U.S. data available at that time. The joint inversion of seismic receiver functions, gravity and spatial statistics used here to image the USArray footprint (including the conterminous United States and southernmost Canada) is similar to the methodology described by Lowry & Pérez-Gussinyé (2011). The primary differences are the addition of newer USArray and other seismic data (Figure 6), and three modifications to the joint inversion methodology designed to improve performance. First, instead of using EARS parameter-space stacks of receiver function amplitudes (Zhu & Kanamori, 2000; Crotwell & Owens, 2005), we built a library of synthetic receiver functions and stacked cross-correlation

coefficients relating synthetic to observed receiver functions from the EARS database (IRIS DMC, 2010) in the crustal thickness and v_P/v_S parameter space. Second, we implemented a stochastic inversion for density parameters associated with crustal thickness, v_P/v_S and thermal contributions to gravity. Finally, we estimated and removed gravity anomalies due to geothermal variations in the lithosphere using a combination of surface heat flow and Moho temperature estimates derived from Pn tomography (Schutt et al., 2016; 2017) instead of surface heat flow alone.

2.3. Data

Data for this analysis are from the EarthScope Automated Receiver Survey (EARS) (Crotwell & Owens, 2005; IRIS DMC, 2010; Trabant et al., 2012), with station locations shown in Figure 6. I used EARS receiver functions only for those seismic events with a radial match for the iterative deconvolution (Ligorría & Ammon, 1999) exceeding 80%.

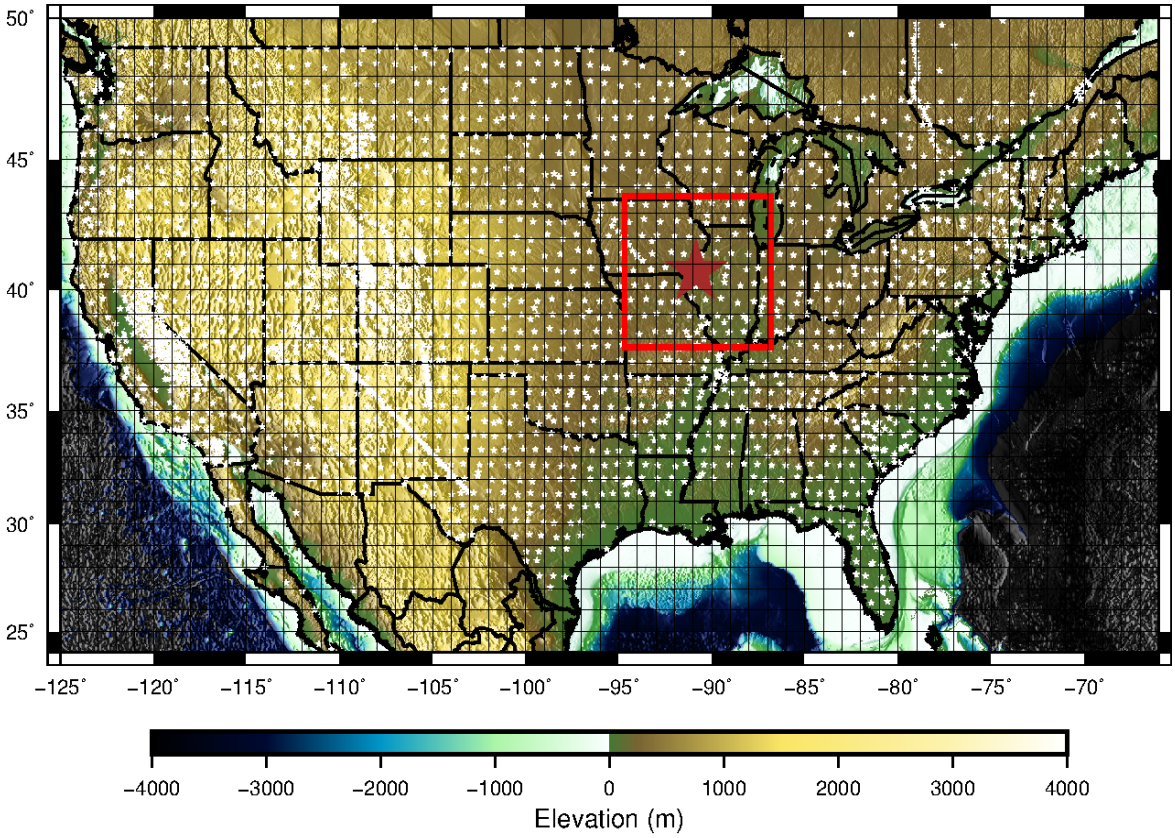

Figure 6: Seismic station map. USArray and other seismic stations used in this analysis (triangles) on a map of topographic elevation with shaded relief. All seismic stations in the EARS receiver function database (Crotwell & Owens, 2005; IRIS DMC, 2010; Trabant et al., 2012) were included in the analysis, including regional networks and PASSCAL and FLEXArray deployments. The nearly 3000 total seismic stations average 46 events for each station. Red star is the location of seismic station TA.N41A used as an example in subsequent figures. Stochastic inversion for density parameters uses gravity and seismic fields from the entire United States; subgrids used to estimate gravity likelihoods are exemplified by the red box centered around the star at TA.N41A.

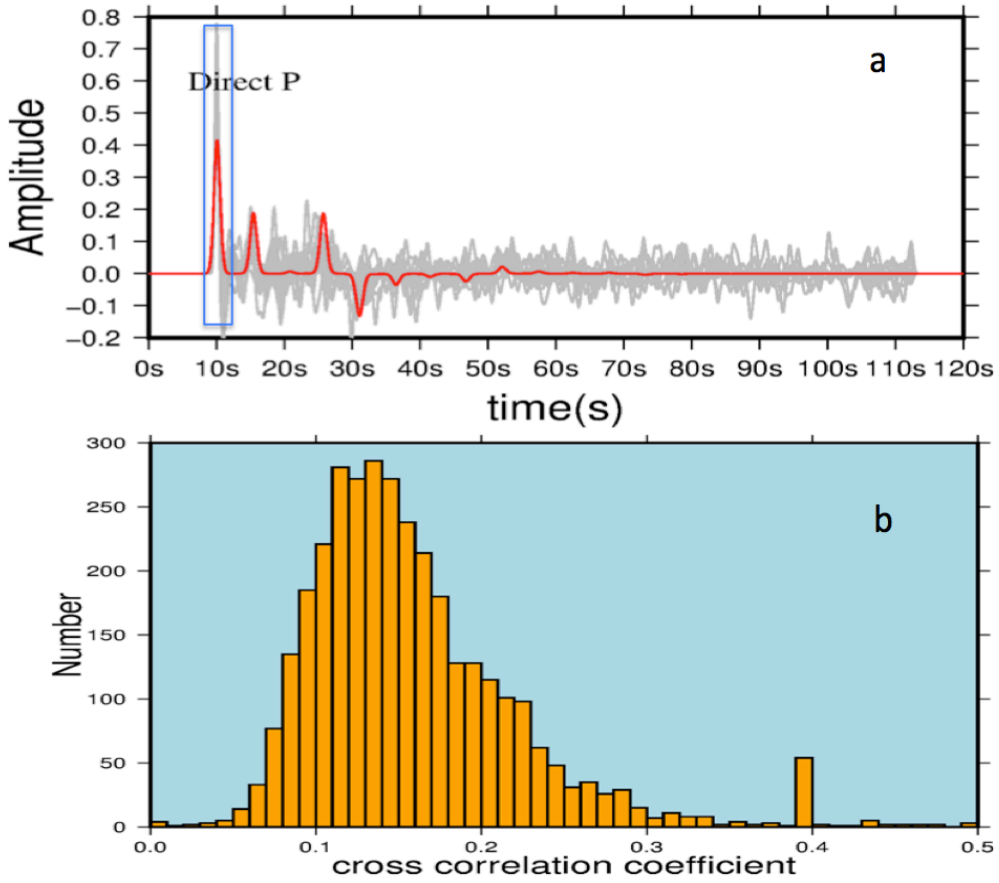

Figure 7: Example observed and synthetic (one-layer model) receiver functions. (a): observed EARS radial receiver functions (grey) for 54 events at site TA.N41A, and the synthetic receiver function that correlated most strongly with the observed receiver functions (red). The direct P arrival inside the blue rectangle is removed before cross-correlation. (b): a histogram of the maximum cross-correlation coefficients found at each of the >3000 sites in the study region; the median maximum cross-correlation is 0.14.

2.4 Receiver Function Synthetics and Cross-Correlation Stacking

EARS (Crotwell & Owens, 2005) *H*-κ amplitude stacks were used in the analysis of Lowry & Pérez-Gussinyé (2011), but here we introduce a new approach to parameter-space receiver function analysis. Typical *H*-κ stacking approaches to estimating bulk crustal properties (e.g., Zhu & Kanamori, 2000) stack the amplitudes at arrival times predicted for the Ps Moho conversion, the PpPs reverberation, and the PpSs+PsPs reverberation given a range of assumed crustal thickness and v_P/v_S. Each of these phase arrivals is weighted equally for each event in the amplitude stack, but in practice the relative scaling of the receiver function arrival amplitudes depends on the Moho impedance contrast, the ray parameter of the event, and interference from phases deriving from other impedance contrasts. Hence, we instead compare (via cross-correlation) the full waveform of each receiver function to synthetic receiver functions generated using a synthetic receiver function code (Ammon, 1991).

A library of synthetic receiver function models was calculated, parameterized by crustal thicknesses ranging from 20 to 60 with sample mesh 0.25 km, and v_P/v_S from 1.6 to 2.1 at a 0.025 mesh, for a total of 3200 models. Each synthetic model assumes a uniform isotropic crustal layer with P velocity 6.3 km/s and upper mantle velocity of 8.0 km/s. Bulk crustal v_P is not uniform across the U.S., instead ranging from 6.1 to 6.5 km/s based on crustal-scale seismic reflection and refraction data (Smith et al., 1989; Pakiser, 1989; Braile et al., 1989). Building a larger library would

be computationally expensive, and Zhu & Kanamori (2000) note that a 0.1 km/s error in crustal v_P translates to a timing error equivalent to only a 0.5 km error in crustal thickness. Uppermost mantle velocity varies from 7.7 to 8.4 km/s (Buehler & Shearer, 2017), but mantle velocity impacts only amplitude of reverberation phases and does not affect arrival time. The cross-correlation method described here is relatively insensitive to amplitude, so our synthetics assume a constant 8.0 km/s upper mantle.

The synthetic receiver function modeling approach of Ammon (1991) specifies a white-noise level, *C*, to prevent numerical singularity of the deconvolution. We tested values for *C* ranging from 0.1 to 0.00001 and settled on 0.00001 as the most robust. The algorithm also specifies a Gaussian filter width, *a.* We adopt *a* = 2.5 s as used by EARS to generate the synthetic receiver functions. All observed receiver functions were resampled to 10 Hz, the sample rate of the synthetic receiver function.

Before cross-correlating, the observed and synthetic receiver functions were aligned to impose coincident timing of the direct P arrival, after which the direct P arrival in each was masked so that only the later phase arrivals were included in the cross-correlation calculation (Figure 7). This is done because the only useful information content in the P arrival, for our purposes, is the reference time of the receiver function, and including the P phase degrades the resolving power of the receiver function correlations. We average the cross-correlations for all earthquake events as a function of the crustal thickness (*H*) and seismic velocity ratio v_P/v_S assumed in the synthetic model, analogous to the *H*-κ parameter-space

representation used in amplitude stacking (Zhu & Kanamori, 2000). Like with H-κ stacking, the raw cross-correlation stacks exhibit several local maxima (Figure 8). The largest cross-correlation coefficients tend to be low, with median maxima around 0.14 (Figure 7a). For example, the maximum cross-correlation coefficient at station TA.N41A is only 0.19 at H = 35 km and v_P/v_S = 1.93 (Figure 6). A secondary local maximum occurs at H = 45 km, v_P/v_S = 1.7, and a tertiary maximum occurs at a crustal thickness of 20 km and v_P/v_S of 1.72.

Averaged cross-correlations are low with multiple maxima in part because the real-Earth crust is not a single uniform layer as our modeling assumes. Converted phases are generated at all impedance contrasts in the crust and mantle, and both crustal thickness and v_P/v_S can vary on scales sampled by the conversions and reverberations from different azimuths of earthquake events at a single site. Cross-correlations are significantly reduced by differences in the receiver functions for different events with different back-azimuths. For example, we took the receiver function from the largest event recorded at station TA.N41A (a M8.4 event, with the second-highest radial match of 98.2%) and compared to all other events using our cross-correlation approach. The resulting average cross-correlation was 0.32. This relatively low correlation of events is likely some combination of “noise” in the receiver function estimate (loosely characterized in the EARS receiver functions by radial match of the deconvolution, in which events with match <80% are rejected (Crotwell & Owens, 2005)) and back-azimuth-dependent variations in timing and amplitude related to layer heterogeneity and anisotropy effects (e.g., Schulte-Pelkum

& Mahan, 2014). The additional difference between a cross-correlation of 0.32, representing the maximum theoretically possible for a 1D, isotropic Earth model at station TA.N41A, and the 0.19 maximum of our comparison to synthetic models likely relates to some combination of multiple layering of the real-Earth lithosphere, and differences in layer impedance from that assumed by the synthetic. Regardless, the cross-correlation approach introduced here produces secondary maxima that are generally much smaller relative to the global maximum than standard H-κ stacking like that used in the joint inversion of Lowry & Pérez-Gussinyé (2011) (Figure 8b).

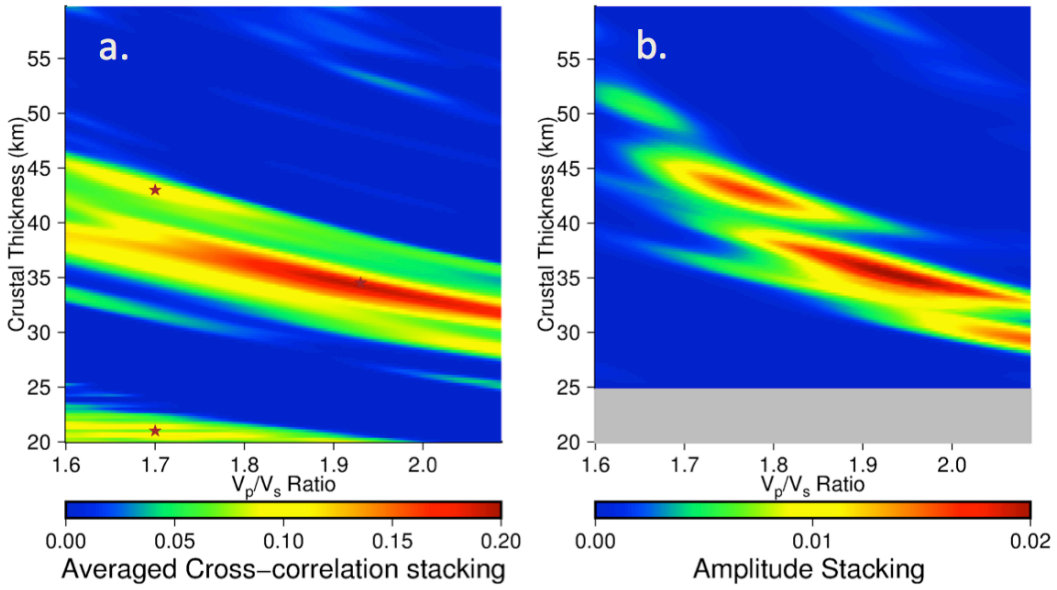

Figure 8: Example parameter-space receiver function analyses at seismic station TA.N41A. (a) Cross-correlations of observed and modeled receiver functions, averaged for 54 earthquake events, as a function of crustal thickness H and v_P/v_S assumed in the synthetic model. Local maxima are marked by stars. The global maximum averaged cross-correlation is 0.19 at H = 35 km, v_P/v_S = 1.93. The local maximum at H = 20 km likely reflects P-to-S conversions at the mid-crustal interface. (b) EARS (Crotwell & Owens, 2005) amplitude stack. Similar to the H-κ amplitude stacking approach (Zhu & Kanamori, 2000), cross-correlation maxima in (a) are elongate along the v_P/v_S axis so are more sensitive to crustal thickness than v_P/v_S, but secondary maxima of the cross-correlation averages are diminished relative to those of amplitude stacks and hence less likely to be mistaken for the true model.

2.5 Gravity Modeling

The receiver functions observed at a single seismic station are not the only pieces of information that constrain this problem, as both gravity and the spatial statistics of estimates at neighboring sites afford additional predictive power. Individual contributions to the total Bouguer gravity anomaly field from crustal thickness H, bulk v_P/v_S κ and thermal variations T are scaled by density parameters $\Delta\rho_{\text{Moho}}$ for the density contrast at the Moho, $\partial\rho/\partial\kappa$ for the change in density for given change in v_P/v_S, and a coefficient of thermal expansion α_v, respectively, and Gravity due to crustal thickness variations is modeled as (Lowry & Pérez-Gussinyé, 2011):

$$\widetilde{B}_H = 2\pi G \Delta\rho_{Moho} \widetilde{H} \exp(-k\overline{H}) \qquad (2.1)$$

in which the overbar indicates the mean of a field, the tilde ~ denotes 2D Fourier-transformed amplitudes of a field with the mean removed (e.g., $\widetilde{H} = F\{H(x,y) - \overline{H}\}$ where $F\{\bullet\}$ denotes the 2D Fourier transform operator); G is the universal gravitational constant; and k is the modulus of 2D wavenumber associated with each amplitude. Variations in bulk v_P/v_S are assumed to be uniformly distributed with depth and the associated gravity anomalies are calculated as:

$$\widetilde{B}_\kappa = 2\pi G \frac{\partial\rho}{\partial\kappa}\left[\frac{1-\exp(-k\overline{H})}{k}\widetilde{K} - \widetilde{M}\exp(-k\overline{H})\right] \qquad (2.2)$$

Here, $\widetilde{M} = F\{(H-\overline{H})(\kappa-\overline{\kappa})\}$ is a correction factor for mass associated with varying crustal thickness and v_P/v_S at the Moho. Finally, gravity anomalies associated with

thermal variations are calculated from the three-dimensional temperature field model described in section 2.7 via:

$$\widetilde{B}_T = \int_0^{200} 2\pi G \alpha_v \bar{\rho}(z) \widetilde{T}(z) \exp(-kz) dz \qquad (2.3)$$

We derive $\bar{\rho}(z)$ from mean temperatures in the geothermal model combined with expected density for a mean continental crustal composition (Christensen & Mooney, 1995). Gravity associated with the thermal boundary layer model is integrated only to a depth of 200 km, beyond which the assumptions of steady-state conduction and constant mantle potential temperature in the thermal modeling (described in a subsequent section) may no longer be representative of actual temperature variation.

2.6 Stochastic Inversion for Density Parameters

In practice, the density parameters $\Delta\rho_{\text{Moho}}$, $\partial\rho/\partial\kappa$ and α_v are not known a priori. The green line in Figure 5a, derived from a weighted regression of the measurements in Christensen (1996), implies $\partial\rho/\partial\kappa$ = 1600 kg/m^3, but scatter in the relationship is obviously large. The globally averaged Moho density contrast $\Delta\rho_{\text{Moho}}$ estimated for the Preliminary Preferred Earth Model (PREM) (Dziewonski & Anderson, 1981) is 480 kg/m^3, and Tenzer et al. (2012) estimated a similar 485 kg/m^3 from independent seismic and gravity observations. However, Martinec (1994) estimated a 280 kg/m^3 Moho contrast under the continents, and regional variations

in Pn velocity (e.g., Buehler & Shearer, 2017), coupled with a large possible range of lower crustal densities for mafic to felsic compositions, implies density contrasts ranging from 160 kg/m^3 to 440 kg/m^3 (Niu & James, 2002; Julià, 2007).

Instead of assuming density parameters *a priori*, we estimate them from the relationship of the model predictions to observed Bouguer gravity over the entire Transportable array footprint using a stochastic inversion approach. Lowry & Pérez-Gussinyé (2011) inverted for density parameters from the model fields using an ordinary least-squares approach, but this produces density parameters that are much lower than those expected based on laboratory and geophysical constraints because the model fields are cross-correlated, yielding an ill-conditioned matrix. Stochastic inversion stabilizes ill-conditioned problems analogously to damped least-squares, but using probabilistic information rather than ad-hoc damping. Stochastic inversion (analogous to Bayesian inversion) assumes a known expected value, $\langle \vec{m} \rangle$, for the model parameter vector, $\vec{m}$, and a known parameter covariance matrix, $\overline{\overline{C}}_m$, for the model parameters. We then solve for differences of the true model parameters from the expected values, $\Delta\vec{m} = \vec{m} - \langle \vec{m} \rangle$, as $\Delta\vec{m} = \left(\overline{\overline{G}}^T \overline{\overline{G}} + \overline{\overline{C}}_m^{-1} \right)^{-1} \overline{\overline{G}}^T \Delta\vec{d}$, in which $\overline{\overline{G}} = \left[\begin{array}{ccc} \vec{\tilde{B}}_H^1 & \vec{\tilde{B}}_\kappa^1 & \vec{\tilde{B}}_T^1 \end{array} \right]$ using amplitudes in equations (2.1) -(2.3) with density parameters set to one; and $\Delta\vec{d} = \vec{\tilde{B}}_{obs} - \overline{\overline{G}} \langle \vec{m} \rangle$ for observed Bouguer gravity amplitudes $\vec{\tilde{B}}_{obs}$.

Our analysis uses observed Bouguer gravity anomalies from WGM2012 (Balmino et al., 2011; Bonvalot et al., 2012). We assign expected values and standard deviations for the density parameters as $\langle \Delta\rho_{\mathrm{Moho}} \rangle$ = 300 ± 100 kg/m^3 (Ito & Simons, 2011); $\langle \partial\rho/\partial\kappa \rangle$ = 1600 ± 300 kg/m^3 based on the regression of Christensen et al. (1996) measurements in Lowry & Pérez-Gussinyé (2011); and $<\alpha_v>$ = 3.5×10^{-5} ± 3×10^{-6} after Afonso et al. (2005). Some of these density parameters can be expected to covary as well: notably, the Moho density contrast $\Delta\rho_{\mathrm{Moho}}$ is partly a function of the density of the overlying crust, which we parameterize as the density derivative with respect to v_P/v_S, $\partial\rho/\partial\kappa$. However, a portion of that covariance is independently modeled by the $\tilde{M}$ correction factor in equation (2), so $\Delta\rho_{\mathrm{Moho}}$ can be conceptualized as a reference value that should approximate the mean density contrast of the region being modeled. We assume zero off-diagonal parameter covariances, as we lack laboratory or geophysical measurements suitable to constrain independently the covariance of (for example) the continental-scale reference value of $\Delta\rho_{\mathrm{Moho}}$ with $\partial\rho/\partial\kappa$. The density parameters are estimated for large-scale grids covering all of the study area (Figure 2) and are recalculated with each new update to the seismic models of crustal thickness and v_P/v_S used in the calculation of gravity models $\vec{\tilde{B}}_H^1$ and $\vec{\tilde{B}}_\kappa^1$, respectively. In later sections we also will examine density parameters independently calculated for the eastern and western halves of the conterminous U.S.

2.7 Spatial Statistics and Optimal Interpolation

To generate gridded values of crustal thickness H and seismic velocity ratio κ needed for the gravity modeling, we must interpolate estimates of the seismic properties at irregularly-spaced seismic sites to a constant-spaced grid. For this we use optimal interpolation (OI), also called “kriging”, an interpolation method that relies on the spatial statistics of measured data to estimate the most likely value and uncertainty at an unsampled location (Davis, 1986). Optimal interpolation uses the variogram statistics of a field, an expression of the expected value of the difference between measurements as a function of the distance between the measurements.

Variograms of crustal thickness H and v_P/v_S are estimated directly from the estimates at pairs of individual seismic stations by binning according to the distance between the stations (Figure 9). Ideally, the variogram at zero distance reflects the variance of individual measurements while the variogram at large distances represents the global variance of the field. A spherical parametric model of the variogram estimates is used to invert for optimal weights applied to the estimates at sites surrounding an interpolation location, and the weights plus a Lagrange variable provide an estimate of the variance of the interpolation estimate. In addition to affording gridded interpolations of the seismic fields, optimal interpolation expected values and variance will be used to generate OI-likelihood functions at a seismic station location based on the estimates at nearby sites.

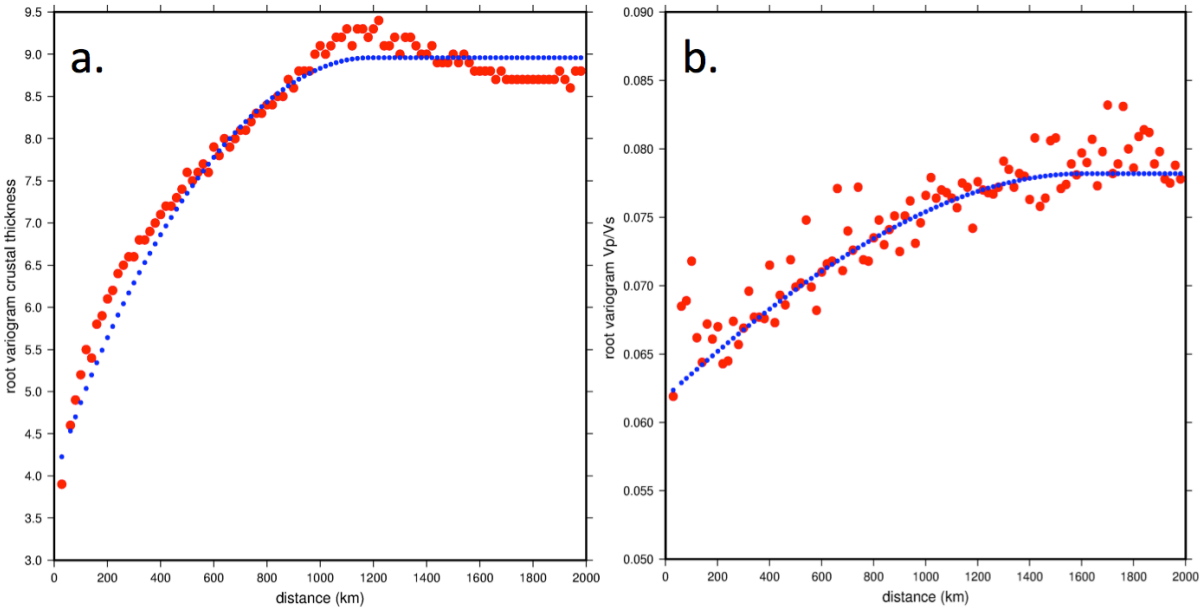

Figure 9: Root-variogram of crustal thickness (a) and v_P/v_S (b) corresponding to the root-mean square difference between measurements as a function of the distance between. Red circles are derived from all of the raw measurements after binning according to the distance between the measurements; blue circles are a parametric model (approximating the observed distribution) that was used for optimal interpolation.

2.8 Joint Inversion with Gravity and OI Likelihood Filters

The joint inversion for crustal thickness and bulk crustal v_P/v_S is applied iteratively over all of the seismic stations in the study area (Figure 6). First, a gravity likelihood filter is calculated using a 640×640 km window centered at the station slated for update, S_i. The crustal thickness H and v_P/v_S κ for station S_i are treated as unknown variables, while prior estimates of H and κ at surrounding stations are

temporarily held fixed. For each possible combination of $(H, \kappa)_j$ in the parameter space at station S_i, we interpolate (H, κ) at S_i and the surrounding sites to a 20 km-spaced, 640×640 km grid. The grids are used to model the gravity via equations (2.1)–(2.3) using density parameters derived from stochastic inversion of the larger grid as described in section 2.4. The L_2-norm, R, of the difference between observed and modeled gravity is calculated for each assumed $(H, \kappa)_j$, and contours of the misfit are used to calculate associated confidence intervals $(1 - \alpha)$ via the likelihood ratio method (Beck & Arnold, 1977):

$$R^2 \le R_{\min}^2 \left(1 + \frac{M}{N_g - M} F_\alpha^{-1}\left(M, N_g - M\right) \right) \qquad (2.4)$$

Here, $R_{\min}$ is the global minimum gravity L_2 norm, M is the number of model parameters (i.e, two corresponding to H and κ at the seismic site S_i), N_g is the number of gravity observations, F^{-1} is the inverse of the F distribution function and α is probability. The likelihood of the model given the data corresponds to the probability density function described by $(1 - \alpha)$, after normalization to yield an integral over the parameter space equal to one. An example gravity likelihood function for station TA.N41A (without normalization) is given in Figure 10b.

Optimal interpolation provides estimates of both the expected values $\left(\langle H \rangle, \langle \kappa \rangle\right)$ and standard deviations $\left(\sigma_H, \sigma_\kappa\right)$ of interpolated fields. To create the OI-likelihood filter, we interpolate estimates of crustal thickness and v_P/v_S at the nearest 150 seismic sites to the location of seismic station S_i. The C_{OI} confidence interval of

any arbitrary $(H, \kappa)_j$ in the 2D parameter space (where C_{OI} represents a real-valued multiple of normalized σ) can be calculated via:

$$C_{OI}^2\left((H,\kappa)_j\right)=\left(\frac{H_j-\langle H\rangle}{\sigma_H}\right)^2+\left(\frac{\kappa_j-\langle\kappa\rangle}{\sigma_\kappa}\right)^2 \qquad (2.5)$$

which has corresponding probability density function:

$$\alpha=\frac{1}{2\pi}\exp\left(-\frac{C_{OI}^2}{2}\right) \qquad (2.6)$$

An example OI likelihood function (without the normalization constant) is shown in Figure 10a.

Finally, both likelihood functions are multiplied by the stacked cross-correlations between modeled and observed receiver functions. This multiplication of probability density functions is thus essentially a Bayesian approach to inversion. We note that in practice the normalization constants are neglected, as they affect only the scaling and not the shape or maxima of the resulting product, which is why likelihoods in Figure 10 are all shown with a maximum of one. The crustal thickness and v_P/v_S at station S_i are then updated to the maximum of the likelihood-filtered cross-correlation stack (Figure 10d).

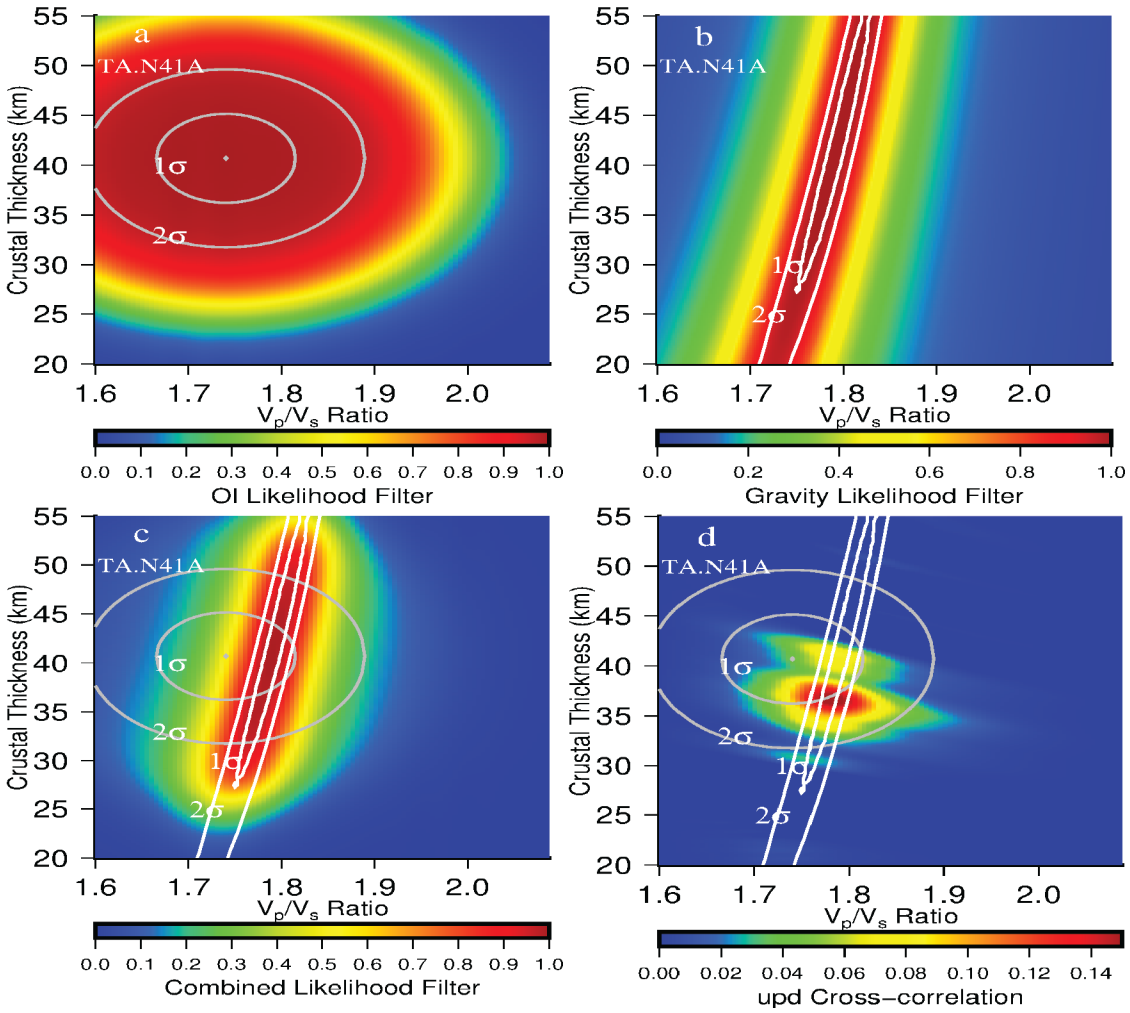

Figure 10: Example parameter-space likelihood maps for joint inversion at seismic station TA.N41A. (a) Optimal interpolation likelihood; (b) gravity likelihood; (c) the combined likelihood of OI and gravity; and (d) receiver function cross-correlation stack after likelihood filtering (compare with Figure 6, the raw cross-correlation stack at TA.N41A).

2.9. Thermal Model

As was done in Lowry & Pérez-Gussinyé (2011), we use a geothermal model patterned after Lowry et al. (2000) to reduce potential bias of mass estimates in the gravity modeling by anticorrelation of the thermal and crustal thickness fields (e.g., due to coupled crustal thinning and advective warming of the lithosphere by extensional strain). The earlier analysis used surface heat flow and surface heat production to estimate geotherms throughout the study region, where in our analysis we use both surface heat flow and an estimate of Moho temperature derived from Pn velocity tomography and mineral physics (Schutt et al., 2016; 2017) as our observables. Measurements of spatially-varying surface heat production were not used in this model after analyses showed that aerospectral gamma radiation measurements of (shallow: <1 m) surface heat production yielded no improvement in the agreement of surface heat flow and Pn geotherm models (Berry et al*.,* 2014). There are large discrepancies between the Moho temperatures predicted by conductive thermal modeling of surface heat flow and those measured from Pn that cannot be removed by varying thermal parameters describing thermal conductivity or radioactive heat production (Berry et al., 2015), so for this analysis we calculate two 1D geotherms at each map location. One geotherm, $T_q(z)$, parameterized a conductive thermal length-scale, l_{con}, for the diffusive error-function based on the surface heat flow; the other, $T_{\mathrm{Pn}}(z)$, chose l_{con} to match the Pn Moho temperature, but both used otherwise identical parameters to describe temperature-dependent thermal conductivity, depth-dependent distribution of radioactive heat production,

and mantle potential temperature. The final geotherm was a crude linear combination of the two using:

$$T(z) = \left(1 - \frac{z}{H}\right) T_q(z) + \left(\frac{z}{H}\right) T_{Pn}(z) \quad (2.7)$$

in the crust and $T(z) = T_{Pn}(z)$ in the mantle. This effectively forces the final geotherm to be more similar to the shallow observations in the shallow crust, where transients, topographically-driven hydrologic flow, and other non-steady-state and advective processes are known to perturb heat flow observations (e.g., Smith & Chapman, 1983; Ehlers, 2005), and more similar to the deep temperature measured at depth. Gravity modeling of this temperature model was found to significantly reduce gravity residuals in our models relative to geotherms derived from surface heat flow alone, lending confidence that the model is indeed an improvement. We discuss a possible mechanism for the observed discrepancy between deep and shallow heat transfer observations in section 2.4.

2.10. Results

We ran the joint inversion algorithm described in section 2 for more than ten iterations over all of the 3000 seismic sites in the study region (Figure 6). The results after multiple iterations significantly reduce the spatial variance of crustal thickness and v_P/v_S parameters relative to the estimates derived from raw cross-correlation stacks, particularly in the case of v_P/v_S. Measurement standard deviations (i.e., the zero-distance bin of variograms in Figure 9) decreased from 9.7 to 4.0 km for crustal

thickness and 0.16 to 0.07 for v_P/v_S, while global standard deviations dropped from 11.8 to 8.7 km and 0.17 to 0.08 respectively. The jointly-inverted estimates of crustal thickness are shown draped over topographic relief in Figure 11, and our v_P/v_S estimates are shown in Figure 12.

Our estimates of crustal thickness (Figure 11) are qualitatively similar to results of other studies of using different methods (e.g., Prodehl, 1970; Braile et al., 1989; Schmandt et al., 2015; Shen & Ritzwoller, 2016). A quantitative comparison to the model of Schmandt et al. (2015), which used common conversion point stacking of receiver functions in combination with Rayleigh wave modeling of velocity, yields a mean difference of 1.7 km with standard deviation of 4.0 km (which is roughly equal to our method's measurement uncertainty in Figure 9). The averaged regional crustal thickness is 38.9 km. The thinnest crust in the western U.S. is associated with oceanic-derived accretionary terranes and highly extended lithosphere in rift zones. Thicknesses less than 30 km occur along the Pacific coastline, in the southern Basin & Range province, in the northernmost part of the northern Basin & Range, and along the eastern and southern edges of the Columbia Plateau (which is part of the Siletzia terrane (Schmandt & Humphreys, 2011)). The crust under the Cascade and Sierra-Nevada mountain ranges and the Snake River plain is slightly thicker, ~35–40 km. The Great Plains, middle and southern Rocky Mountains, Colorado Plateau and Wyoming have the thickest (~45-55 km) crust in the western U.S. One minor difference between our model and other USArray models (Schmandt et al., 2015; Shen & Ritzwoller, 2016) is that our inversion finds a ~5 km

thinner crust along the southern boundary of the northern Rocky Mountains, isolating the thicker, magmatically-inflated Snake River plain crust to the south (McCurry & Rodgers, 2008) from moderately extended crust in the northern Rocky Mountains. In the eastern U.S., the thinnest crust (<30 km) is found in the Coastal Plains of the Mississippi Embayment and where attenuated by Atlantic rifting along the Atlantic coastline, although there is also surprisingly thin crust (~35 km) straddling the Great Plains/Central Lowlands boundary in the southwestern Superior province. The crust under the Great Lakes, Illinois Basin and southern Canada has mostly intermediate thickness of 37–42 km. The Appalachian Highlands by contrast have crustal thickness up to 50+ km. Of the Precambrian basement provinces, the Yavapai and Granite-Rhyolite provinces have generally thicker crust than the Mazatzal province.

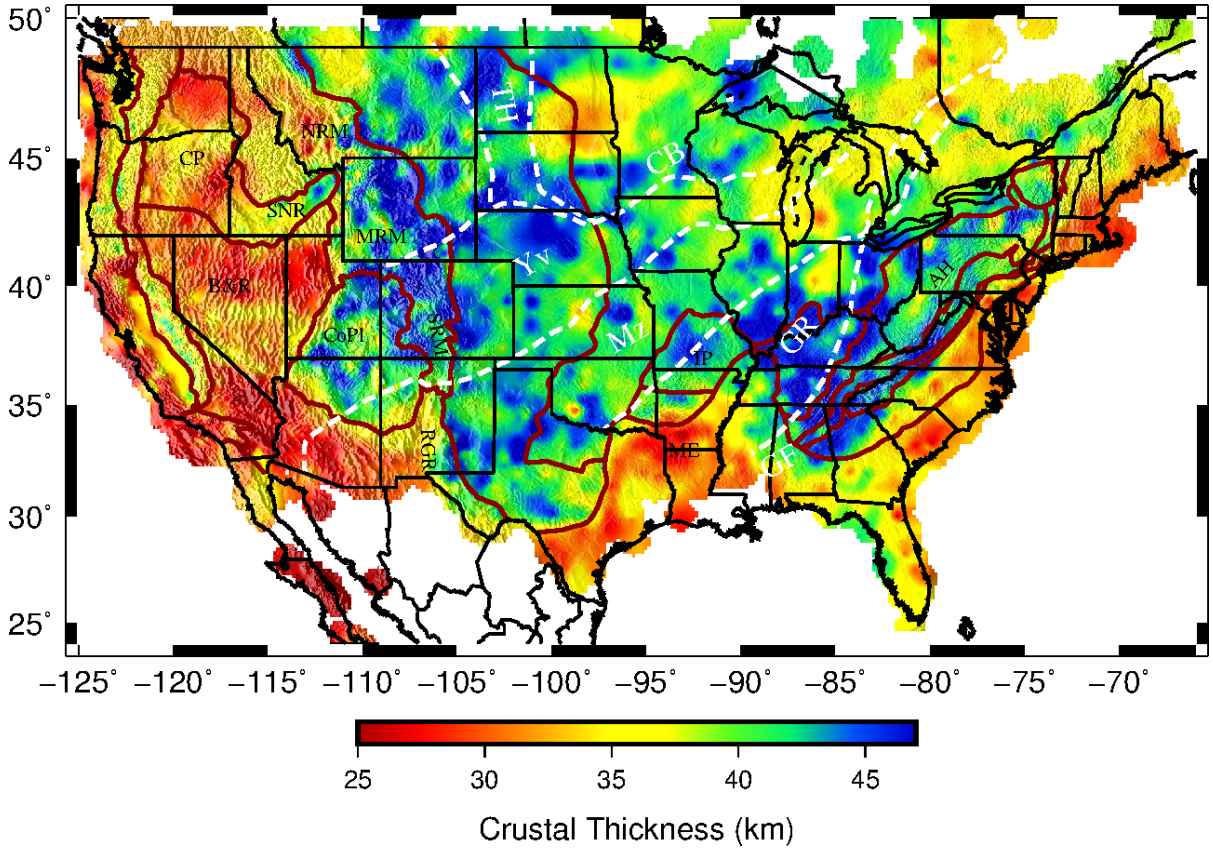

Figure 11: Map of crustal thickness, draped over shaded topographic relief. The averaged crustal thickness is 38.9 km. Physiographic province boundaries are shown in red and labeled with black text; dashed white lines with white labels are Precambrian basement features after Whitmeyer & Karlstrom (2007). AH denotes Appalachian Highlands; B&R: Basin & Range province; CB: Cheyenne belt; CoPl: Colorado Plateau; CP: Columbia Plateau; GF: Grenville Front; GR: Granite-Rhyolite province; IP: Interior Plain; ME: Mississippi embayment; MRM: middle Rocky Mountains; Mz: Mazatzal; NRM: northern Rocky Mountains; RGR: Rio Grande rift; SRP: Snake River plain; SRM: southern Rocky Mountains; TH: Trans-Hudson orogeny; Yv: Yavapai.

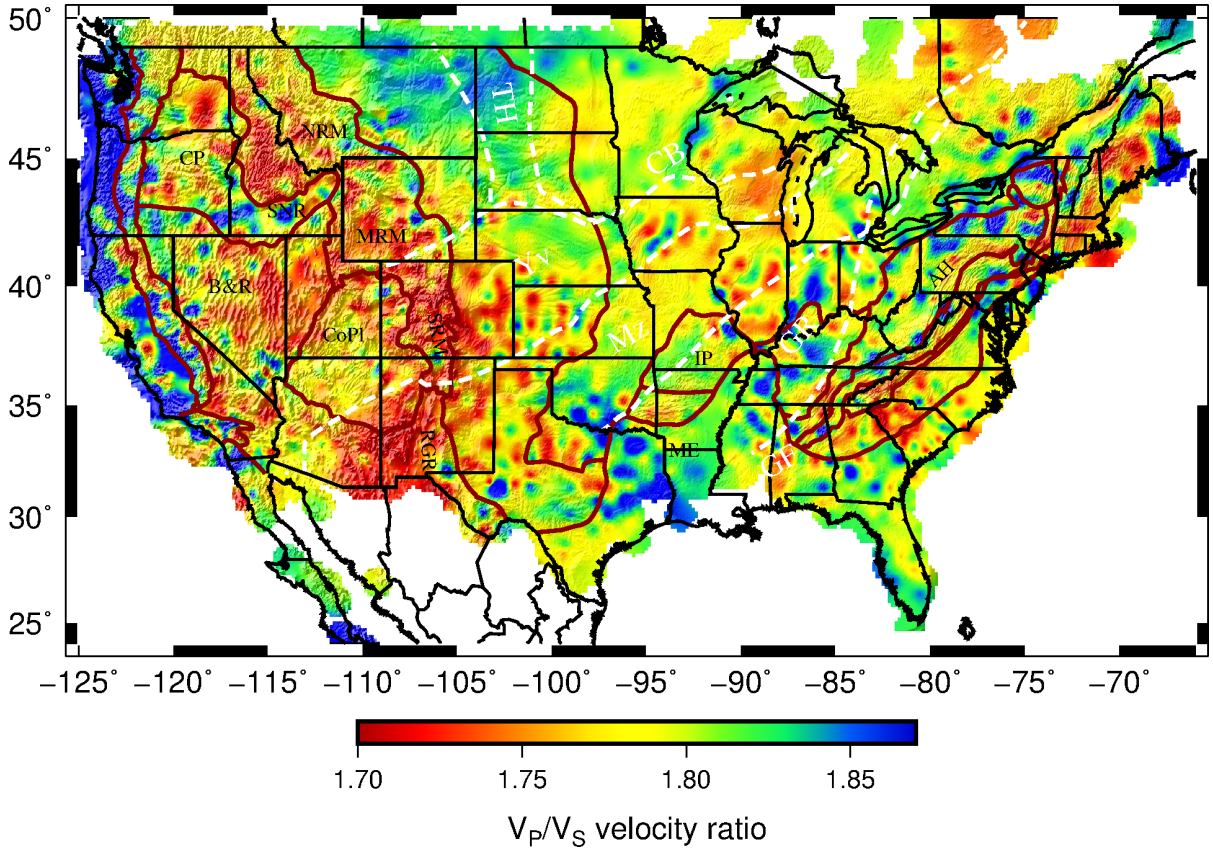

Figure 12: Map of jointly-inverted bulk crustal v_P/v_S. The averaged v_P/v_S is 1.79. Physiographic and Precambrian basement provinces are as in Figure 11.

Estimates of western U.S. crustal v_P/v_S have been published previously in Lowry & Pérez-Gussinyé (2011) using a precursor to this inversion method, in Buehler & Shearer (2014) using station terms from Pn/Sn tomography, and in Steck et al. (2011) from Pg/Sg tomography. The pattern of variations in Figure 12 is (unsurprisingly) broadly similar to those of Lowry & Pérez-Gussinyé (2011), but with

significant differences in the scaling and some small-scale patterns. Roughly 98% of our v_P/v_S estimates fall between 1.7 and 1.9, whereas ~15% of the estimates in Lowry & Pérez-Gussinyé (2011) are over 1.9. We attribute the change to improved characterization of the density parameters by the switch to stochastic inversion described in section 2.4. v_P/v_S is poorly constrained by receiver function seismic constraints alone (see e.g. Figure 9), making the gravity constraint an important contributor to the final estimate. As a consequence however, the $\partial\rho/\partial\kappa$ density parameter plays a pivotal role in "scaling" the pattern of variation of v_P/v_S. The stochastic inversion approach yields larger density parameters that are more similar to those one would infer from laboratory measurements (Figure 5), resulting in a steeper slope for gravity confidence intervals on the (H, κ) parameter space (e.g., Figure 10b) and a tighter resulting range (and corresponding reduced variance) of v_P/v_S. Where the models overlap, the overall pattern of variation of bulk crustal v_P/v_S is very similar to that of Lowry & Pérez-Gussinyé (2011) despite the difference in variance, and they differ by only 0.04 ± 0.05 (i.e., within measurement uncertainties). However the reduced overall variance of this model is encouraging in that the vast majority of estimates fall within the range encompassed by measurements of crustal rocks (Figure 5a). Both Buehler & Shearer (2014) and Steck et al. (2011) noted some similarities in patterns of their v_P/v_S estimates to those of Lowry & Pérez-Gussinyé (2011), but both also noted significant discrepancies, the origins and significance of which are unclear.

The average v_P/v_S of the study area is 1.79. Low v_P/v_S (<1.75) is prevalent in the southern Rocky Mountains, Rio Grande rift, northern Rocky Mountains and northern Basin and Range provinces. The western half of the Colorado Plateau has an intermediate v_P/v_S ~1.8, while the eastern Colorado Plateau is nearer 1.72. The Snake River plain and oceanic-derived terranes along the Pacific coast have high v_P/v_S ~1.83-1.88. The northwestern Basin and Range, central Wyoming and northeastern Snake River plain have locally much higher v_P/v_S than surrounding regions where tomography studies find low shear velocity in the lower crust (Wagner et al., 2012; Schmandt et al., 2015), suggesting some high v_P/v_S may reflect lower crustal melts. v_P/v_S is generally high in the northern Great Plains, and lower in the southern and eastern Granite Rhyolite provinces except near strong gravity highs such as those of the southern Oklahoma Aulacogen and the Midcontinent rift, which have very high v_P/v_S. The Mississippi Embayment has generally high v_P/v_S and high v_P/v_S pockets are also observed in the Appalachian Highlands, while eastward from there to the Piedmont v_P/v_S is relatively low.

2.11 Model Uncertainty

Uncertainties of the crustal thickness and v_P/v_S estimates are given in Figures 13 and 14, respectively. Uncertainties are derived from the optimal interpolation procedure, which in turn uses the variogram spatial statistics (Figure 9) of the measurements at individual seismic sites to estimate both the interpolation weights for the expected value of a field and the estimate uncertainty. The error estimates

are not comprehensive in that they neglect potential bias error that may arise from, e.g., an incorrect assumption of crustal v_P in generating our synthetic receiver functions. Optimal interpolation variance is given by the sum of the interpolation weights multiplied by the variogram variance expected for the distance between the interpolation point and the site associated with that weight, plus a slack variable that results from requiring interpolation weights to sum to one (e.g., Davis, 1986). The weights are naturally largest for the nearest sites, so uncertainties in Figures 13 and 14 approximately reflect the variogram estimate (Figure 9) at the distance corresponding to the nearest seismic site.

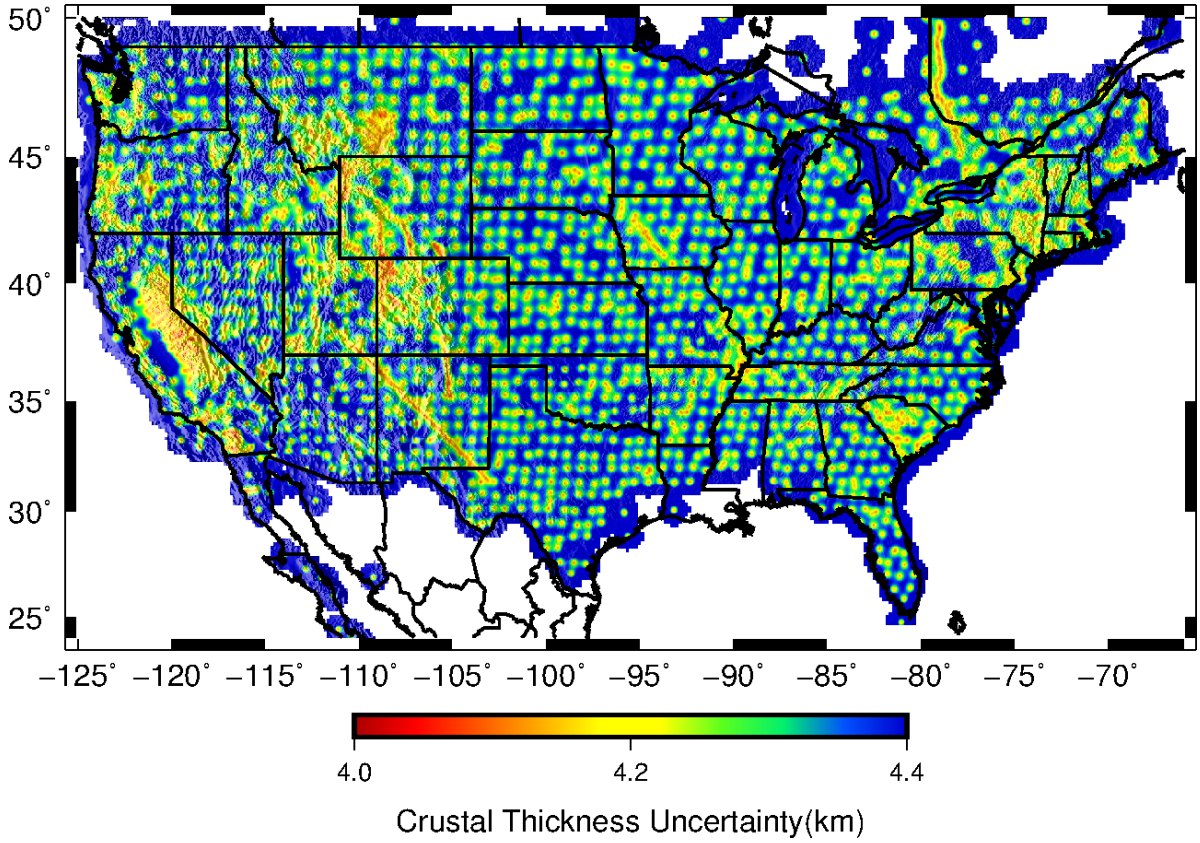

Figure 13: One-sigma uncertainty of crustal thickness. Uncertainty is estimated from optimal interpolation and hence strongly reflects the variogram statistics (Figure 9) used for interpolation, resulting in uncertainties ~4 km near seismic sites rising to above 4.8 km at distances beyond 70 km from the nearest station.

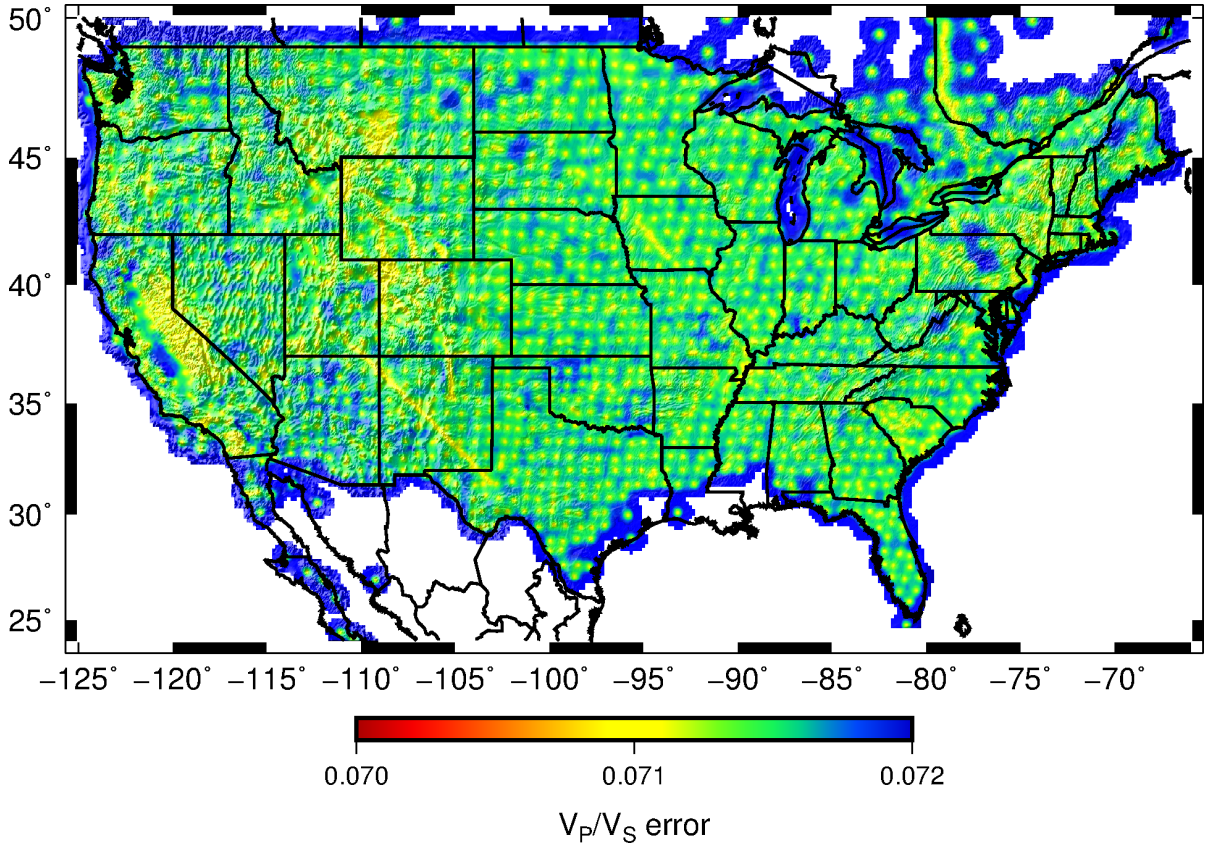

Figure 14: Uncertainty of bulk crustal v_P/v_S. Uncertainty is estimated from optimal interpolation and hence strongly reflects the variogram statistics (Figure 9) used for interpolation, resulting in uncertainties ~0.070 near seismic sites rising to above 0.073 at distances beyond 70 km from the nearest station.

2.12 Gravity Models

Estimation of the bulk crustal density and thickness contributions to observed Bouguer gravity is another significant result of this analysis. Figure 15 shows the gravity models associated with crustal thickness and v_P/v_S, calculated using the final

inverted density parameters of $\Delta\rho_{\text{Moho}}$ = 244 kg/m^3 and $\partial\rho/\partial(v_P/v_S)$ = 1212 kg/m^3. The density parameter estimates are much larger than those found by Lowry & Pérez-Gussinyé (2011), which were 115 and 460 kg/m^3 respectively. Density parameters found here are much closer to values expected based on laboratory and geophysical investigations because of the stochastic inversion approach used in this analysis (section 2.4). The Moho density contrast is nevertheless lower than, e.g., the 410 kg/m^3 reference value assumed for North America in Mooney & Kaban (2010). Interestingly, the variance of the gravity associated with crustal composition implicit in v_P/v_S is slightly larger than that associated with crustal thickness: the root-mean square (RMS) of the gravity models are 58.9 mGal from crustal thickness variation and 60.0 mGal from v_P/v_S. This suggests that compositional density variations are a very significant (if not the largest) fraction of the total mass balance, and that it must be correctly accounted for in studies of elevation and lithospheric stress (e.g., Becker et al., 2014).

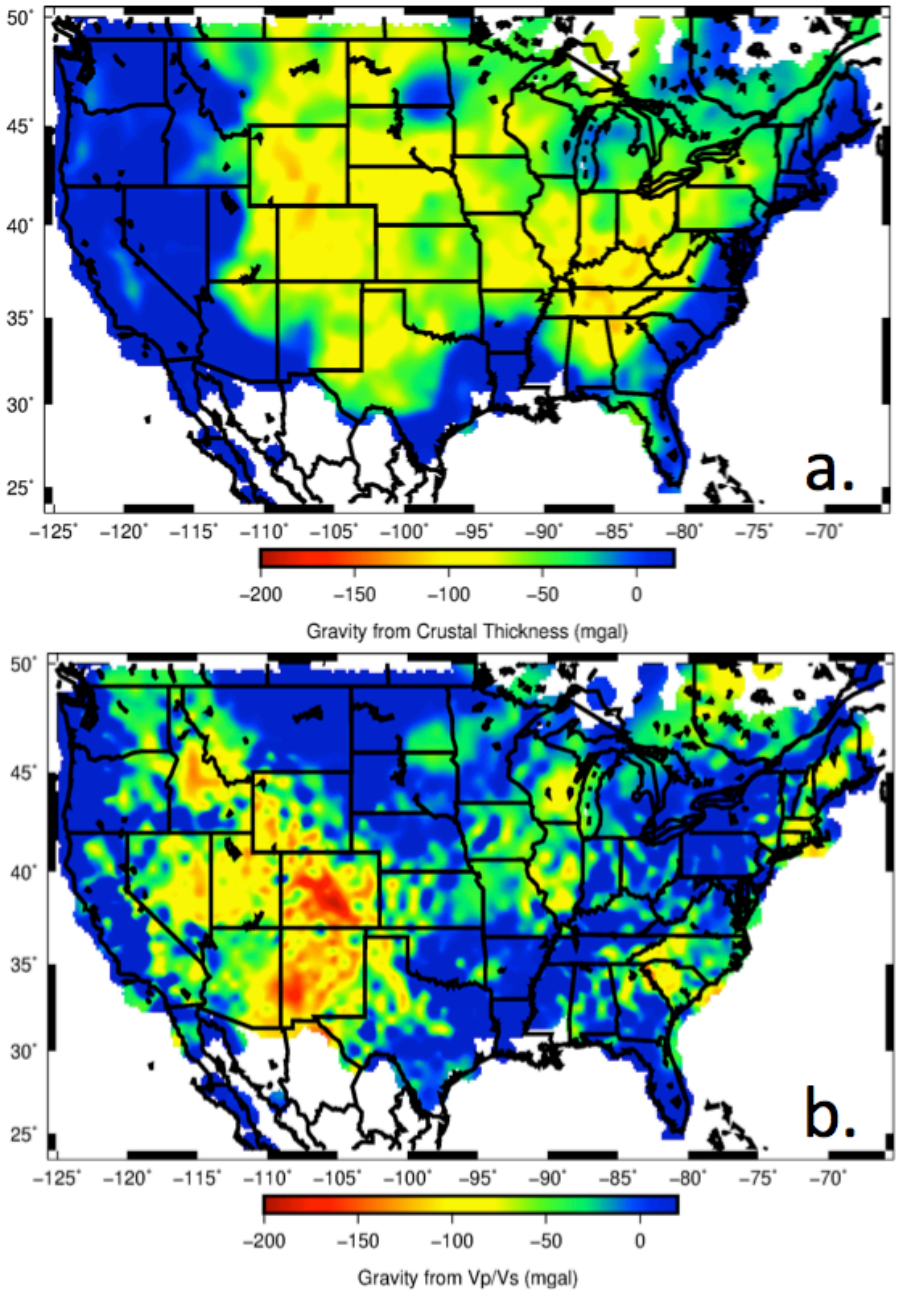

Figure 15: Modeled Bouguer gravity anomaly. Bouguer gravity anomaly modeled from crustal thickness (a) and v_P/v_S (b). Gravity maps have been shifted by a datum corresponding to the difference between observed gravity and the (zero-mean) models.

The residual Bouguer gravity after subtraction of contributions from crustal thickness, bulk compositional density and thermal variations is shown in Figure 16. The residual is greatly reduced, with RMS 56 mGal, relative to the 78 mGal RMS of the observed Bouguer gravity and a 112 mGal residual associated with the starting model derived from receiver function cross-correlation stacking. The residual gravity anomalies are likely dominated by asthenospheric mantle mass variations that our model does not account for (e.g., Becker et al., 2014; 2015) and sphericity of the Earth, which produces anomalies that differ by up to tens of mGal from the Cartesian calculations used here on the scale of the conterminous U.S. The largest residuals appear to be dominated by a systematic pattern of greater asthenospheric mantle buoyancy in the west, resulting in residual anomalies mostly in the range of –150 to 50 mGal in the western U.S., but in the range –50 to 200 mGal in the east. Schmandt et al. (2015) inferred a ~200 kg/m^3 higher $\Delta\rho_{\text{Moho}}$ west of –105°E longitude than in the eastern U.S., based on differences in the slope of crustal thickness versus elevation. We examined this hypothesis by separately inverting for the density contrast for the two halves, and found that gravity is best-fit with a Moho density contrast that is 63 kg/m^3 smaller in the east than in the west (Figure 17). There are other components of our model that might account for our east-west difference not being as large as that in Schmandt et al. (2015): For example, our crustal v_P/v_S is noticeably lower on average in the west than in the east (Figure 12). If a roughly 0.08 mean difference in v_P/v_S were added to the Moho density contrast, it would increase the difference in eastern and western $\Delta\rho_{\text{Moho}}$ by ~100 kg/m^3. On

the other hand, the western U.S. mantle at 60 km depth averages 103°C hotter than in the east in our thermal model, which would translate to a 12 kg/m^3 reduction in the difference in eastern and western $\Delta\rho_{\text{Moho}}$.

The residual anomalies also may be amplified by melts present in the crust. For example, the High Lava Plains and northwestern Basin and Range exhibits high v_P/v_S ratio (>1.9) associated with low observed Bouguer gravity where shear wave velocities and electrical conductivity indicate a lower crustal melt fraction as high as 3% (Wagner et al., 2012; Meqbel et al., 2014). Partial melt raises the v_P/v_S with no corresponding increase in crustal density, resulting in a density derivative with opposite sign to the compositional trend that dominates our estimate of the density derivative. Consequently, the assumed constant density derivative overestimates the crustal compositional gravity anomaly where melt increases v_P/v_S.

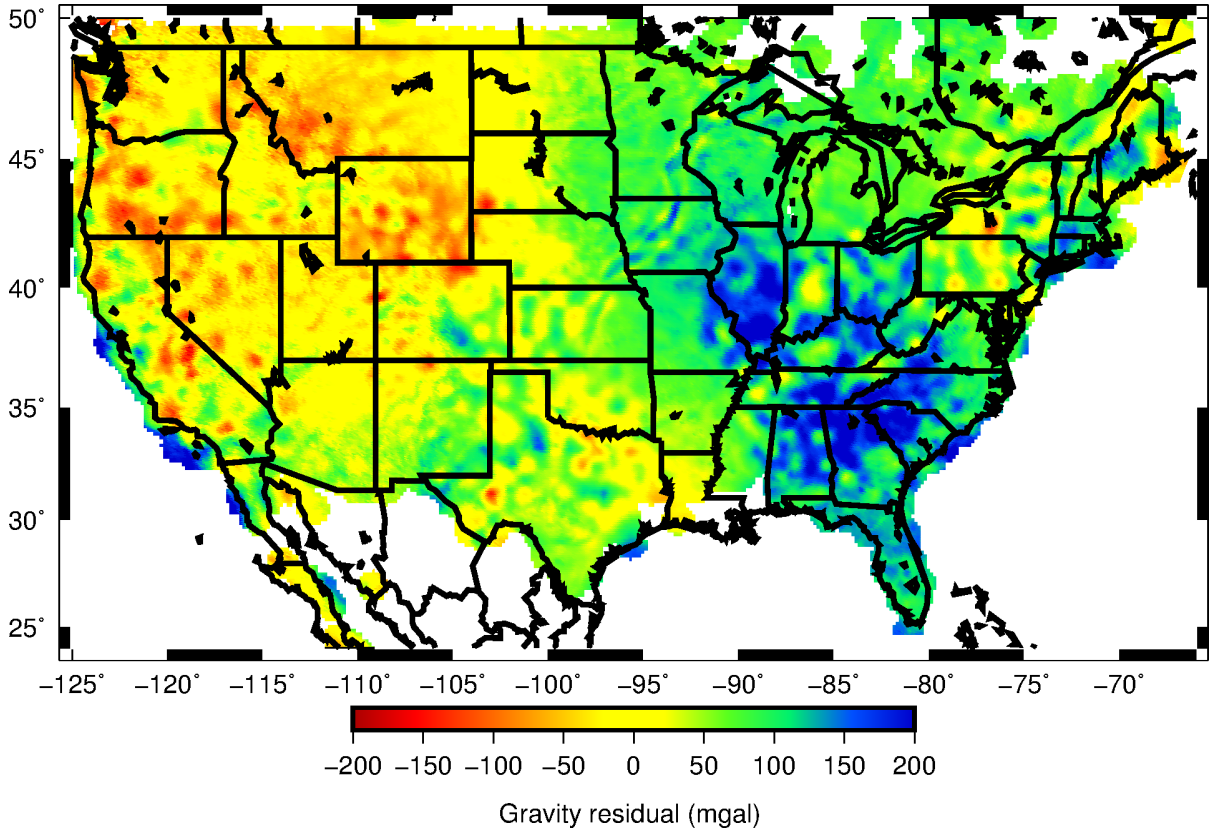

Figure 16: Residual Bouguer gravity after subtracting model contributions from Moho density contrast, crustal compositional variation implicit in v_P/v_S, and thermal variations.

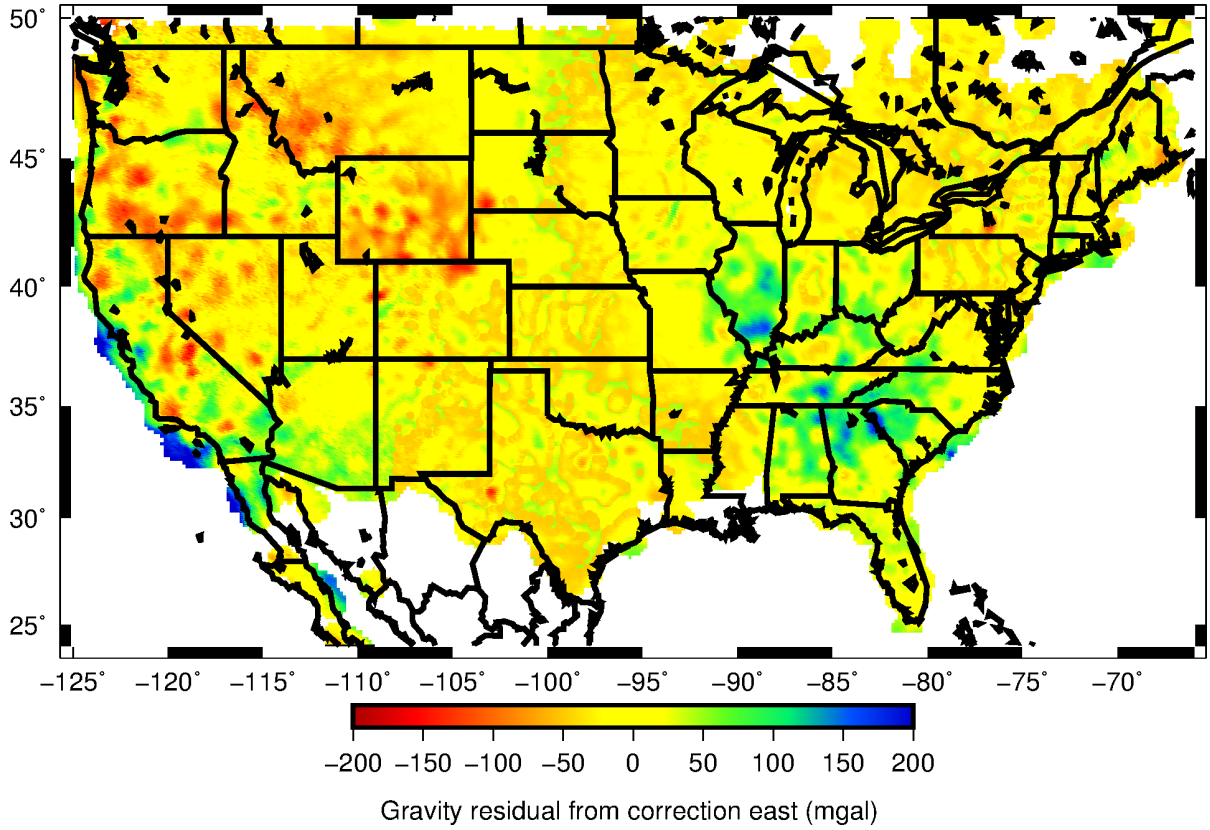

Figure 17: Residual Bouguer gravity after estimating the Moho density contrast separately for the eastern and western United States. Western U.S. gravity anomalies are similar to Figure 16, dominated by negative anomalies in the northern and middle Rocky Mountains and northern Basin and Range. However previously large positive anomalies in the eastern U.S. are greatly reduced, with most less than 100 mGal.

2.13. Mineral Physics Modeling

The chemical composition and mineralogical makeup of continental crust has been examined for decades but remains a significant challenge (Rudnick & Fountain, 1995; Rudnick & Gao, 2003; Hacker et al., 2015). Sparse (and potentially biased) xenolith sampling of both localities and depth raises questions about how well the potential variability of deep continental crust is understood. Seismic imaging of the crust clearly has great potential for illuminating deep crustal variability, but is subject to its own limitations and ambiguities (Christensen & Mooney, 1995; Christensen, 1996). However, variations in the seismic velocity ratio v_P/v_S of crustal rocks, because of its insensitivity to temperature and comparatively high sensitivity to composition (and especially quartz content), shows some promise as an investigative tool for exploring crustal compositional variation (Christensen, 1996; Lowry & Pérez-Gussinyé, 2011).

To more fully understand the possible implications of v_P/v_S and associated density variations for deep crustal composition and mineralogy, we used the thermodynamic model Perple_X (Connolly, 2009). Perple_X's thermodynamical modeling of (pressure-, temperature, and chemistry-dependent) mineral equations of state calculates the likely assemblage of minerals using a linear programming minimization of the Gibbs free energy at given entropy and volume. Our modeling assumes crustal chemistries with weight percentage of components as described in Table 1, assuming three different major element chemistries corresponding to averages for the upper, middle and lower crust, based on Rudnick & Gao (2003).

The thermodynamical database is identical to that of Holland & Powell (1998). The mineral solution (Dale et al., 2000; Holland & Powell, 1996, 1998, 2001, 2003; White et al., 2001) is included in Appendix.

Guerri et al. (2015) earlier used Perple_X to examine how hydration state of crustal chemistries influenced geophysical properties of seismic velocity and density. Although the seismic velocity ratio was not a primary target for their analyses, they did note in passing that hydration reduces v_P/v_S. Our modeling is undertaken here to replicate their result, to examine why v_P/v_S decreases (e.g., address how much is related to increased abundance of quartz versus changes to velocity properties of other minerals), and to more fully understand how hydration affects other physical properties of the crust including temperature.

Table 1

Crustal chemical composition: Average chemistry of upper, middle and lower continental crust from Rudnick & Gao (2003), used in modeling for this paper.

Wt-%	Na_20	MgO	Al_2O_3	SiO_2	K_2O	FeO	CaO
upper crust	3.27	2.48	15.4	66.62	2.8	3.59	5.04
middle crust	3.39	3.59	15.00	63.5	2.3	5.25	6.02
lower crust	2.65	7.24	16.9	53.4	0.61	9.59	8.57

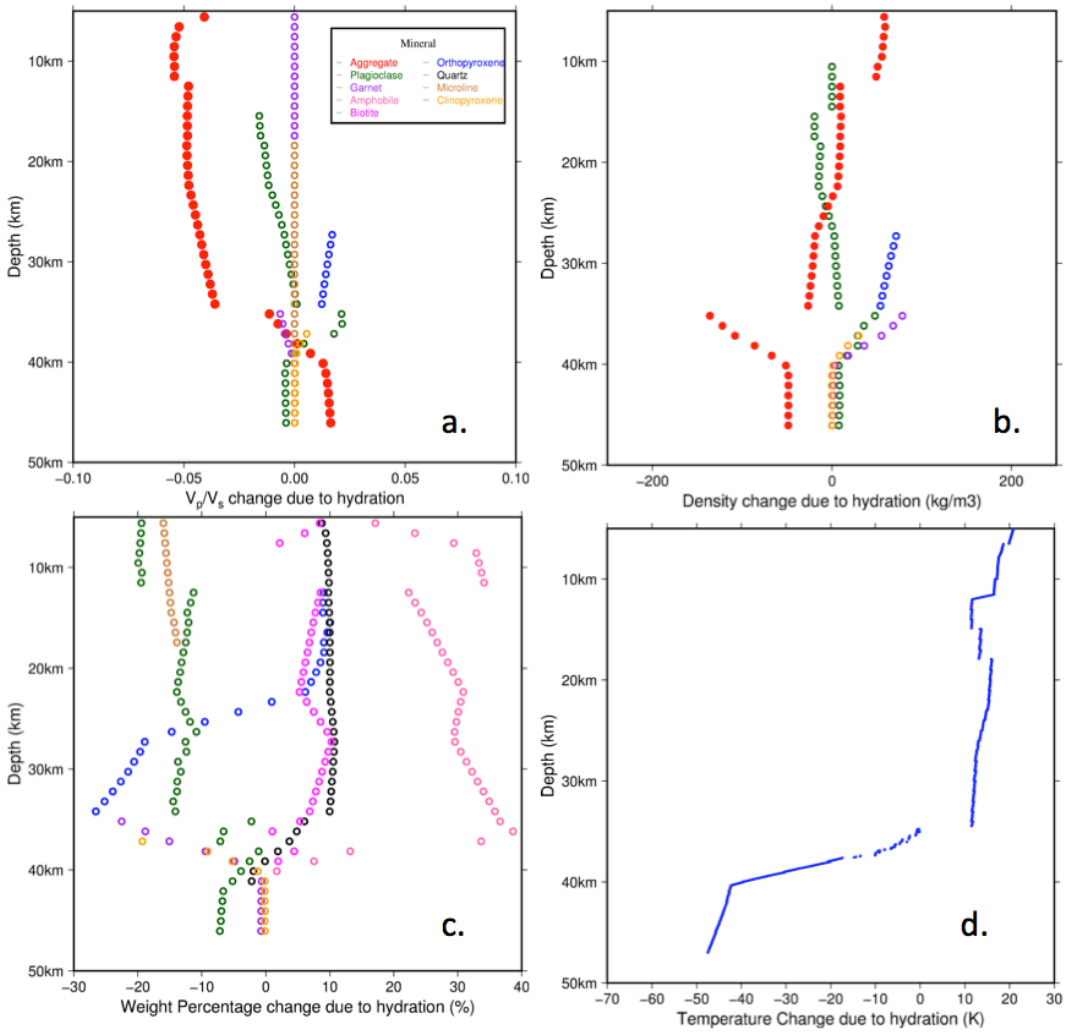

Figure 18: Mineral physics modeling. Perple_X modeling (Connolly, 2009) assumes a mid-crustal chemistry with and without 1 wt-% of water. (a) v_P/v_S; (b) density; (c) wt-% mineral constituents; (d) temperature difference for hydrated minus dry assemblages, representing change of mineral enthalpy after adding 1 wt-% water content, assuming no change in original entropy. Red symbols represent aggregate properties. The high v_P/v_S at 30 km depth is due to partial melt, which is below the Moho at the Basin and Range location of the geotherm used here.

We compute the mineral assemblage as a function of *P*-*T* from geothermal with revised thermodynamic data, which is identical to Holland & Powell (1998) apart from considering anomalous behavior of quartz in the alpha-beta phase transition. All of our thermodynamical models sampled the crust at 1 km depth intervals using the weight of the crustal column for pressure and geotherms derived from our thermal model (section 2.7). In some models, we interpolated smoothly over depth a changing chemistry based on the layer average chemistries in Table 1; for others we used a constant mid-crustal chemistry in order to more easily distinguish effects of phase boundaries from those of changing chemistry. Figure 18 shows one example of our modeling in which we used a midcrustal chemistry (i.e., no change with depth) and modeled the changes that result with and without a 1 wt-% water constituent included. The thermodynamical modeling predicts the v_P/v_S ratio of a dry chemistry increases gradually with depth from 1.72–1.75 (Figure 18a), as the wt-% of quartz gradually decreases. Adding a 1 wt-% water constituent significantly reduces plagioclase, orthopyroxene and microcline in the aggregate while increasing the quartz constituent by up to 10 wt-%, resulting in a significant reduction of v_P/v_S at all depths except where melt is produced (in this example, below 40 km, but the geotherm used was from the Basin and Range province where the crust is not that thick). The density is also reduced, but the greatest reduction of density occurs deep in the crustal column where garnet is consumed by hydration (consistent with the interpretation of xenoliths from the U.S. Cordillera by Jones et al. (2015)).

The model in Figure 18a predicts a bulk-crustal v_P/v_S near 1.75 for a dry crustal column and 1.65 for hydrated. The average v_P/v_S ratio from our joint inversion is 1.79, which is more consistent with typical values for crustal rocks from lab experiments (Christensen, 1996). The lower model v_P/v_S might reflect some error in equations of state relating to the Poisson's ratio. It is also possible that the chemistry profile from Rudnick & Gao (2003) adopted in the modeling depicted in Figure 14 is not representative of the mean chemistry of North American crust, or that the equations of state specified in the Perple_X modeling are slightly in error. Nevertheless, the primary conclusion we draw from the modeling is liable to be true regardless of chemistry: Hydration increases the abundance of quartz, consumes pyroxenes, feldspars and garnets, and consequently reduces bulk v_P/v_S and density of the crustal column. Hence, low bulk crustal v_P/v_S in Figure 12 can be considered indicative of a hydration event at some point during the evolution of the crust.

Another interesting implication of the Perple_X modeling in Figure 18 is that hydration results in a complicated thermal profile for the crust. Above the ~35 km depth where orthopyroxene and plagioclase break down to form clinopyroxene and garnet, hydration reactions are exothermic and would be expected to raise crustal temperatures by 10–20°C. Below that phase boundary however, hydration reactions are endothermic and would be expected to reduce temperatures by as much as 50°C for 1 wt-% water, largely because of the latent heat of fusion associated with melting of garnet. Hence, hydration of the entire crustal column would be expected to increase surface heat flow by increasing advective heat transfer and raising

temperatures in the shallow crust, while simultaneously lowering temperatures in the lower crust and at the Moho. A large discrepancy between surface heat flow and Pn-derived Moho temperatures has been observed under high elevations of the western U.S. Cordillera (Berry et al., 2015), with colder-than-expected Moho prevalent in regions of the Basin and Range and Rocky Mountains where we observe very low v_P/v_S.

2.14. Discussion

2.14.1 Implications of v_P/v_S

Much of what we know about the compositional variation of continental crust is derived from observations of surface exposures of crystalline basement and sparse xenoliths brought to the surface by volcanism (Rudnick & Fountain, 1995; Hacker et al., 2015; Weber et al., 2002), and these types of studies suggest that regional differences in bulk chemistry are small (of order 1%). Many studies have also examined relationships between mineral composition and seismic velocities (e.g., Miller & Christensen, 1994; Sobolev & Bakeyko, 1994; Christensen & Mooney, 1995; Kern et al., 1996; Musacchio et al., 1997; Hacker et al., 2015), but the temperature and melt-dependence of velocities, plus the wide range of compositions consistent with a given velocity, make interpretation ambiguous.

The seismic velocity ratio, v_P/v_S, also is non-unique with respect to composition and melt, but its relative insensitivity to temperature and high sensitivity

to quartz content makes it a potentially valuable tool for investigation of crustal compositional variation (Christensen & Fountain, 1975; Kern, 1982; Holbrook et al., 1992; Zandt et al., 1994; Christensen, 1996; Lowry & Pérez-Gussinyé, 2011). Guerri et al. (2015) noted that hydration lowers Poisson's ratio (and hence v_P/v_S) based on their results of Perple_X modeling of mineral thermodynamics similar to that performed here. The thermodynamical modeling of mineralogy described here further clarifies that hydration increases the abundance of quartz at the expense of pyroxene, feldspar and mica. This is also consistent with an observed systematic relationship observed between v_P/v_S and depth to the subducting plate interface in Cascadia (Audet & Bürgmann, 2014), which had been interpreted as evidence of progressive quartz precipitation and mineralization in veins but more likely reflects hydration state of the overlying crust. Hence, greater quartz abundance evidenced by lower crustal v_P/v_S may prove a reliable indicator of hydration history of the crust.

Viewed from that perspective, Figure 12 can be considered as at least partly reflecting the hydration state of the crust. This has implications that may extend far beyond just processes of volatile transfer through the crust. For example, hydration state is one of the primary factors determining rheological strength of rocks in the ductile flow regime (e.g., Mackwell et al., 1985; Bürgmann & Dresen, 2008). Hydration also affects density (Figure 18b), most significantly by consuming garnet in lower crustal *P-T* conditions.

Jones et al. (2015) cited hydration observed in a handful of lower crustal xenoliths as evidence that hydration and resulting expansion of the lower crust may

be responsible for a significant fraction of elevation of the western United States Cordillera following the Laramide flat slab episode. This interpretation is supported by the imaging results and modeling described in this paper. Moreover, it raises some interesting possible implications for the nature of Laramide-style, thick-skin contractional tectonics. The curious nature of such tectonism, characterized by high-angle thrust faulting at odd and highly variable angles to any presumptive regional plate-tectonic stress geometry, makes some sense if we recognize that these structures are found almost exclusively in the vicinity of flat-slab style subduction and may actually reflect a response to simultaneous weakening and volumetric expansion of lower crustal mineral assemblages by hydration. Such a hypothesis raises other questions however, including what volumes of hydrous mass transport are needed to achieve widespread hydration of a significant fraction of the crust in these regions, and how such widespread volatile transport would affect thermal transport through the crust.

The thermodynamical modeling result suggesting that temperatures are reduced by hydration in the lower crust but increased in the upper crust (Figure 18d) is especially intriguing in light of observations that, in regions of high Cordilleran elevation, Moho temperatures derived from Pn velocities are much lower than one would anticipate based on conductive thermal modeling of surface heat flow measurements (Berry et al., 2015). If hydration reaction thermodynamics turns out to be an observable phenomenon, this would provide a potentially useful constraint on the timing of hydration. Much of the low v_P/v_S observed in Figure 12 is found in

regions where hydration undoubtedly occurred long ago (e.g., in the Appalachian Piedmont to Valley and Ridge; Interior Plains central lowlands and adjacent to the Midcontinent rift). The timescale for conductive thermal transport through the lithosphere is roughly 100 million years, so observing a thermal signature associated with hydration reactions would imply that the hydration event is more recent than that.

2.15. Conclusions

Receiver function estimates of thickness and seismic velocity ratios, v_P/v_S, of U.S. continental crust within the EarthScope footprint are greatly improved by joint inversion with likelihood filters derived from gravity modeling and spatial statistics. Crustal thickness averaged over the conterminous U.S. is 38.9 km, and averaged v_P/v_S is 1.79.

Crustal thickness (Figure 11) exhibits many interesting relationships to physiographic and basement provinces, even in the central and eastern U.S. where these are not forced by active tectonism. Crust is thickest in the southern Rocky Mountains and Appalachian Highlands, consistent with earlier inferences from seismic refraction surveys (Braile et al., 1989; Taylor, 1989) as well as with other tomographic and receiver function models derived from EarthScope data (Shen et al., 2016; Schmandt et al., 2015).

As measured by modeled contributions to the variance of gravity, the largest contributor to mass variation in the U.S. lithosphere is compositional variation within

the crust, followed by variations in crustal thickness and finally geothermal variations. After subtracting gravity anomalies due to crustal composition, thickness and thermal variation from measured Bouguer gravity, most of the residual gravity is likely related to mantle density variations (e.g., Becker et al., 2014), although some residual gravity anomalies may be amplified by the presence of crustal melts. The gravity residual is reduced if we allow for differences in Moho density contrast in the eastern (172 kg/m^3) and western (235 kg/m^3) United States, similar to that previously proposed by Schmandt et al. (2015).

Modeling of the thermodynamics of mineral formation suggests that hydration of crustal mineral assemblages significantly impacts several geophysical properties that may be observable by geophysical remote sensing methods. Hydration increases the abundance of quartz (Figure 18c), which reduces the seismic velocity ratio in the middle and upper crust (Figures 5 and 18a). Hydration also reduces density in the lower crust by consuming garnet (Figure 18b). Consequently, water derived from dehydration of the Farallon slab during its Laramide phase of flattened geometry (Humphreys et al., 2003) may be partly responsible for post-Laramide elevation of the Intermountain western U.S. (e.g., Jones et al., 2015). Finally, hydration reactions are exothermic in the upper crust, which would express as enhanced surface heat coincident with low crustal v_P/v_S (as observed by Lowry & Pérez-Gussinyé (2011)). However, hydration is endothermic in the lower crust where garnets are consumed to form melts, which should cool the Moho and may result in large discrepancies between Pn-derived estimates of Moho temperature and

predictions of deep temperature derived from surface heat flow in regions of high elevation (Berry et al., 2015).

Acknowledgments

All USArray and other U.S. seismic receiver functions were acquired from the EarthScope Automated Receiver Survey (EARS) (Crotwell & Owens, 2005; IRIS DMC, 2010; Trabant et al., 2012). Bouguer gravity data are from the WGM2012 International Gravimetric Bureau global map (Balmino et al., 2011; Bonvalot et al., 2012). Eric Lyman performed some preliminary Perple_X modeling suggesting the impact of hydration on quartz abundance for an undergraduate thesis (Lyman, 2016). This project was supported by National Science Foundation grants EAR-0955909, EAR-1246977, and EAR-1358622 from the Geophysics and EarthScope science programs.

References

Afonso, J. C., G. Ranalli, & M. Fernandez (2005). Thermal expansivity and elastic properties of the lithospheric mantle: results from mineral physics of composites. *Physics of the Earth and Planetary Interiors*, *149*(3), 279-306. https://doi.org/10.1016/j.pepi.2004.10.003

Ammon, C. J. (1991). The isolation of receiver effects from teleseismic P waveforms. *Bulletin of the Seismological Society of America*, *81*(6), 2504-2510.

Audet, P., & R. Bürgmann (2014). Possible control of subduction zone slow-earthquake periodicity by silica enrichment. *Nature*, *510*(7505), 389-392. https://doi.org/10.1038/nature13391.

Balmino, G., N. Vales, S. Bonvalot, & A. Briais (2011). Spherical harmonic modeling to ultra-high degree of Bouguer and isostatic anomalies. *Journal of Geodesy*, *86*(7), 499-520. https://doi.org/10.1007/s00190-011-0533-4.

Beck, J. V. & K. J. Arnold (1977). *Parameter Estimation in Engineering and Science*. John Wiley & Sons, New York.

Becker, T. W., C. Faccenna, E. D. Humphreys, A. R. Lowry, & M. S. Miller (2014). Static and dynamic support of western United States topography. *Earth and Planetary Science Letters*, *402*, 234-246. https://doi.org/10.1016/j.epsl.2013.10.012.

Becker, T. W., A. R. Lowry, C. Faccenna, B. Schmandt, A. Borsa, & C. Yu (2015). Western US intermountain seismicity caused by changes in upper mantle flow. *Nature*, *524*(7566), 458-461. https://doi.org/10.1038/nature14867.

Berry, M. A., A. R. Lowry, & D. L. Schutt (2015). Cold and wet at the roots of U.S. Cordilleran high elevation. Abstr. #T11C-2910, AGU Fall Meeting, San Francisco CA.

Bonvalot, S., G. Balmino, A. Briais, M. Kuhn, A. Peyrefitte, N. Vales, R. Biancale, G. Gabalda, F. Reinquin, & M. Sarrailh (2012). World Gravity Map, *Bureau Gravimetrique International* (*BGI*), Map, CGMW-BGI-CNES728, IRD, Paris.

Braile, L. W., W. J. Hinze, R. R. B. Von Frese, & G. R. Keller (1989). Seismic properties of the crust and uppermost mantle of the conterminous United States and adjacent Canada. *Geological Society of America Memoirs*, *172*, 655-680, https://doi.org/10.1130/MEM172-p655.

Buehler, J. S., & P. M. Shearer (2014), Anisotropy and v_P/v_S in the uppermost mantle beneath the western United States from joint analysis of Pn and Sn phases. *Journal of Geophysical Research*, *119*(2), 1200-1219. https://doi.org/10.1002/2016JB013265.

Buehler, J. S., & P. M. Shearer (2017), Uppermost mantle seismic velocity structure beneath USArray, *Journal of Geophysical Research*, in press. https://doi.org/10.1002/2016JB013265.

Bürgmann, R., & G. Dresen (2008). Rheology of the lower crust and upper mantle: Evidence from rock mechanics, geodesy, and field observations. *Annual Reviews of Earth and Planetary Sciences*, *36*, 531-567. https://doi.org/10.1146/annurev.earth.36.031207.124326.

Christensen, N. I. (1996). Poisson's ratio and crustal seismology. *Journal of Geophysical Research*, *101*(B2), 3139-3156. https://doi.org/10.1029/95JB03446

Christensen, N. I., & D. M. Fountain (1975). Constitution of the lower continental crust based on experimental studies of seismic velocities in granulite. *Geological Society of America Bulletin*, *86*(2), 227-236. https://doi.org/10.1130/0016-7606(1975)86%3C227:COTLCC%3E2.0.CO;2

Christensen, N., & W. Mooney (1995). Seismic velocity structure and composition of the continental crust: A global view. *Journal of Geophysical Research*, *100*(B6), 9761-9788. https://doi.org/10.1029/95JB00259.

Connolly, J. A. D. (2009). The geodynamic equation of state: what and how. *Geochemistry, Geophysics, Geosystems*, *10*(10). https://doi.org/10.1029/2009GC002540.

Crotwell, H. P., & T. J. Owens (2005). Automated receiver function processing. *Seismological Research Letters*, *76*(6), 702-709. https://doi.org/10.1785/gssrl.76.6.702.

Dale, J., Holland, T. & Powell, R. (2000). Hornblende–garnet–plagioclase thermobarometry: a natural assemblage calibration of the thermodynamics of hornblende. *Contributions to Mineralogy and Petrology, 140*(3), 353-362. https://doi.org/10.1007/s004100000187

Davis, J. C. (1986). *Statistics and Data Analysis in Geology* (2nd edn). Wiley, New York.

DePaolo, D. J., T. E. Cerling, S. R. Hemming, A. H. Knoll, F. M. Richter, L. H. Royden, R. L. Rudnick, L. Stixrude, & J. S. Trefil (2008). *Origin and Evolution of Earth: Research Questions for a Changing Planet*. National Academies Press, Washington D.C.

Dziewonski, A. M., & D. L. Anderson (1981). Preliminary reference Earth model. *Physics of the Earth and Planetary Interiors*, *25*(4), 297-356. https://doi.org/10.1016/0031-9201(81)90046-7

Ehlers, T. A. (2005). Crustal thermal processes and the interpretation of thermochronometer data. *Reviews of Mineralogy and Geochemistry, 58*(1), 315-350. https://doi.org/10.2138/rmg.2005.58.12

Guerri, M., F. Cammarano, & J. A. Connolly (2015). Effects of chemical composition, water and temperature on physical properties of continental crust. *Geochemistry, Geophysics, Geosystems*, *16*(7), 2431-2449. https://doi.org/10.1002/2015GC005819.

Hacker, B. R., P. B. Kelemen, & M. D. Behn (2015). Continental lower crust. *Annual Reviews of Earth and Planetary Sciences*, *43*, 167-205. https://doi.org/10.1146/annurev-earth-050212-124117.

Holbrook, W. S., W. D. Mooney, & N. I. Christensen (1992). The seismic velocity structure of the deep continental crust. In D. M. Fountain, R. Arculus, R. W. Kay (Eds.), *Continental Lower Crust*, pp. 1–43, Elsevier Sci., New York.

Holland, T. & Powell, R. (1996). Thermodynamics of order-disorder in minerals: II. Symmetric formalism applied to solid solutions. *American Mineralogist, 81*(11-12), 1425-1437. https://doi.org/10.2138/am-1996-11-1215

Holland, T. J. B., & Powell, R. (1998). An internally consistent thermodynamic data set for phases of petrological interest. *Journal of Metamorphic Geology, 16*(3), 309-343. https://doi.org/10.1111/j.1525-1314.1998.00140.x

Holland, T. I. M. & Powell, R. (2001). Calculation of phase relations involving haplogranitic melts using an internally consistent thermodynamic dataset. *Journal of Petrology, 42*(4), 673-683. https://doi.org/10.1093/petrology/42.4.673

Holland, T. & Powell, R. (2003). Activity–composition relations for phases in petrological calculations: an asymmetric multicomponent formulation. *Contributions to Mineralogy and Petrology, 145*(4), 492-501. https://doi.org/10.1007/s00410-003-0464-z

Humphreys, E., E. Hessler, K. Dueker, G. L. Farmer, E. Erslev, & T. Atwater (2003). How Laramide-age hydration of North American lithosphere by the Farallon slab controlled subsequent activity in the western United States. *International Geology Review*, 45(7), 575-595. https://doi.org/10.2747/0020-6814.45.7.575.

IRIS DMC (2010). *Data Services Products: EARS EarthScope Automated Receiver Survey*. https://doi.org/10.17611/DP/EARS.1

Ito, T., & M. Simons (2011). Probing asthenospheric density, temperature, and elastic moduli below the western United States. Science, 332(6032), 947-951. https://doi.org/10.1126/science.1202584

Jones, C. H., K. H. Mahan, L. A. Butcher, W. B. Levandowski, & G. L. Farmer (2015). Continental uplift through crustal hydration. *Geology*, *43*(4), 355-358. https://doi.org/10.1130/G36509.1.

Julià, J. (2007). Constraining velocity and density contrasts across the crust—mantle boundary with receiver function amplitudes. *Geophysical Journal International*, *171*(1), 286-301, https://doi.org/10.1111/j.1365-2966.2007.03502.x

Kern, H. (1982). Elastic-wave velocity in crustal and mantle rocks at high pressure and temperature: The role of the high-low quartz transition and of dehydration reactions. *Physics of the Earth and Planetary Interiors*, *29*(1), 12-23. https://doi.org/10.1016/0031-9201(82)90133-9

Kern, H., S. Gao, & Q. S. Liu (1996). Seismic properties and densities of middle and lower crustal rocks exposed along the North China Geoscience Transect. *Earth and Planetary Science Letters*, *139*(3-4), 439-455. https://doi.org/10.1016/0012-821X(95)00240-D

Kohlstedt, D. L. (2006). The role of water in high-temperature rock deformation. *Reviews of Mineralogy and Geochemistry*, *62*(1), 377-396. https://doi.org/10.2138/rmg.2006.62.16.

Kono, Y., A. Miyake, M. Ishikawa, & M. Arima (2008). Temperature derivatives of elastic wave velocities in plagioclase (An51±1) above and below the order-disorder transition temperature. *American Mineralogist*, *93*(4), 558-564. https://doi.org/10.2138/am.2008.2591

Levander, A., & M. S. Miller (2012). Evolutionary aspects of lithosphere discontinuity structure in the western US. *Geochemistry, Geophysics, Geosystems*, *13*(7). https://doi.org/10.1029/2012GC004056.

Ligorría, J. P., & C. J. Ammon (1999). Iterative deconvolution and receiver-function estimation. *Bulletin of the Seismological Society of America*, *89*(5), 1395-1400.

Lin, F. C., B. Schmandt, & V. C. Tsai (2012). Joint inversion of Rayleigh wave phase velocity and ellipticity using USArray: Constraining velocity and density structure in the upper crust. *Geophysical Research Letters*, *39*(12). https://doi.org/10.1029/2012GL052196

Lowry, A. R., & M. Pérez-Gussinyé (2011). The role of crustal quartz in controlling Cordilleran deformation. *Nature*, *471*(7338), 353-357. https://doi.org/10.1038/nature09912

Lowry, A. R., N. M. Ribe, & R. B. Smith (2000). Dynamic elevation of the Cordillera, western United States. *Journal of Geophysical Research*, *105*(B10), 23371-23390. https://doi.org/10.1029/2000JB900182

Lyman, E. (2016). *Mineral Physics Modeling of the Effect of Water on Crustal Seismic Velocity Ratios*. (undergraduate research thesis) Utah State University.

Mackwell, S. J., D. L. Kohlstedt, & M. S. Paterson (1985). The role of water in the deformation of olivine single crystals. *Journal of Geophysical Research*, *90*(B13), 11319-11333. https://doi.org/10.1029/JB090iB13p11319.

Martinec, Z. (1994). The density contrast at the Mohorovičic discontinuity. *Geophysical Journal International*, *117*(2), 539-544. https://doi.org/10.1111/j.1365-246X.1994.tb03950.x

McCurry, M., & D. W. Rodgers (2009). Mass transfer along the Yellowstone hotspot track I: Petrologic constraints on the volume of mantle-derived magma. *Journal of Volcanology and Geothermal Research*, *188*(1), 86-98. https://doi.org/10.1016/j.jvolgeores.2009.04.001.

Meqbel, N. M., G. D. Egbert, P. E. Wannamaker, A. Kelbert, & A. Schultz (2014). Deep electrical resistivity structure of the northwestern US derived from 3-D inversion of USArray magnetotelluric data. *Earth and Planetary Science Letters, 402*, 290-304. https://doi.org/10.1016/j.epsl.2013.12.026.

Miller, D. J., & N. L. Christensen (1994). Seismic signature and geochemistry of an island arc: A multidisciplinary study of the Kohistan accreted terrane, northern Pakistan. *Journal of Geophysical Research*, *99*(B6), 11623-11642. https://doi.org/10.1029/94JB00059

Mooney, W. D., & M. K. Kaban (2010). The North American upper mantle: Density, composition, and evolution. *Journal of Geophysical Research*, *115*(B12). https://doi.org/10.1029/2010JB000866.

Musacchio, G., W. D. Mooney, J. H. Luetgert, & N. I. Christensen (1997). Composition of the crust in the Grenville and Appalachian Provinces of North America inferred from v_P/v_S ratios. *Journal of Geophysical Research*, *102*(B7), 15225-15241. https://doi.org/10.1029/96JB03737.

Niu, F., & D. E. James (2002). Fine structure of the lowermost crust beneath the Kaapvaal craton and its implications for crustal formation and evolution. *Earth and Planetary Science Letters*, *200*(1), 121-130. https://doi.org/10.1016/S0012-821X(02)00584-8.

Pakiser, L. C. (1989). Geophysics of the Intermontane system. *Geological Society of America Memoirs*, *172*, 235-248. https://doi.org/10.1130/MEM172-p235.

Porter, R., Y. Liu, & W. E. Holt (2016). Lithospheric records of orogeny within the continental U.S.. *Geophysical Research Letters*, *43*(1), 144-153. https://doi.org/10.1002/2016JB012887.

Prodehl, C. (1970) Seismic refraction study of crustal structure in the western United States. *Geological Society of America Bulletin*, *81*(9), 2629-2646. http://dx.doi.org/10.1130/0016-7606(1970)81[2629:SRSOCS]2.0.CO;2.

Prodehl, C., & Lipman, P. W. (1989). Crustal structure of the Rocky Mountain region. Geological Society of America Memoirs, 172, 249-284. https://doi.org/10.1130/MEM172-p249

Rudnick, R. L., & D. M. Fountain (1995). Nature and composition of the continental crust: a lower crustal perspective. *Reviews of Geophysics*, *33*(3), 267-309. https://doi.org/10.1029/95RG01302.

Rudnick, R. L., & S. Gao (2003). The composition of the continental crust. In R. L. Rudnick (Ed.) *The Crust*, pp. 1–64, Elsevier-Pergamon, Oxford, U. K.. https://doi.org/10.1016/B0-08-043751-6/03016-4

Schmandt, B., & E. Humphreys (2011). Seismically imaged relict slab from the 55 Ma Siletzia accretion to the northwest United States. *Geology*, *39*(2), 175-178. https://doi.org/10.1130/G31558.1.

Schmandt, B., F. C. Lin, & K. E. Karlstrom (2015). Distinct crustal isostasy trends east and west of the Rocky Mountain Front. *Geophysical Research Letters*, *42*(23), 10290-10298. https://doi.org/10.1002/2015GL066593.

Schulte-Pelkum, V., & K. H. Mahan (2014). A method for mapping crustal deformation and anisotropy with receiver functions and first results from USArray. *Earth and Planetary Science Letters*, *402*, 221-233. https://doi.org/10.1016/j.epsl.2014.01.050.

Schutt, D. L., A. R. Lowry, & J. S. Buehler (2016). Moho temperature and compositional controls on lithospheric bending strength in the western United States. Abstr. #T23E-03, AGU Fall Meeting, San Francisco CA.

Schutt, D. L., A. R. Lowry, & J. S. Buehler (2017). Moho temperature and mobile lower crust in the western United States. *Geology*, accepted for publication.

Shen, W., & M. H. Ritzwoller (2016). Crustal and uppermost mantle structure beneath the United States. *Journal of Geophysical Research*, *121*(6), 4306-4342. https://doi.org/10.1002/2016JB012887.

Smith, L., & D. S. Chapman (1983). On the thermal effects of groundwater flow: 1. Regional scale systems. *Journal of Geophysical Research, 88*(B1), 593-608. https://doi.org/10.1029/JB088iB01p00593.

Smith, R. B., W. C. Nagy, K. A. S. Julander, J. J. Viveiros, C. A. Barker, & D. G. Gants (1989). Geophysical and tectonic framework of the eastern Basin and Range-Colorado Plateau-Rocky Mountain transition. *Geological Society of America Memoirs*, *172*, 205-234. https://doi.org/10.1130/MEM172-p205.

Sobolev, S. V., & A. Y. Babeyko (1994). Modeling of mineralogical composition, density and elastic wave velocities in anhydrous magmatic rocks. *Surveys of Geophysics*, *15*(5), 515-544. https://doi.org/10.1007/BF00690173

Solano, J. M. S., M. D. Jackson, R. S. J. Sparks, J. D. Blundy, & C. Annen (2012). Melt segregation in deep crustal hot zones: a mechanism for chemical

differentiation, crustal assimilation and the formation of evolved magmas. *Journal of Petrology*, *53*(10). https://doi.org/10.1093/petrology/egs041.

Steck, L. K., M. L. Begnaud, S. Phillips, & R. Stead (2011). Tomography of crustal P and S travel times across the western United States. *Journal of Geophysical Research*, *116*(B11). https://doi.org/10.1111/j.1365-246X.2009.04109.x.

Taylor, S. R. (1989). Geophysical framework of the Appalachians and adjacent Grenville Province. *Geological Society of America Memoirs*, *172*, 317-348. https://doi.org/10.1130/MEM172-p317.

Tenzer, R., P. Novák, V. Gladkikh, & P. Vajda (2012). Global crust-mantle density contrast estimated from EGM2008, DTM2008, CRUST2.0, and ICE-5G. *Pure and Applied Geophysics*, *169*(9), 1663-1678. https://doi.org/10.1007/s00024-011-0410-3.

Trabant, C., A. R. Hutko, M. Bahavar, R. Karstens, T. Ahern, & R. Aster (2012). Data Products at the IRIS DMC: Stepping Stones for Research and Other Applications. *Seismological Research Letters*, *83*(5), 846–854, https://doi.org/10.1785/0220120032.

Wagner, L. S., M. J. Fouch, D. E. James, & S. Hanson‐Hedgecock (2012). Crust and upper mantle structure beneath the Pacific Northwest from joint inversions of

ambient noise and earthquake data. *Geochemistry, Geophysics, Geosystems*, *13*(12). https://doi.org/10.1029/2012GC004353.

Weber, M. B., J. Tarney, P. D. Kempton, & R. W. Kent (2002). Crustal make-up of the northern Andes: evidence based on deep crustal xenolith suites, Mercaderes, SW Colombia. *Tectonophysics*, *345*(1), 49-82. https://doi.org/10.1016/S0040-1951(01)00206-2.

White, R. W., Powell, R., & Holland, T. J. B. (2001). Calculation of partial melting equilibria in the system Na2O–CaO–K2O–FeO–MgO–Al2O3–SiO2–H2O (NCKFMASH). *Journal of metamorphic Geology, 19*(2), 139-153. https://doi.org/10.1046/j.0263-4929.2000.00303.x

Whitmeyer, S. J., & K. E. Karlstrom (2007). Tectonic model for the Proterozoic growth of North America. *Geosphere*, *3*(4), 220-259. https://doi.org/10.1130/GES00055.1

Williams, M.L., K.M. Fischer, J.T. Freymueller, B. Tikoff, A.M. Tréhu, et al., (2010). *Unlocking the Secrets of the North American Continent: An EarthScope Science Plan for 2010-2020*. 78 pp.

Zandt, G., S. C. Myers, & T. C. Wallace (1995). Crust and mantle structure across the Basin and Range-Colorado Plateau boundary at 37 N latitude and implications for Cenozoic extensional mechanism. *Journal of Geophysical Research*, *100*(B6), 10529-10548. https://doi.org/10.1029/94JB03063

Zhu, L., & H. Kanamori (2000). Moho depth variation in southern California from teleseismic receiver functions. *Journal of Geophysical Research*, *105*(B2), 2969-2980. https://doi.org/10.1029/1999JB900322

CHAPTER 3

A TWO-LAYER MODEL OF CONTINENTAL CRUST IN THE CONTERMINOUS UNITED STATES

Abstract

Detailed imaging of crustal structure and composition can improve our understanding of dynamical processes including lithospheric strength and deformation history. Although many studies of crustal seismic velocity structure have been published using EarthScope data, deep crustal properties remain ambiguous owing to incomplete constraint of the physical state of the lower crust. Here we model thicknesses and seismic velocity ratios, v_P/v_S, of two-layer crustal structure in the conterminous United Stated from joint inversion of cross-correlations of synthetic and observed seismic receiver functions, gravity, and spatial statistics. Upper and lower crustal thicknesses are consistent with imaging by active-source crustal-scale seismic refraction surveys. We observe interesting relationships of crustal structure to the history of accretion of North American terranes and the history of continental deformation. Variations in mineralogy implicit in v_P/v_S suggest the upper crust is relatively homogeneous outside of a few locations where effusive basaltic volcanism has recently occurred, including the Snake River Plain and Columbia Plateau. Averaged v_P/v_S of the lower crust in the midcontinent and eastern U.S. is significantly higher than for the upper crust, which suggests the mid-crustal boundary may represent a change in bulk chemistry. The v_P/v_S of the lower crust is

much lower under the western U.S. Cordillera than in the stable continent. Based on thermodynamical modeling of crustal mineralogy, we hypothesize that this reflects hydration of the lower crust in the deforming backarc of Farallon-Juan de Fuca subduction. This is consistent with lower density and consumption of garnet in the Cordilleran lower crust inferred from xenoliths.

3.1 Introduction

The structure and composition of continental crust provides a critical constraint on our understanding of the evolution of continental lithosphere and dynamics including mantle flow; lithospheric buoyancy; thermal, mass and volatile flux through the lithosphere; and surface deformation. Continental crust is thought to have an andesitic to dacitic major-element chemistry (Rudnick & Gao, 2003), but the variability of continental crustal composition is poorly known, particularly in the sparsely sampled deep crust. Crustal structure and chemistry are key contributors to lithosphere strength and buoyancy, which in turn affect surface elevation and deformation (e.g., Lowry et al., 2000; Bürgmann & Dresen, 2008; Becker et al., 2014, 2015). Earlier crustal-scale seismic refraction studies suggest crystalline basement can be divided into two to three layers with distinct seismic velocities (Christensen & Mooney, 1995; Braile et al., 1989; Prodehl & Lippman, 1989). Hypotheses for formation of the lowermost, highest velocity layer include crustal delamination, settling of cumulates during crustal fractionation, relamination, and

thermodynamics of mineral formation (Rudnick, 1995; Hacker et al., 2015; Guerri et al., 2015). The controversy stems in part from uncertainties in major element chemistry of the deep crust. Uncertainties in lower crustal chemistry and mineralogy also contribute to debates over the relative importance of the lower crust and upper mantle in lithospheric strength and deformation response (Maggi et al., 2000; Watts & Burov, 2003; Bürgmann & Dresen, 2008), and complicate interpretation of surface geology (Tikoff & Maxson, 2001).

Many high-resolution images of crustal seismic velocity structure have been published from the data collected by EarthScope's USArray (e.g., Lin et al., 2012; Levander & Miller, 2012; Schulte-Pelkum & Mahan, 2014; Schmandt et al., 2015; Shen & Ritzwoller, 2016; Ma & Lowry, 2017). Seismic velocity structure used to infer crustal mineralogy is derived from older active-source profiles (Rudnick & Gao, 2003; Christensen & Mooney, 1995; Kern et al., 1996; Musacchio et al., 1997; Hacker et al., 2015), coupled with xenolith samples and exhumed crustal sections (Rudnick & Gao, 2003). Lower crustal xenoliths sample sparsely and may lose much of the information relating to physical state in transit to the surface, while ambiguities in the relationships of seismic velocity to major-element composition and temperature-, pressure- and volatile-dependent equations of state obscure the composition and physical state of the deep crust (Hacker et al., 2015). The ratio of compressional to shear seismic velocities is an underutilized source of information that is insensitive to the temperature but is particularly sensitive to quartz abundance (Christensen, 1996; Lowry & Pérez-Gussinyé, 2011; Ma & Lowry, 2017). Here we

model thickness and seismic velocity ratio, v_P/v_S, of a two-layer crust for the conterminous United States in order to better illuminate mineralogical properties of the lower crust. The model jointly inverts for thickness and v_P/v_S using seismic receiver functions, gravity and a thermal model derived from Pn tomography of the uppermost mantle, following previous work by Ma & Lowry (2017). That earlier analysis inverted for properties of a single-layer crust and noted based on thermodynamical modeling of mineralogy that low v_P/v_S can be interpreted as evidence of past hydration of the crust.

The EarthScope Major Research Facilities and Equipment project was designed to understand the evolution and modern deformation processes of the North American lithosphere, as well as dynamics of the deeper mantle. EarthScope seismic and GPS instrumentation was installed beginning in 2004, and the USArray seismic network included a permanent array of 100 stations along with temporary deployments of 400 three-component broadband seismographs, called the Transportable Array (TA), at a regular ~70 km spacing initiating at the Pacific coast and rolling eastward all the way to the Atlantic coast. The TA has now completed data collection in the lower 48 United States and is currently deployed in Alaska.

3.2 Seismic Velocity Ratio, v_P/v_S

Our inversion for a two-layer crustal structure is an extension of earlier modeling of thickness and averaged v_P/v_S of a single-layer crust (Ma & Lowry,

2017). The v_P/v_S is sensitive to quartz content and is much less sensitive to effects of temperature (Christensen, 1996; Lowry & Pérez-Gussinyé, 2011; Ma & Lowry, 2017) (Figure 19), enabling us to characterize variations in mineralogy of the deep crust in isolation from other effects that make interpretation of seismic velocity ambiguous. Generally speaking, lower v_P/v_S (< 1.75), intermediate v_P/v_S (1.75-1.8) and high v_P/v_S (>1.809) represent felsic, intermediate and mafic lower crust, respectively (Holbrook, et al*.,* 1992).

Guerri et al. (2015) examined the influence of major element chemistry and hydration state on density and seismic velocities of crustal assemblages via thermodynamical modeling of mineral equations of state. They inferred that a phase change from plagioclase to clinopyroxene is partly responsible for velocity layering of the crust, and that hydration increases the seismic impedance contrast at this phase transition. Hydration also lowers the melting temperature of rocks, and significantly reduces the ductile rheological strength (Kohlstedt, 2006). Noting a corollary observation by Guerri et al. (2015) that hydration lowers v_P/v_S, Ma & Lowry (2017) replicated their thermodynamical modeling to find that hydration increases quartz abundance and reduces averaged crustal v_P/v_S, implying that low v_P/v_S is an indicator of past hydration of the crust. By modeling the thicknesses and v_P/v_S of a two-layer crustal structure, we here examine the implications of v_P/v_S for hydration state of the lower crust in the conterminous United States.

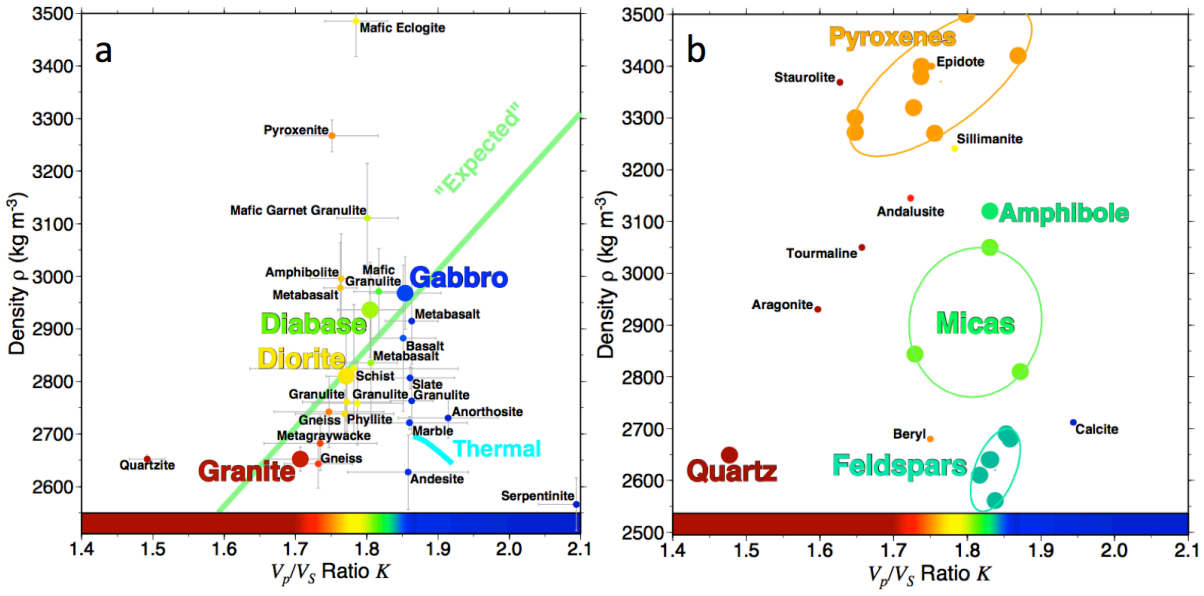

Figure 19: v_P/v_S and density of common crustal rocks and minerals (after Lowry & Pérez-Gussinyé, 2011). (a) Rock density versus v_P/v_S for various rock types; the temperature dependence of v_P/v_S in anorthite is shown as a cyan curve for a 900°C temperature range after Kono et al. (2008). (b) v_P/v_S variation in rocks is dominated by quartz content.

3.3 Data

We jointly invert the crustal structure from observations that include seismic receiver functions, gravity, and a temperature model derived from Pn-tomography of velocities of the uppermost few km of the mantle. Receiver functions used in our analysis are from the EarthScope Automated Receiver Survey (EARS) community product (Crotwell & Owens, 2005; IRIS DMC, 2010; Trabant et al., 2012), with station locations shown in Figure 20. We used EARS receiver functions only for

those seismic events with a radial match for the iterative deconvolution (Ligorría & Ammon, 1999) exceeding 80%. The seismic stations used here include those from USArray (including Transportable Array), several FlexArray and PASSCAL temporary deployments, and permanent sites from the regional networks. These were compared to synthetic receiver functions calculated via shareware codes (Ammon, 1991). Bouguer gravity data are from the WGM2012 International Gravimetric Bureau global map (Balmino et al., 2011; Bonvalot et al., 2012), which merges ground-based measurements with GRACE and GOCE satellite observations.

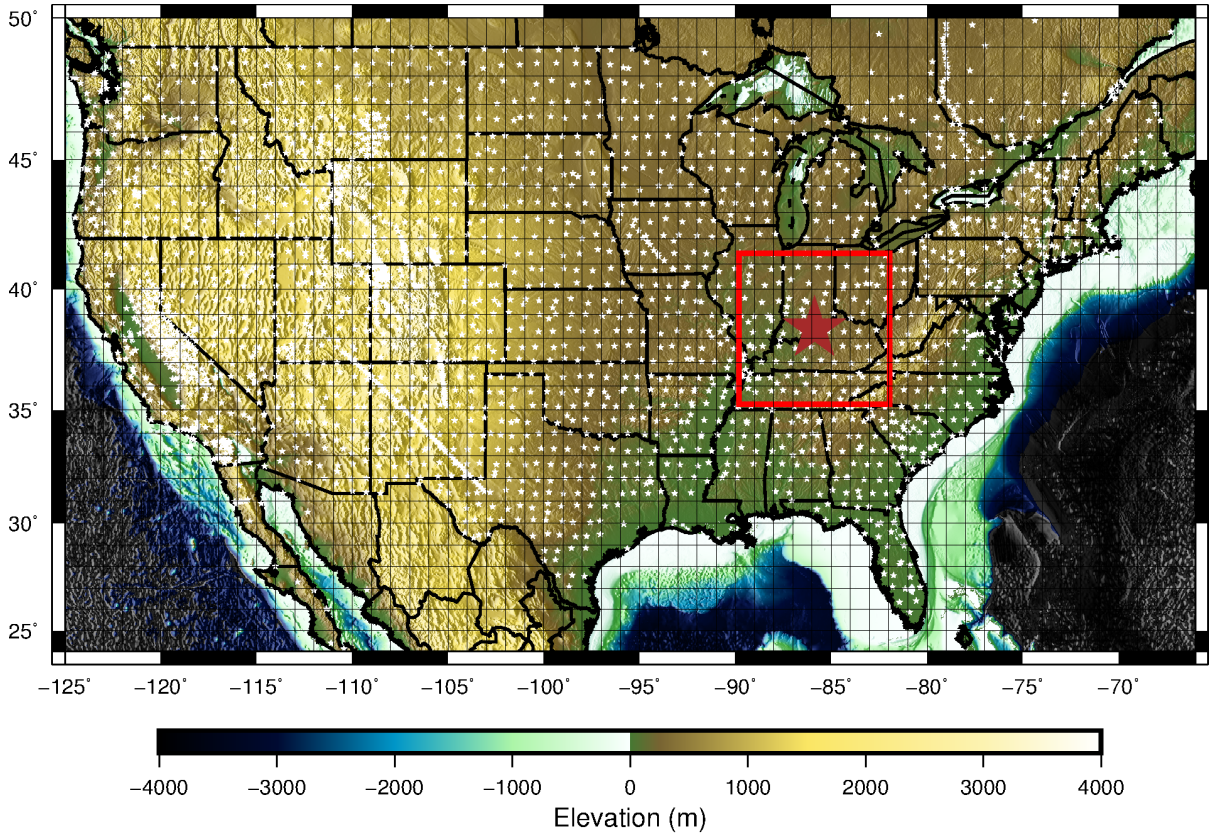

Figure 20: Seismic stations used in two-layer modeling. Color contours are topographic elevation. All seismic stations in the EARS receiver function database (Crotwell & Owens, 2005; IRIS DMC, 2010; Trabant et al., 2012) were included in the analysis, including regional networks and PASSCAL and FLEXArray deployments. The total seismic stations are close 3000 with average 46 events for each station. Red star is the location of seismic station TA.R48A used as an example in subsequent figures. Stochastic inversion for density parameters uses gravity and seismic fields from the entire United States; subgrids used to estimate gravity likelihoods are exemplified by the red box centered around the star at TA.R48A.

3.4 Methods

The two-layer model of continental crust in the United States extends an earlier analysis of single-layer crustal thickness and bulk v_P/v_S (Ma & Lowry, 2017). The workflow for calculating synthetic models, cross-correlation of the synthetic and observed receiver functions, stacking the correlation coefficients in parameter space and multiplying the cross-correlation stacks by likelihood functions in order to jointly invert with gravity and spatial statistics is similar to previous analyses (Lowry & Pérez-Gussinyé, 2011; Ma & Lowry, 2017). A significant difference is that modeling of the two-layer structure requires four model parameters, including thickness and v_P/v_S of both the upper and lower crustal layers. Building cross-correlation stacks and likelihood functions that densely sample a fully four-dimensional parameter space would require evaluating several million forward models at each site, and in the case of gravity modeling this would not be computationally tractable to do at the more than 3000 seismic stations used in our study (Figure 20). Instead, we assume that the thickness and averaged bulk v_P/v_S derived from single-layer modeling is representative for the whole crust, and invert only for thickness and v_P/v_S of the upper crustal layer, recognizing that properties of the lower layer are not independent given a fixed total thickness and bulk-crustal v_P/v_S. Thickness H_{lo} of the lower crust is simply the difference between the total, H, and upper-crustal, H_{up}, thicknesses:

$$H_{lo} = H - H_{up} \quad (3.1)$$

while the lower crustal seismic velocity ratio, κ_{lo}, can be calculated by noting that total crustal travel-times for body waves sum the travel-times in the individual layers (Figure 21). After some algebraic manipulation, this yields:

$$\kappa_{lo} = \left[\frac{\kappa\left(H_{up}V_{Plo} + H_{lo}V_{Pup}\right) - H_{up}V_{Plo}\kappa_{up}}{H_{lo}V_{Pup}} \right] \qquad (3.2)$$

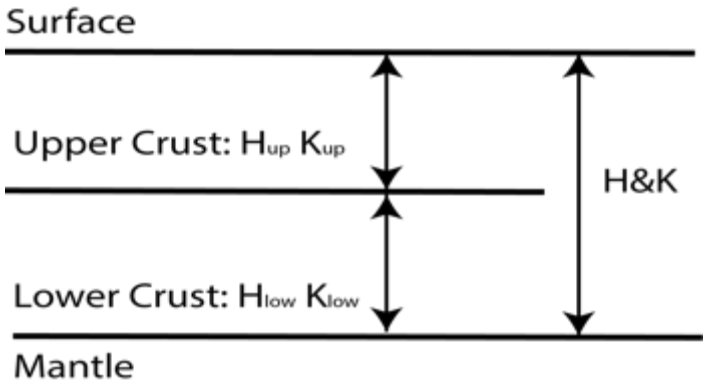

Figure 21: Simple illustration of the relationships of upper and lower crustal properties to the whole crust. The two-layer model (left) has thicknesses that sum to equal total thickness of the single-layer crust (right). The sum of travel-times through the upper and lower layers equals travel-time through the single-layer crust.

Equations (3.1) and (3.2) are also applied in the stochastic inversion of density parameters from gravity data, and in calculating the gravity likelihood functions.

3.5. Synthetic Receiver Functions and Parameter-Space Cross-Correlation Stacking

Typically, parameter-space stacking approaches to receiver function imaging of the crust stack the amplitudes of receiver functions at times predicted for the arrival of the Ps, PpPs and PpSs+PsPs phases following the P arrival (Zhu & Kanamori, 2000). Our approach differs in that we instead cross-correlate observed with synthetic receiver functions and stack the correlation coefficients in thickness versus v_P/v_S parameter space (Ma & Lowry, 2017). At each seismic site, synthetic receiver function models (Ammon, 1991) were generated with total crustal thickness and bulk v_P/v_S fixed to the estimates derived from our single-layer analysis (Ma & Lowry, 2017), upper crustal thickness are allowed to vary over a range from 10 km to 60 km with 0.25 km step, and upper crustal v_P/v_S varies from 1.6 to 2.1 with 0.025 step. This resulted in a total of more than twelve million synthetic models (4000 models times more than 3000 stations).

Continental crustal structure from active source refraction profiling typically is divided into two or three layers including a high-velocity lower crust. P-wave velocities vary from 6.0 to 6.2 km/s for the crystalline upper crust, 6.3 to 6.8 km/s for the midcrust and can exceed 7.0 km/s in the lower crust (Laske et al., 2013; Smith et al., 1989; Pakiser, 1989; Braile et al., 1989; Dziewonski & Anderson, 1981). Our studies model a single midcrustal boundary separating upper and lower crust, so our refraction synthetic models assumed P wave velocities of 6.2 km/s for the upper crust, 6.8 km/s for the lower crust and 8 km/s for the upper mantle. Errors in assumed v_P have been shown to have very small impacts on amplitude-stacking

estimates of v_P/v_S that rely primarily on travel-times (Zhu & Kanamori, 2000), but assumed velocities significantly affect amplitudes in synthetic receiver functions. However, the cross-correlation approach adopted here is somewhat insensitive to amplitudes. The synthetic receiver function model (Ammon, 1991) specifies a white-noise level, *C*, to prevent numerical singularity of the deconvolution. We tested values for *C* ranging from 0.1 to 0.00001 and settled on 0.00001 as the most robust. A Gaussian filter with width a = 2.5 s was assumed, matching that used by EARS to generate the observed receiver functions. All observed receiver functions were resampled to 20 Hz, the sample rate of the synthetic receiver function. An example ensemble of observed receiver functions and the synthetic model that best fit them is given in Figure 22.

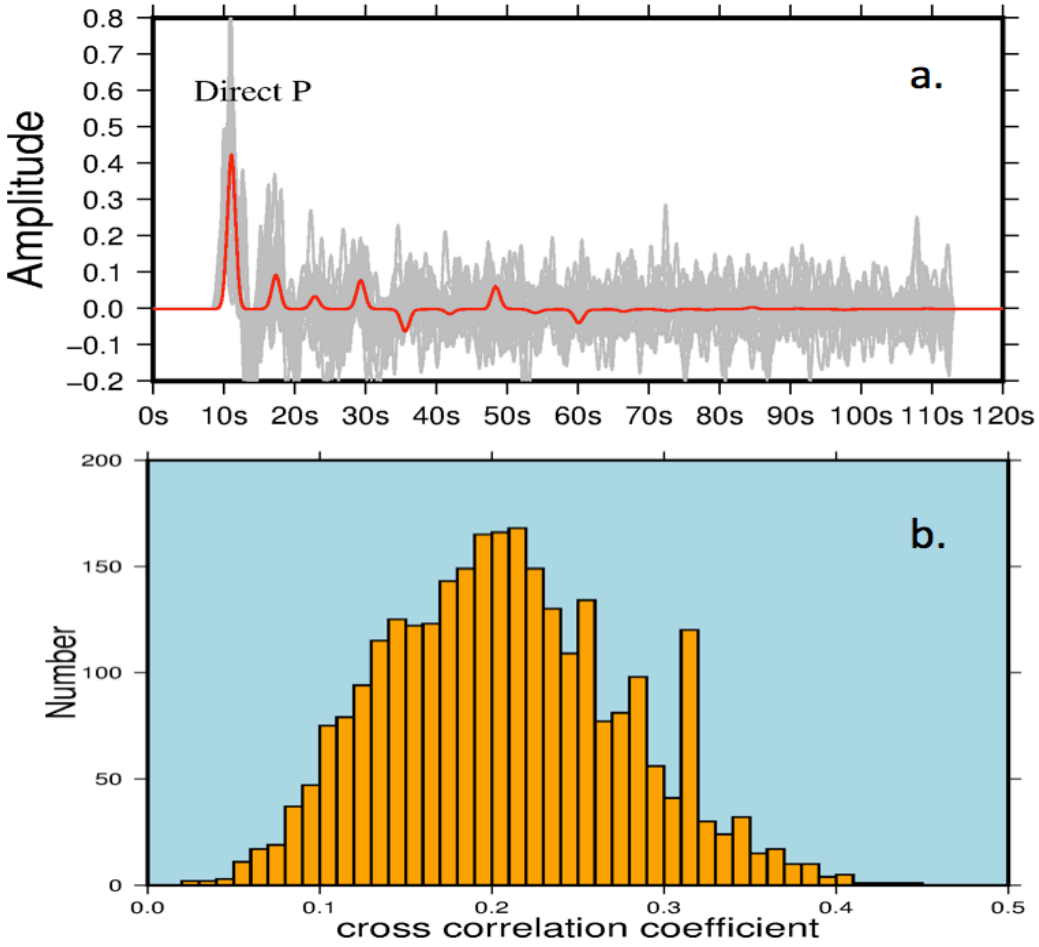

Figure 22: Cross-correlation of observed and synthetic receiver functions. (a) Example of observed (grey curves) and highest cross-correlation synthetic modeled (red curve) receiver functions for a two-layer crustal model at site TA.M25A. The direct P arrival (within the blue rectangle) is masked. (b) Histogram of maximum averaged cross-correlation coefficients of all seismic stations.

Before calculating the cross-correlation, the observed and synthetic receiver functions were aligned to impose coincident timing of the direct *P* arrival, after which

the direct P arrival in each was masked so that only the later phase arrivals are included in the cross correlation calculation (Figure 22). We average the cross-correlation coefficients for all earthquake events as a function of the upper crustal thickness (H_{up}) and seismic velocity ratio (κ_{up}) assumed in the synthetic model, analogous to the H-κ parameter-space representation used in amplitude stacking of single-layer crustal models (Zhu & Kanamori, 2000; Ma & Lowry, 2017). Like with our single-layer crustal model, the averaged cross-correlations exhibit several local maxima as a function of (H_{up}, κ_{up}) (Figure 23). The largest average cross-correlation coefficients are low, with median maxima around 0.22 (Figure 22), but larger than the averaged cross-correlations for a single-layer model (typically ~0.14). For example, the maximum averaged cross-correlation coefficient at station TA.R48A is only 0.30 at H = 16 km and v_P/v_S = 1.63 (Figure 23), which is significantly greater than the 0.14 maximum cross correlation from single-layer crustal modeling at this site. A secondary maximum occurs at H = 18 km, v_P/v_S = 2.10, and a tertiary maximum occurs at a crustal thickness of 38 km and v_P/v_S of 1.6 (which reflects the conversion at the Moho). Multiple maxima occur because our modeling assumes just two impedance boundaries separating layers of uniform thickness and velocity, whereas the real-Earth crust is more complicated. Converted phases are generated at all impedance contrasts in the crust, and both crustal thickness and v_P/v_S can vary on scales sampled by the conversions and reverberations from different azimuths of earthquake events at a single site.

Relative to single-layer crustal modeling, two-layer models improve in several ways. First, the maximum averaged cross-correlation coefficients are significantly increased. The median maximum cross-correlation coefficient for two-layer models is 0.22 (Figure 22) whereas for single-layer models the median is 0.14 (Figure 7), and similar-sized improvements occur at each individual station. Second, the number of significant local maxima is reduced. This is encouraging both because mid-crustal impedance contrasts should be responsible for some of the local maxima in single-layer modeling, and because the higher correlation coefficients associated with a more robust model should improve the robustness of modeling.

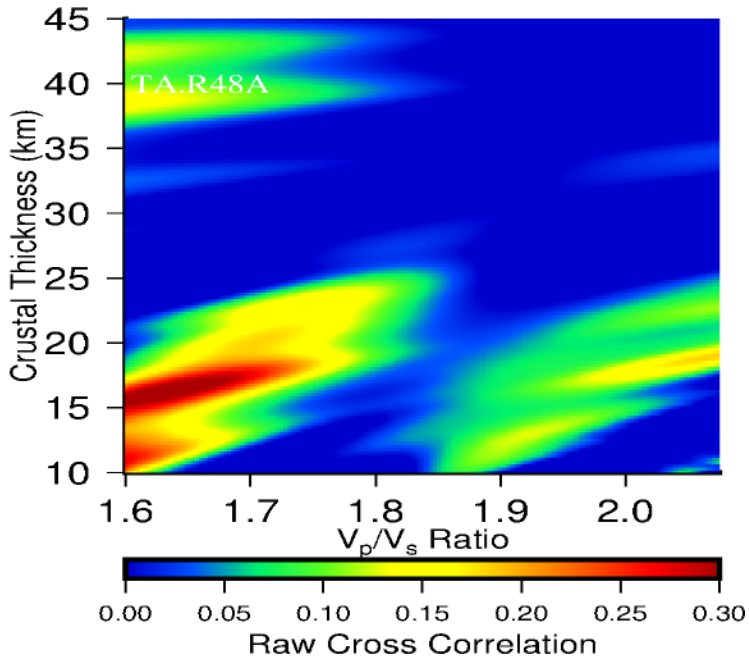

Figure 23**:** Example parameter-space average of cross-correlation coefficients relating observed and modeled receiver functions for a two-layer crustal model at station TA.R48A. The highest cross-correlation implies a mid-crustal impedance contrast at H = 16 km and v_P/v_S = 1.65. A secondary cross-correlation peak at H = 39 km indicates mismodeling of a portion of the seismic energy converted at the Moho depth.

3.6 Gravity Modeling and Density Parameters

The thickness and v_P/v_S of the upper and lower crust under each seismic station were further constrained by modeling of Bouguer gravity and examination of the spatial statistics of estimates at neighboring seismic stations. Variations in layer thicknesses, compositional differences associated with variations in bulk v_P/v_S, and

geothermal variations each contribute to gravity. The seismically-derived model parameters can be related to gravity by assigning corresponding density parameters, including $\Delta\rho_{Moho}$ for the mean density contrast at the Moho, $\partial\rho/\partial\kappa$ for density variation associated with v_P/v_S, and a coefficient of thermal expansion, α_v. We note here that we do not assign an independent density contrast to the midcrustal boundary because, as we will show, there is a significant change in v_P/v_S at the mid-crustal boundary that captures the density change there. Calculation of Bouguer gravity anomalies, *B*, associated with crustal thickness is identical to the approach described previously (Lowry & Pérez-Gussinyé, 2011*;* Ma & Lowry*,* 2017):

$$\widetilde{B}_H = 2\pi G\Delta\rho_{Moho}\widetilde{H}\exp(-k\overline{H}) \qquad (3.3)$$

where the overbar indicates a mean value, the tilde ~ denotes 2D Fourier-transformed amplitudes of a field with the mean removed (e.g., $\tilde{H} = F\left\{H\left(x,y\right)-\bar{H}\right\}$ where $F\{\bullet\}$ denotes the Fourier transform operator), k is the modulus of 2D wavenumber associated with each amplitude, and G is the universal gravitational constant.

The calculation of Bouguer anomalies associated with v_P/v_S variation differs from previous analyses however because there are now two crustal layers with potentially differing v_P/v_S, yielding:

$$\tilde{B}_{\kappa} = 2\pi G \frac{\partial \rho}{\partial \kappa} \begin{Bmatrix} \dfrac{1-\exp\left(-k\bar{H}_{up}\right)}{k}\tilde{\kappa}_{up} \\ +\dfrac{\exp\left(-k\bar{H}_{up}\right)-\exp\left(-k\bar{H}\right)}{k}\tilde{\kappa}_{lo} \\ -\tilde{M}\exp\left(-k\bar{H}\right)-\tilde{N}\exp\left(-k\bar{H}_{up}\right) \end{Bmatrix} \quad (3.4)$$

Here, $\tilde{M} = F\left[\left(H-\bar{H}\right)\left(\kappa-\bar{\kappa}\right)\right]$ is a correction factor for mass associated with varying crustal thickness and v_P/v_S at the Moho; $\tilde{N} = F\left[\left(H_{up}-\bar{H}_{up}\right)\left(\kappa_{up}-\kappa_{low}\right)\right]$ is a similar correction for the mass associated with variable upper crustal thickness and changing v_P/v_S at the mid-crustal boundary.

Finally, we calculate the thermal contribution to Bouguer gravity anomalies via:

$$\tilde{B}_T = \int_0^{200} 2\pi G \alpha_v \bar{\rho}(z)\tilde{T}(z)\exp(-kz)dz \quad (3.5)$$

Here temperatures $T(x,y,z)$ are derived from Pn variations and surface heat flow via the geothermal model as described in Ma & Lowry (2017). The associated density parameters were determined with a stochastic inverse method similar to that described in Ma & Lowry (2017), with the primary difference that the gravity anomalies caused by bulk v_P/v_S are calculated with two-layer model using equation 3.4, and the reference density, $\bar{\rho}(z)$, corresponds to that of a mean continental crustal composition (Christensen & Mooney, 1995).

3.7 Spatial Statistics and Optimal Interpolation

To generate gridded values of upper crustal thickness H and seismic velocity ratio κ needed for the gravity modeling, we must interpolate estimates of the seismic properties at irregularly-spaced seismic sites to a constant-spaced grid. For this we use optimal interpolation (OI), also called “kriging”, an interpolation method that relies on the spatial statistics of measured data to estimate the most likely value and uncertainty at an unsampled location (Davis, 1986). Optimal interpolation uses the variogram statistics of a field, an expression of the expected value of the difference between measurements as a function of the distance between the measurements.

Variograms of upper crustal thickness H and v_P/v_S are estimated directly from the estimates at pairs of individual seismic stations by binning according to the distance between the stations (Figure 24). Ideally, the variogram at zero distance reflects the variance of individual measurements while the variogram at large distances represents the global variance of the field. A parametric (spherical) model of the variogram estimates is used to invert for optimal weights applied to the estimates at sites surrounding an interpolation location, and the weights plus a Lagrange variable provide an estimate of the variance of the interpolation estimate. In addition to affording gridded interpolations of the seismic fields, optimal interpolation expected values and variance will be used to generate OI-likelihood functions at a seismic station location based on the estimates at nearby sites.

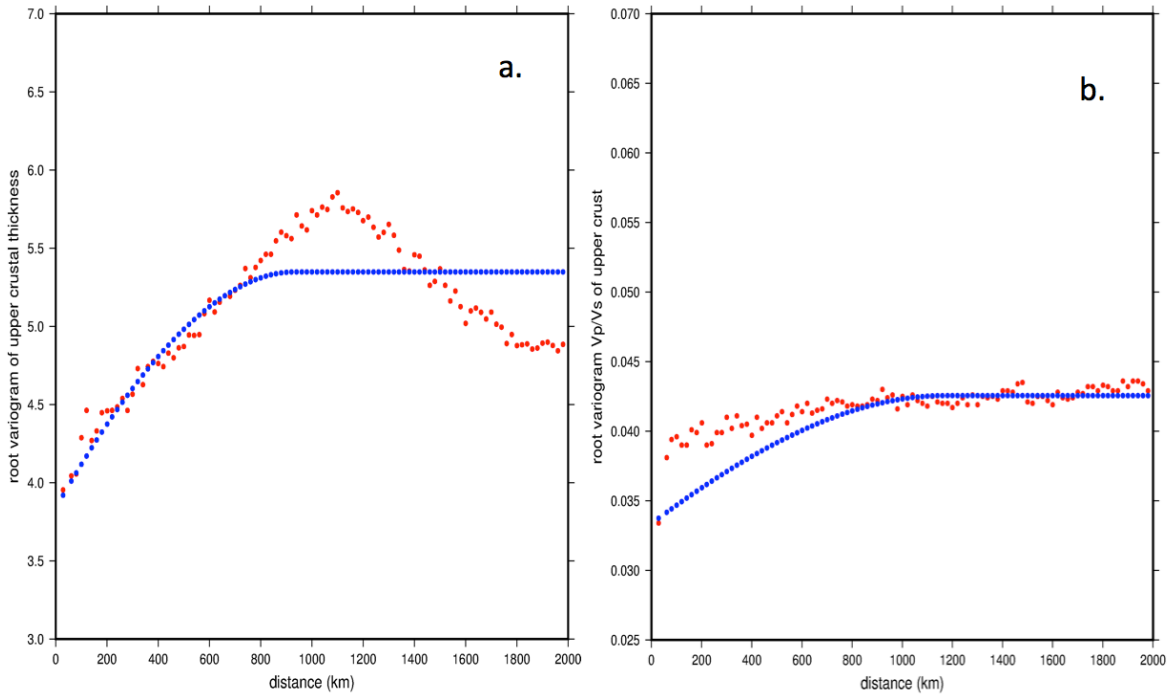

Figure 24: Root variograms of (a) thickness and (b) v_P/v_S of the upper crust. Red circles are derived from all of the raw results after binning by distance between measurements of each joint inversion; blue circles depict a spherical parametric model (approximating the observed distribution) that was used for optimal interpolation.

3.8 Joint Inversion with Gravity and OI Likelihood Filters

The joint inversion for crustal thickness and upper crustal v_P/v_S is applied iteratively over all the seismic stations in the study area (Figure 20). First, a gravity

likelihood filter is calculated using a small window centered at the station slated for update, S_i. The upper crustal thickness H_{up} and v_P/v_S κ for station S_i are treated as unknown variables, while prior estimates of H and κ at surrounding stations are temporarily held fixed. For each possible combination of $(H_{up}, \kappa_{up})_j$ in the parameter space at station S_i, we interpolate (H_{up}, κ_{up}) at S_i and the surrounding sites to a 20 km-spaced, 640×640 km grid. The grids are used to model the gravity via equations (3.3) – (3.5) using density parameters derived from stochastic inversion of the larger grid as described in section 3.7. The L_2-norm, R, of the difference between observed and modeled gravity is calculated for each assumed $(H_{up}, \kappa_{up})_j$, and contours of the misfit are used to calculate associated confidence intervals $(1 - \alpha)$ via the likelihood ratio method (Beck & Arnold, 1977):

$$R^2 \le R^2_{\min}\left(1 + \frac{M}{N-M} F_{\alpha}^{-1}\left(M, N_g - M\right)\right) \qquad (3.6)$$

Here, $R_{\min}$ is the global minimum gravity L_2 norm, M is the number of model parameters (i.e, two corresponding to H_{up} and κ_{up} at the seismic site S_i), N_g is the number of gravity observations, F^{-1} is the inverse of the F distribution function and α is probability. The likelihood of the model given the data corresponds to the probability density function described by $(1 - \alpha)$, after normalization to yield an integral over the parameter space equal to one. An example gravity likelihood function for station TA.R48A (without normalization) is given in Figure 25b.

Optimal interpolation provides estimates of both the expected values $\left(\langle H_{up}\rangle,\langle \kappa_{up}\rangle\right)$ and standard deviations $\left(\sigma_H,\sigma_\kappa\right)$ of interpolated fields. To create the OI-likelihood filter, we interpolate estimates of upper crustal thickness and v_P/v_S at the nearest 150 seismic sites to the location of seismic station S_i. The C_{OI} confidence interval of any arbitrary $(H_{up}, \kappa_{up})_j$ in the 2D parameter space (where C_{OI} represents a real-valued multiple of normalized σ) can be calculated via:

$$C_{OI}^2\left(\left(H_{up},\kappa_{up}\right)_j\right)=\left(\frac{H_{up_j}-\langle H_{up}\rangle}{\sigma_H}\right)^2+\left(\frac{\kappa_{up_j}-\langle \kappa_{up}\rangle}{\sigma_\kappa}\right)^2 \qquad (3.6)$$

which has corresponding probability density function:

$$\alpha=\frac{1}{2\pi}\exp\left(-\frac{C_{OI}^2}{2}\right) \qquad (3.7)$$

An example OI likelihood function (without the normalization constant) is shown in Figure 25a.

Finally, both likelihood functions are multiplied by the stacked cross-correlations of modeled and observed receiver functions. The upper crustal thickness and v_P/v_S at station S_i are then updated to the maximum of the likelihood-filtered cross-correlation stack (Figure 25d).

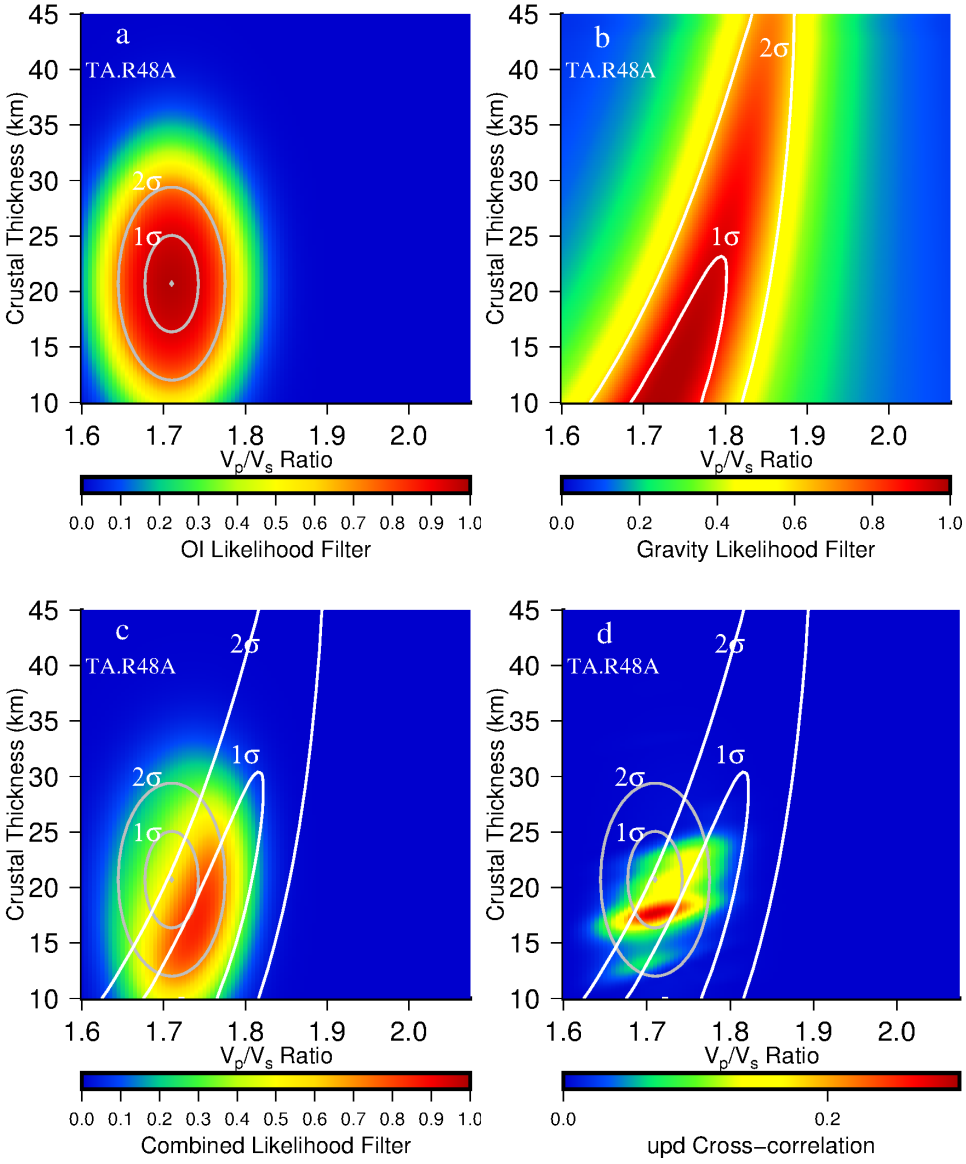

Figure 25: Example parameter space likelihood filtering for joint inversion of gravity and seismic receiver functions for the two-layer model. The example is from seismic station TA.R48A. a) Optimal Interpolation likelihood function. b) Gravity likelihood function. c) Combined likelihoods for OI and gravity. d) Updated receiver function cross-correlation stack after multiplying the likelihood filters by the cross-correlation stack (compare with the raw stack in Figure 23).

3.9 Results

We ran the joint inversion for more than fifty iterations. The final interpolated results of the two-layer model exhibits patterns reflective of surface physiographic and basement provinces, and they also further illuminate the pattern of variations observed in the single-layer crustal model of Ma & Lowry (2017). The depth of the mid-crustal boundary from our study is generally similar to results from seismic refraction/reflection survey (Christensen & Mooney, 1995; Braile et al., 1989; Prodehl & Lipman, 1989). The thickness of the upper crust, shown in Figure 26a, is 16.8 ± 3.8 km. In the western U.S. Cordillera, the upper crust is relatively thin ($\leqslant$ 15 km) in the extensional provinces and along the Pacific coastline, while the upper crust of the Sierra Nevada and Cascade ranges, Rocky Mountains and Colorado Plateau is relatively thick (18–25 km). The western side of the Interior Plains has a thick upper crust consistent with the neighboring Rocky Mountain region, but the remainder of the High Plains from North Dakota to Nebraska has predominantly thin upper crust. The upper crust is as thin as 10 km in the eastern Dakotas, where the total crust is also thin. The midcontinent upper crust is up to 20 km thick in western Texas and the Midcontinent Rift and Central Lowlands. In the east, the thinnest upper crust is in the Mississippi Embayment and Atlantic Coastal Plain. Under the Appalachian Highlands, the upper crustal thickness is up to 25 km in the Charlotte belt and ~15–20 km in the Inner Piedmont. The Grenville Front demarks a boundary between thick (25 km) upper crust to the east and thinner (15-20 km) to the west.

Zones of similar upper crustal thickness commonly cross the boundaries of Precambrian basement age terranes, but upper crust of the Mazatzal province is notably thicker than that of the Yavapai to the north and the southern Granite-Rhyolite province. Upper crustal thickness in the Cordillera and Appalachia tend to correlate more with physiographic provinces and associated tectonic history than with basement age.

The seismic velocity ratio of the upper crust (Figure 26b) is 1.71 ± 0.03. The Basin & Range, Colorado Plateau, middle Rocky Mountains, southern Rocky Mountains and Rio Grande rift all have low v_P/v_S (<1.70). The Pacific coastal oceanic-derived terranes, Columbia Plateau and Snake River plain have higher v_P/v_S up to 1.8, which is a value typical of gabbro or basalt (Geist & Richard, 1993). The northern Interior Plains and northern Texas also have high v_P/v_S, while most of the eastern U.S. has low to moderate v_P/v_S except in the northern Ohio.

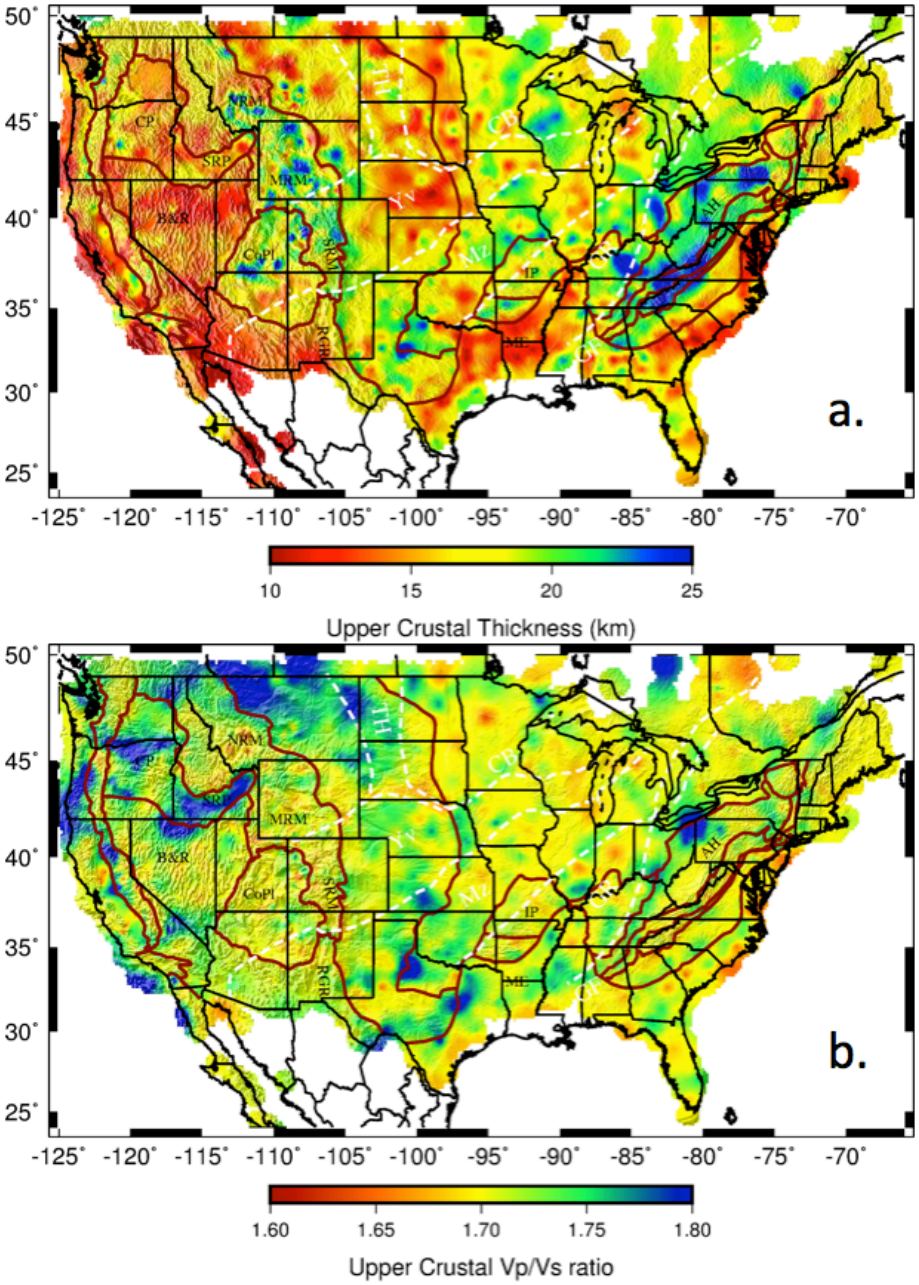

Figure 26. Upper crustal structure of the continental United States. (a): Upper crustal thickness is 16.8 ± 3.8 km. (b): seismic velocity ratio, v_P/v_S, of the upper crust is 1.71 ± 0.03. Geological province boundaries are shown in red and labeled with black text; the province acronyms are described in Figure 11.

The lower crustal thickness is 22.4 ± 4.7 km (Figure 27a), which is 33% thicker on average and 50% greater variance than the upper crustal thickness. Most of the rifted Cordilleran lower crust is thin (< 20 km) with the exception of > 20 km lower crust in the Sierra and Cascade ranges, Snake River Plain and Columbia Plateau. Under the eastern and western edges of the northern Basin & Range where the most extensional thinning has occurred, the lower crust is only 12–15 km thick. A ribbon of thicker (~20 km) lower crust runs north-south along the higher-elevation center of the Basin and Range. Thicker crust of the Rocky Mountains, Colorado Plateau and Great Plains has mostly 20–30 km thick lower crust with pockets that locally exceed 30 km. The lower crust under the adjacent Central Lowlands is generally 20–25 km except in the eastern Dakotas where total crustal thickness is anomalously thin and the lower crust is less than 20 km. The thickest lower crust in the eastern U.S. (20–30+ km) is in the southern Granite-Rhyolite province west of the Grenville Front, while the Mississippi Embayment and Atlantic Coastal Plain has lower crust only 10–15 km thick. Overall, the thickest lower crust is under the Yavapai Province, Trans-Hudson and southern Granite-Rhyolite Precambrian basement age terranes.

The seismic velocity ratio, v_P/v_S, of the lower crust is 1.88 ± 0.11 (Figure 27b). The much higher mean v_P/v_S (1.88 vs. 1.71) indicates the lower crust is much more mafic/less quartz-rich than the upper crust, which is anticipated, but the standard deviation of the variations (0.11 vs. 0.03) is also nearly four times larger. The lowest v_P/v_S (1.70–1.72) is found in the lower crust of the southern Rocky Mountains and

Rio Grande rift, which is consistent with the pattern of bulk crustal v_P/v_S. v_P/v_S under the northern Basin and Range is also low, 1.72-1.75, as are parts of the northern and middle Rocky Mountains, Columbia Plateau, the southern Great Plains, southern Illinois and South Carolina. Other regions all have relatively high v_P/v_S. The Midcontinent rift is clearly appearent as a zone of relatively high lower-crustal v_P/v_S, whereas this feature is not obviously expressed in upper crustal v_P/v_S.

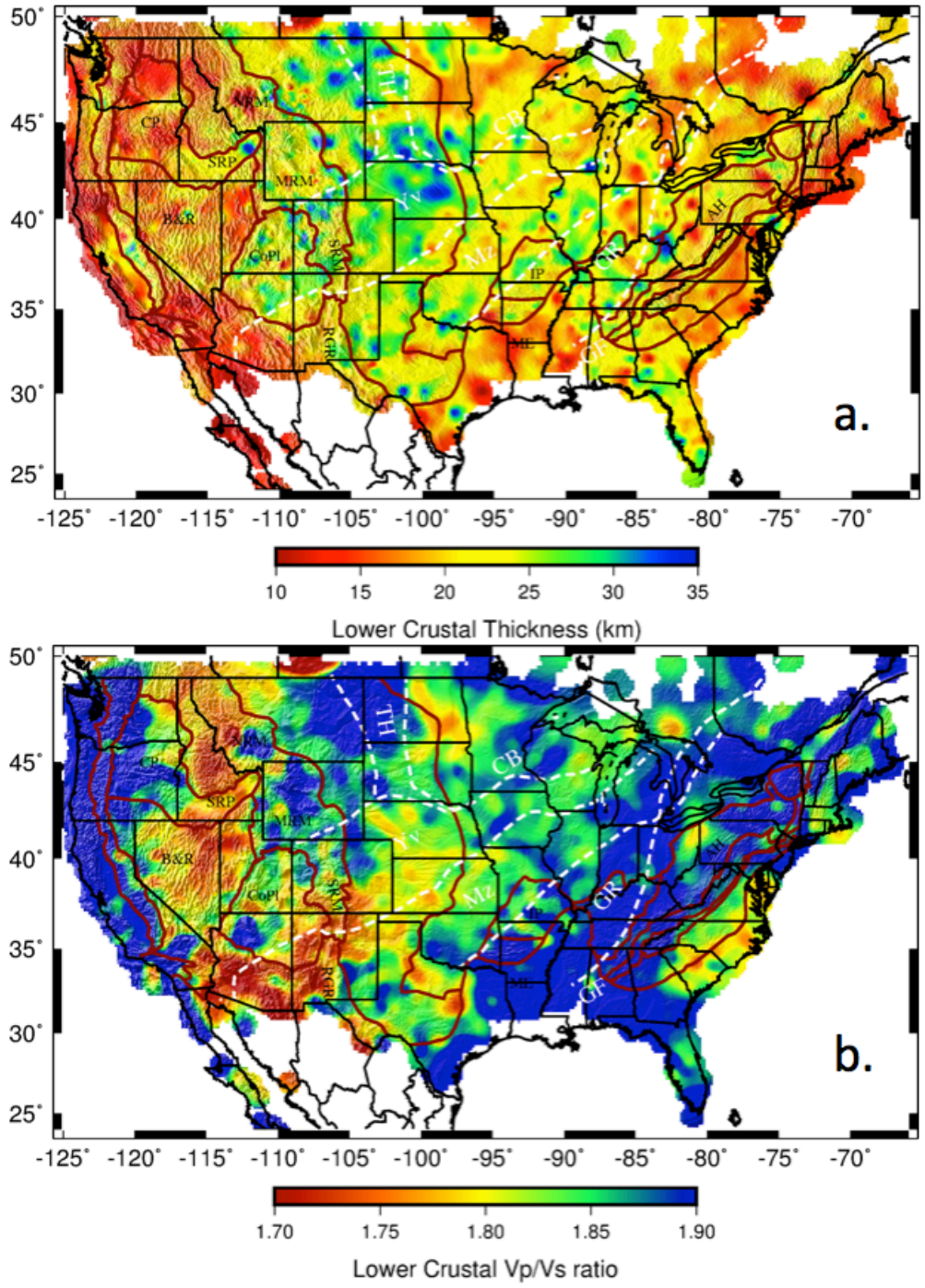

Figure 27: Thickness and v_P/v_S of the lower crust of the continental United States. Top: lower crustal thickness is 22.4 ± 4.7 km. Bottom: lower crustal seismic velocity ratio, v_P/v_S, is 1.88 ± 0.11.

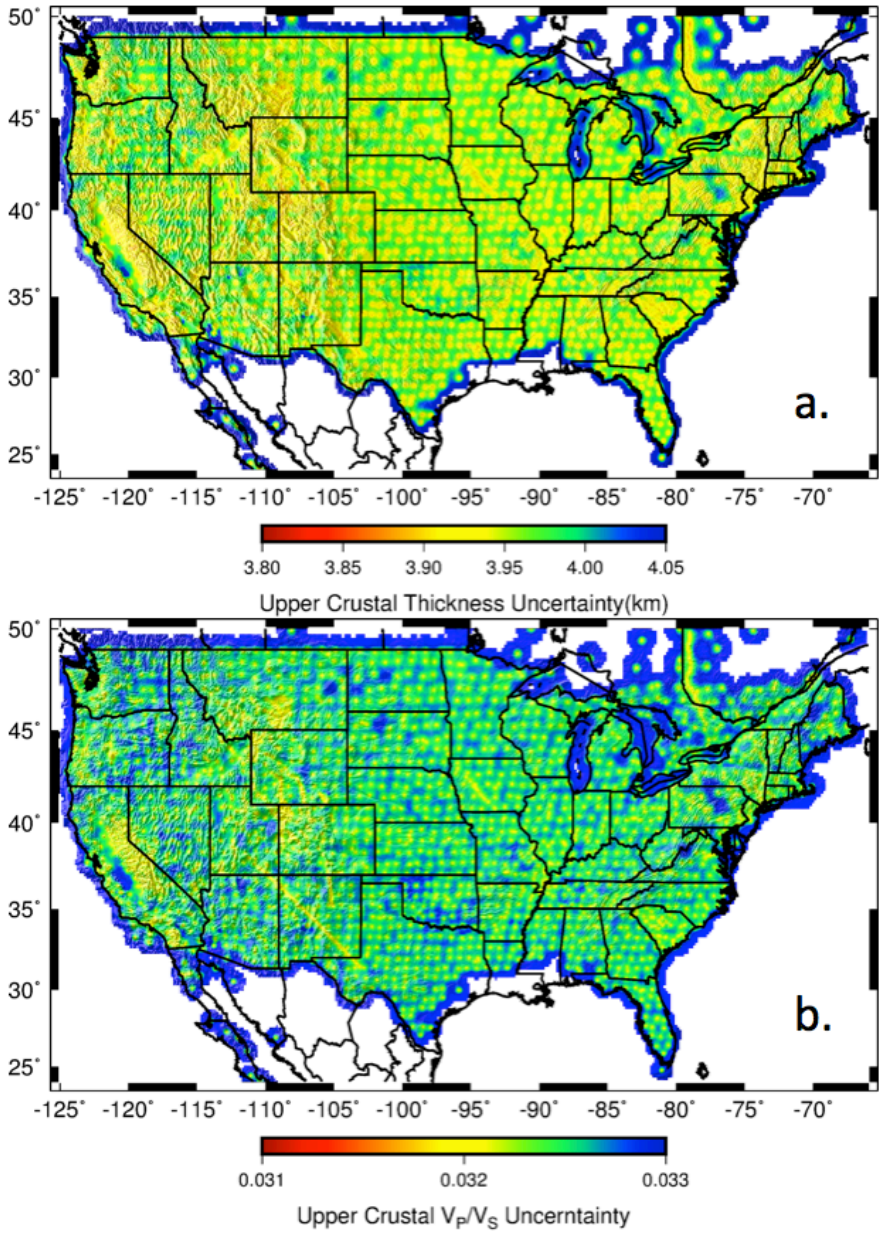

Figure 28: Uncertainty of upper crust. One-sigma uncertainty of upper crustal thickness (a) and v_P/v_S (b). Uncertainty is calculated from optimal interpolation. For upper crustal thickness, the uncertainty is 3.9 km near seismic sites and 4.05 km at distances beyond 70 km. v_P/v_S uncertainty is 0.032 near seismic sampling and rises to 0.033 beyond 70 km.

3.10. Uncertainties

Uncertainties of the gridded upper crustal thickness and v_P/v_S are shown in Figure 28. The uncertainties are derived from optimal interpolation, in which variograms of the fields (Figure 24) are used to estimate weight factors for interpolation from nearby seismic measurements, resulting in the nearest seismic sites having the greatest weight. The variance corresponds to the weighted sum of the variogram variances expected for the distance between the measurement sites and interpolation point, plus a slack variable that results from requiring interpolation weights to sum to one (e.g., Davis, 1986). Typical uncertainties are ~4.0 km for upper crustal thickness and 0.033 for v_P/v_S.

3.11. Gravity Residuals

Gravity anomalies associated with crustal structure are also estimated as part of our joint inversion. Figure 29 shows the gravity anomalies models with the final inverted density parameters of the two-layer model. The estimated Moho density contrast, $\Delta\rho_{\text{Moho}}$ = 256 kg/m^3, is very similar to that of our single-layer model. This is to be expected given that the Moho depth and averaged bulk v_P/v_S from the one-layer model are used to build the two-layer model. The estimate of the crustal compositional density parameter, $\partial\rho/\partial(v_P/v_S)$ = 1120 kg/m^3, is about 100 kg/m^3 less than that of the single-layer model (Ma & Lowry, 2017). The root-mean square (RMS) misfit of the gravity models to observed gravity are 85.3 mGal for crustal thickness, 64.8 mGal for v_P/v_S, and 56 mGal for the total model combining crustal

thickness, compositional and thermal mass variation. The rms misfit of gravity associated with v_P/v_S is decreased by about 25 mGal relative to the single-layer model. Since the contribution to gravity from compositional variation already exceeds that from crustal thickness in the single-layer model, this indicates that contributions to gravity and mass balance from compositional variations are much more significant than generally thought (Ma & Lowry, 2017). Relative to the single-layer model, the amplitude of the gravity residual is reduced in the tectonically stable Great Plains and Appalachian Highlands (Figure 30), with the largest changes attributable to v_P/v_S layering in the midcontinent.

The gravity residual after removing crustal mass should reflect mass variations in the mantle. The residual is in the range of –150 to 50 mGal in the west and 50 to 200 mGal in the east (Figure 29). Ma & Lowry (2017) inferred a 63 kg/m^3 difference in Moho density contrast for the western versus eastern U.S., as compared to a 200 kg/m^3 difference in Moho density contrast west versus east of -105°E longitude estimated by Schmandt et al. (2015). We again inverted separately for Moho density contrast east and west of the Rocky Mountain front (Figure 30) and found the best-fit Moho density contrasts differ by 111 kg/m^3. This is larger than the difference inferred from the single-layer model, but still much smaller than the estimate of Schmandt et al. (2015). If we add a 100 kg/m^3 difference in Moho density contrast expected from mean crustal v_P/v_S difference and a 12 kg/m^3 difference related to differences in uppermost mantle temperature of the western versus

eastern U.S. (Ma & Lowry, 2017), the sum is 212.8 kg/m^3, which is only slighter greater than the estimate of Schmandt et al. (2015).

Some of the gravity residual anomalies may be amplified by errors introduced if melts are present in the crust. For example, the upper crustal v_P/v_S of the northern Rocky Mountains is typical of the upper crust, but the lower crustal v_P/v_S is much lower than surrounding regions, reflecting the low observed Bouguer gravity. Wagner et al. (2012) observed that shear wave velocities in the northern Rocky Mountains decrease as much as 8% beginning at ~20 km depth (approximately the base of our upper crust). In the High Lava Plains and Northern Basin and Range, low shear velocity was observed through the entire crust where we find low v_P/v_S in both the upper and lower crust. High electric conductivity near the Moho in these regions almost certainly requires partial melt (Meqbel et al., 2014). Partial melts would increase v_P/v_S and lower crustal density, resulting in a density derivative with opposite sign to the compositional trend that dominates our estimate of the density derivative.

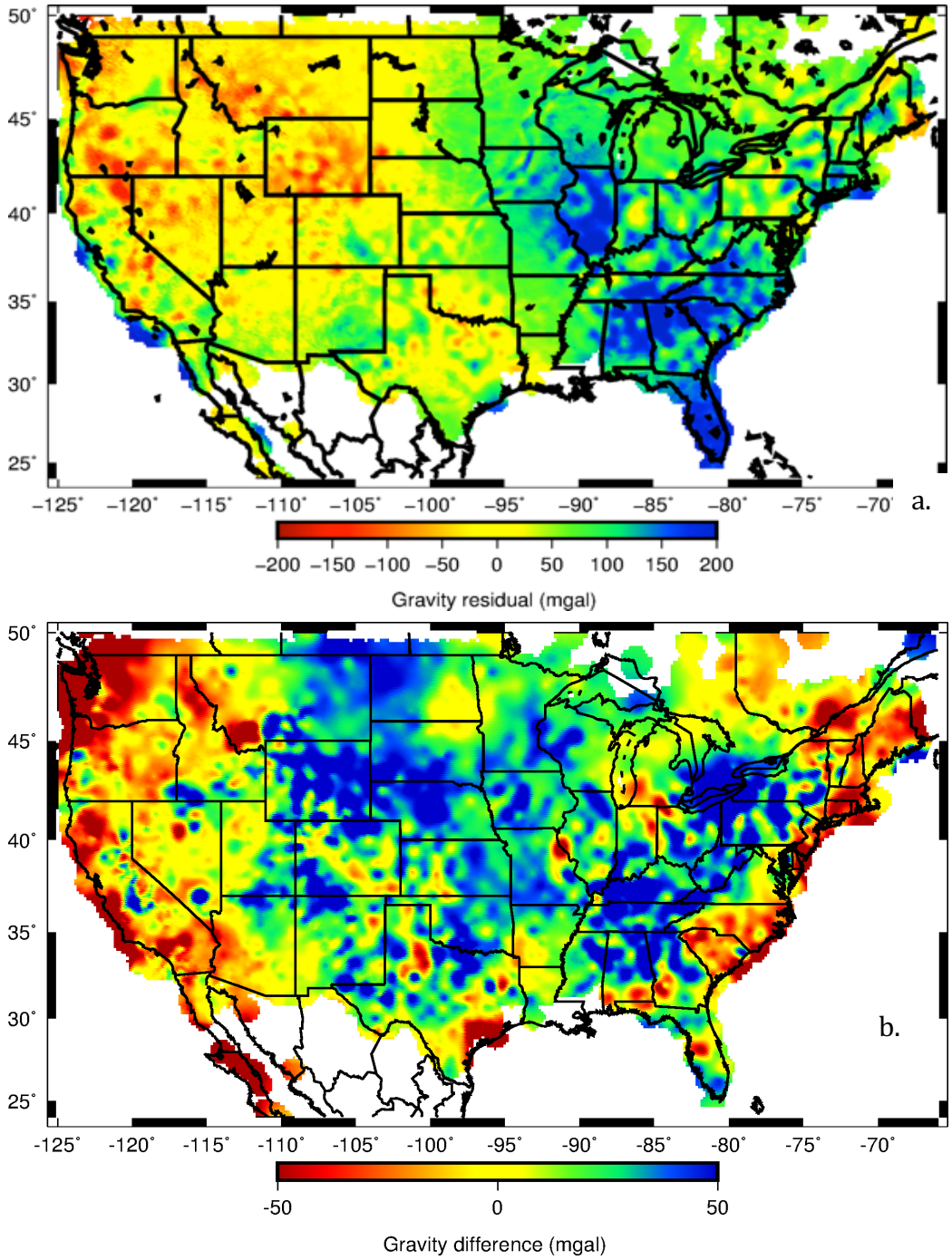

Figure 29: Gravity residuals. (a): Gravity residual after removing crustal and thermal mass of the two-layer model. (b): Difference in gravity residuals of the two-layer and single-layer models (two-layer residual minus one-layer residual).

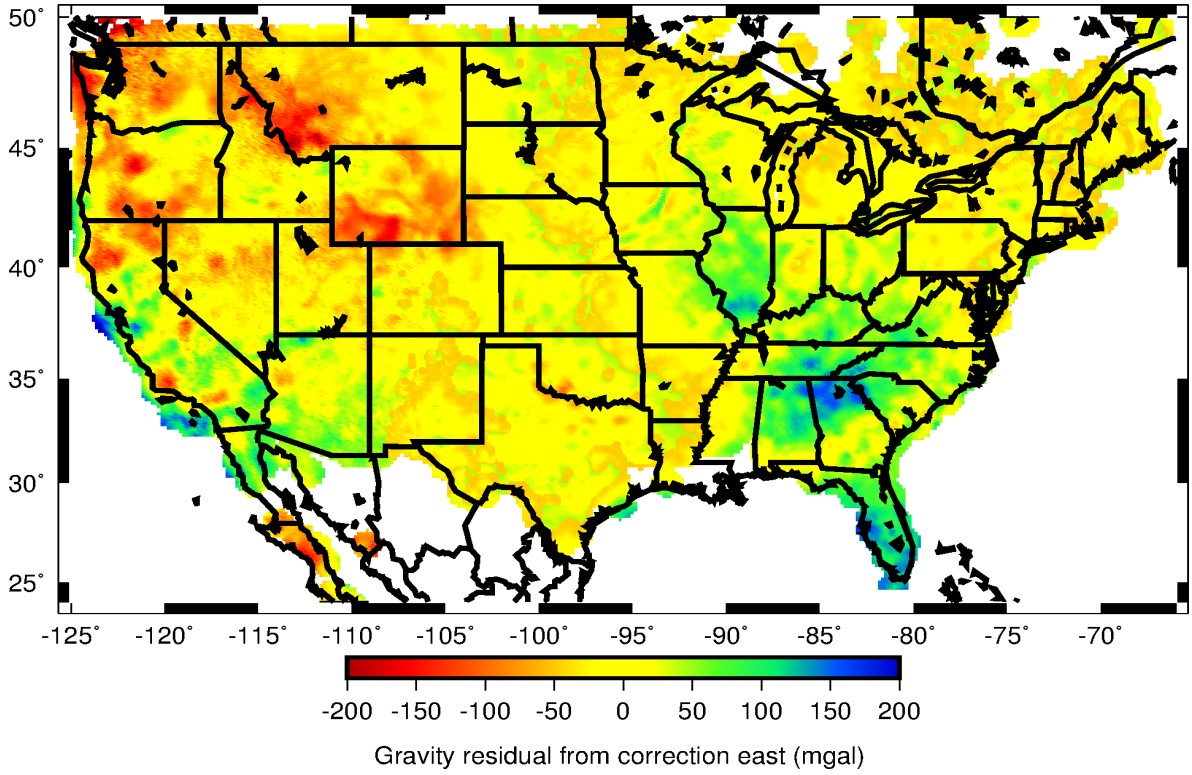

Figure 30: Residual gravity after separately solving for two different Moho density contrasts for regions east and west of –105°E longitude.

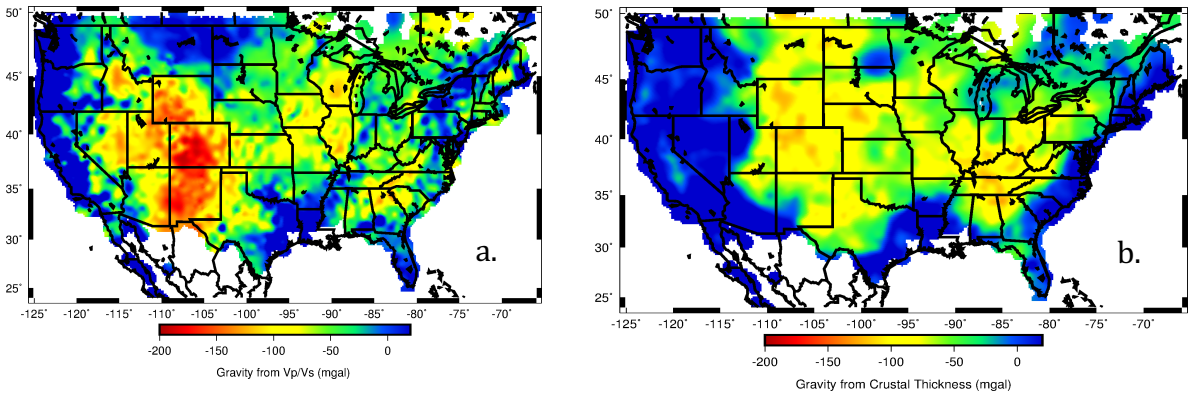

Figure 31: Modeled Bouguer gravity anomalies associated with crustal composition and thickness for the two-layer model. a): Gravity due to crustal compositional variation (i.e., v_P/v_S using equation 3.4). (b): Gravity due to crustal thickness variation. Crustal compositional variation is the dominant contributor to Bouguer gravity, resulting in anomalies that exceed -200 mGal, e.g., in the Rocky Mountains.

3.12. Cross-correlation Cross-sections

To visualize the variations in crustal layer thicknesses, I created vertical cross-sections of the cross-correlation coefficients relating synthetic models to observed receiver functions along profiles at 37°, 40°, 43° and 46° N latitude (Figure 32). Averaged correlation coefficients for all of the models at each station location can be represented as a matrix $\overline{\overline{C}} \equiv C_{ij} = C\left(H_i, \kappa_j\right)$ for all H_i and κ_j combinations of model parameters. The vertical cross-sections plot the vector of cross-correlations corresponding to all H_i sampled at the particular v_P/v_S that yielded the maximum correlation coefficient after multiplication by the OI and gravity likelihood functions.

These were then normalized by a multiplication factor chosen to yield a maximum of one. The profiles cross most of the physiographic and basement age provinces of the United States. The Moho in these images (Figure 33 and 34) is rougher and exhibits greater variance than the mid-crustal boundary. Intriguingly the midcrustal and Moho boundaries show similar topographic deflections in many instances, which likely has implications for the nature of the midcrustal boundary.

There is evidence of other impedance contrasts that are present in some locations. For example, both the midcrustal and Moho boundaries near longitude –113° to –111° in profile A (Figure 33a) are more diffuse than elsewhere and the crustal thickness is only 29 km. This location coincides with magnetotelluric imaging of high electrical conductivities typical of melts in the lower crust and upper mantle. The Moho under the eastern Dakotas is the shallowest found anywhere in the stable continental interior (around –100° to –95° in Figure 31a), in the southwesternmost portion of the Superior basement age province (Whitmeyer & Karlstrom, 2007). There is a weak but still observable impedance contrast beneath at ~45 km depth. Further south at the same longitude, near what would have been the collision zone between the Superior and Yavapai blocks, multiple impedance boundaries are still apparent (around –100° to –95° in Figure 33b), and additional impedance boundaries are evident further west under the collision zone of the Yavapai and Trans-Hudson terranes as well as within the Wyoming craton.

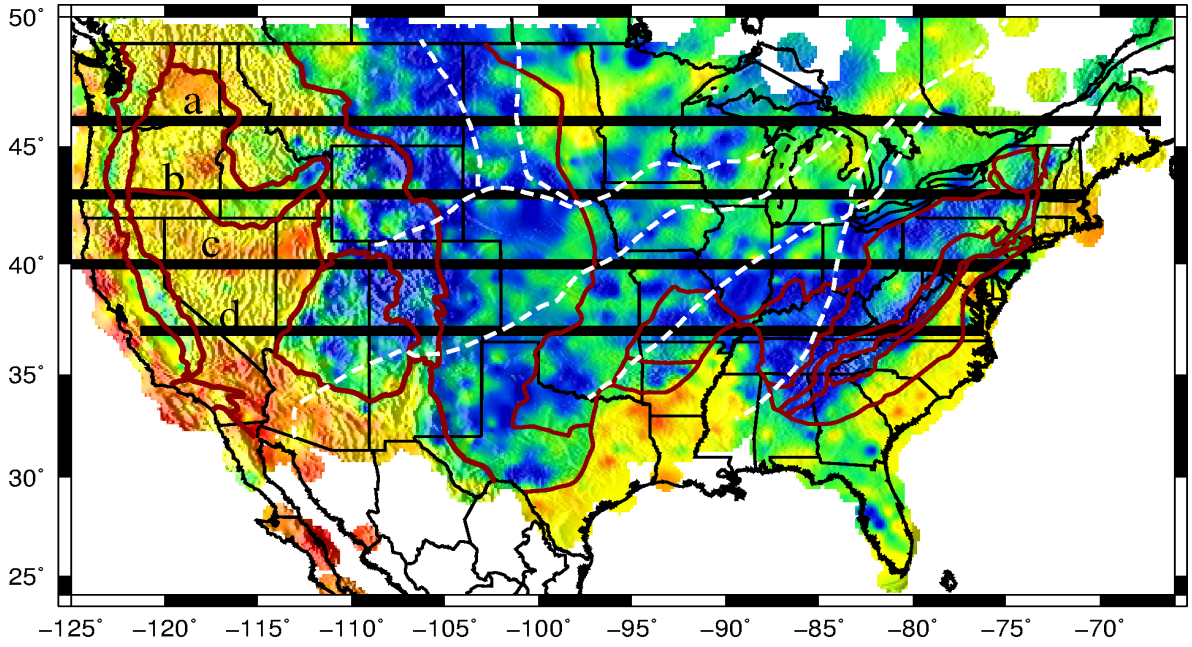

Figure 32: Location map of cross-correlation profiles crossing the United States.

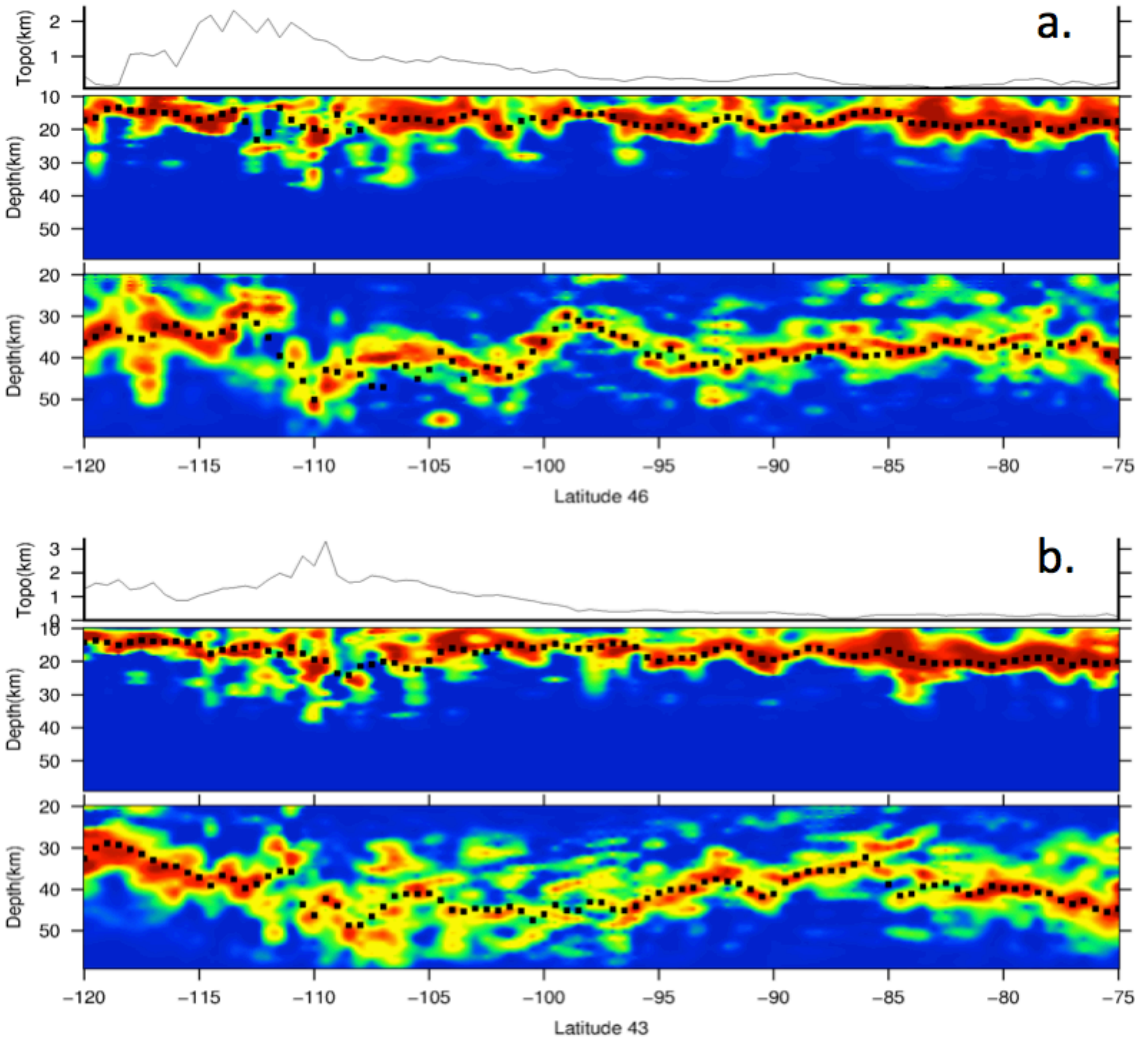

Figure 33: Profiles of receiver function cross-correlation coefficients along latitude 46° and 43° showing topography (top panels), two-layer models (middle) and one-layer models (bottom). Profiles are along latitudes (a) 46°, (b) 43°. Black dots represent final model estimates of the midcrustal boundary and Moho.

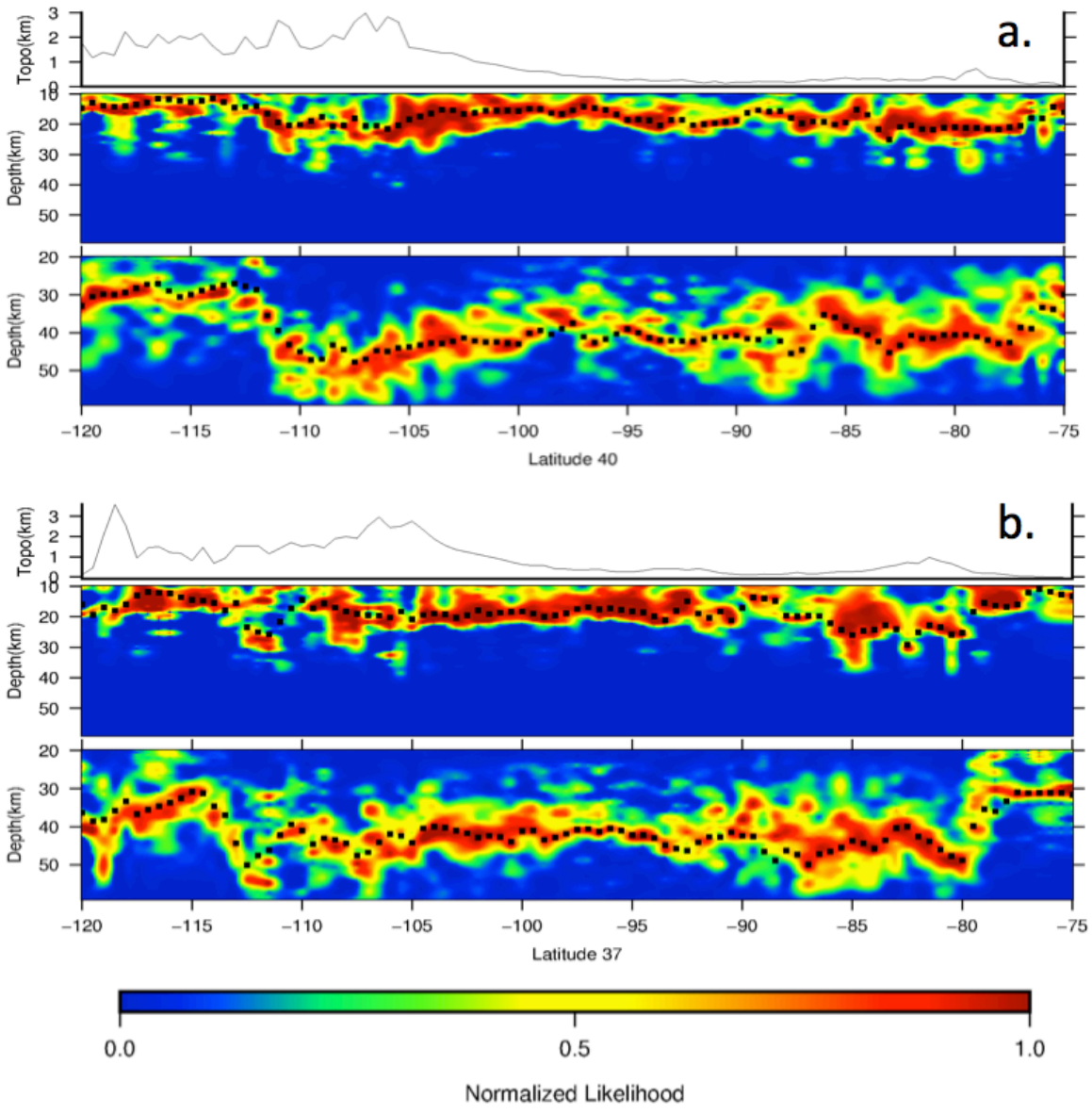

Figure 34: Profiles of receiver function cross-correlation coefficients along latitude 40° and 37° showing topography (top panels), two-layer models (middle) and one-layer models (bottom). Profiles are along latitudes (a) 40°, (b) 37°. Black dots represent final model estimates of the midcrustal boundary and Moho.

3.13. Mineral Physics Modeling

To aid in interpretation of the v_P/v_S and associated density variations for possible composition and mineralogy of the crust, Ma & Lowry (2017) used the thermodynamical model Perple_X (Connolly, 2009). Perple_X models mineral assemblages expected to form as a function of pressure, temperature and chemistry by minimizing the Gibbs free energy at given entropy and volume via linear programming. Thermodynamical modeling was performed with major-element chemical constituents derived from Rudnick & Gao (2003), as shown in Table 2.

Table 2

Crustal chemical composition: Average chemistry of upper, middle and lower continental crust from Rudnick & Gao (2003), used in modeling for this paper.

Wt-%	Na_20	MgO	Al_2O_3	SiO_2	K_2O	FeO	CaO
upper crust	3.27	2.48	15.4	66.62	2.8	3.59	5.04
middle crust	3.39	3.59	15.00	63.5	2.3	5.25	6.02
lower crust	2.65	7.24	16.9	53.4	0.61	9.59	8.57

In order to better understand the role of crustal composition in layering, crustal mineral assemblages are modeled with two different depth-dependencies for crustal chemistry. For the first end-member case, we assume that crustal chemistry changes gradually with depth. In this case, the weight percentage of each major

element linearly interpolates between an upper-crustal chemistry at the surface, midcrustal chemistry at 22.5 km and lower crustal chemistry at 45 km depths, with interpolated sampling at 1 km depth intervals. For this end-member case, any impedance boundaries observed ideally would correspond to phase boundaries resulting from *P*-*T*-dependent changes in minimum-energy packing structure, but may also demonstrate energy sensitivities to small variations in major-element chemistry. For the second end-member, we assume three distinct 15-km-thick layers with uniform chemistries corresponding to upper, middle and lower crust in Table 2. In this end-member impedance contrasts can result from both chemical boundaries and phase boundaries, but one would have to invoke some process by which crustal fractionation processes could generate sharp, laterally contiguous chemical boundaries. Both models assume identical geotherms, with a Moho temperature of 650°C typical of the stable continental interior (Schutt et al., 2017).

Figure 35 shows the first end-member case in which chemistry changes gradually with depth. We also model the changes in mineral assemblages and properties that result with and without a 1 wt-% water constituent included. The thermodynamical models predict that aggregate v_P/v_S of a dry chemistry increases gradually with depth from 1.72–1.75 as the wt-% of quartz gradually decreases (Figure 35a), then decreases sharply to 1.70 in garnet-grade below a depth of 35 km. Adding 1 wt-% of water significantly reduces plagioclase, orthopyroxene and mica while increasing the quartz constituent by up to 10 wt-%, resulting in a significant reduction of aggregate v_P/v_S at all depths except where melt is produced

from consumption of garnet (in this example, below 35 km, but the geotherm used was from the Basin and Range province where the crust is only barely that thick). Density is also reduced by hydration, but the greatest reduction of density occurs deep in the crustal column where garnet is consumed by melting (consistent with the interpretation of xenoliths from the U.S. Cordillera by Jones et al. (2015)). The garnet phase boundary is much deeper than the midcrustal boundary of our two-layer model, and the P velocity in garnet grade is 7+ km/s, so the midcrustal boundary of our two-layer model is unlikely to correspond to that phase boundary. There are smaller impedance contrasts introduced at depths of 12 (hydrous) to 18 (dry) km (Figure 35) that appear to relate to disappearance of muscovite, but changes in v_P/v_S predicted at those depths are subtle to nonexistent.

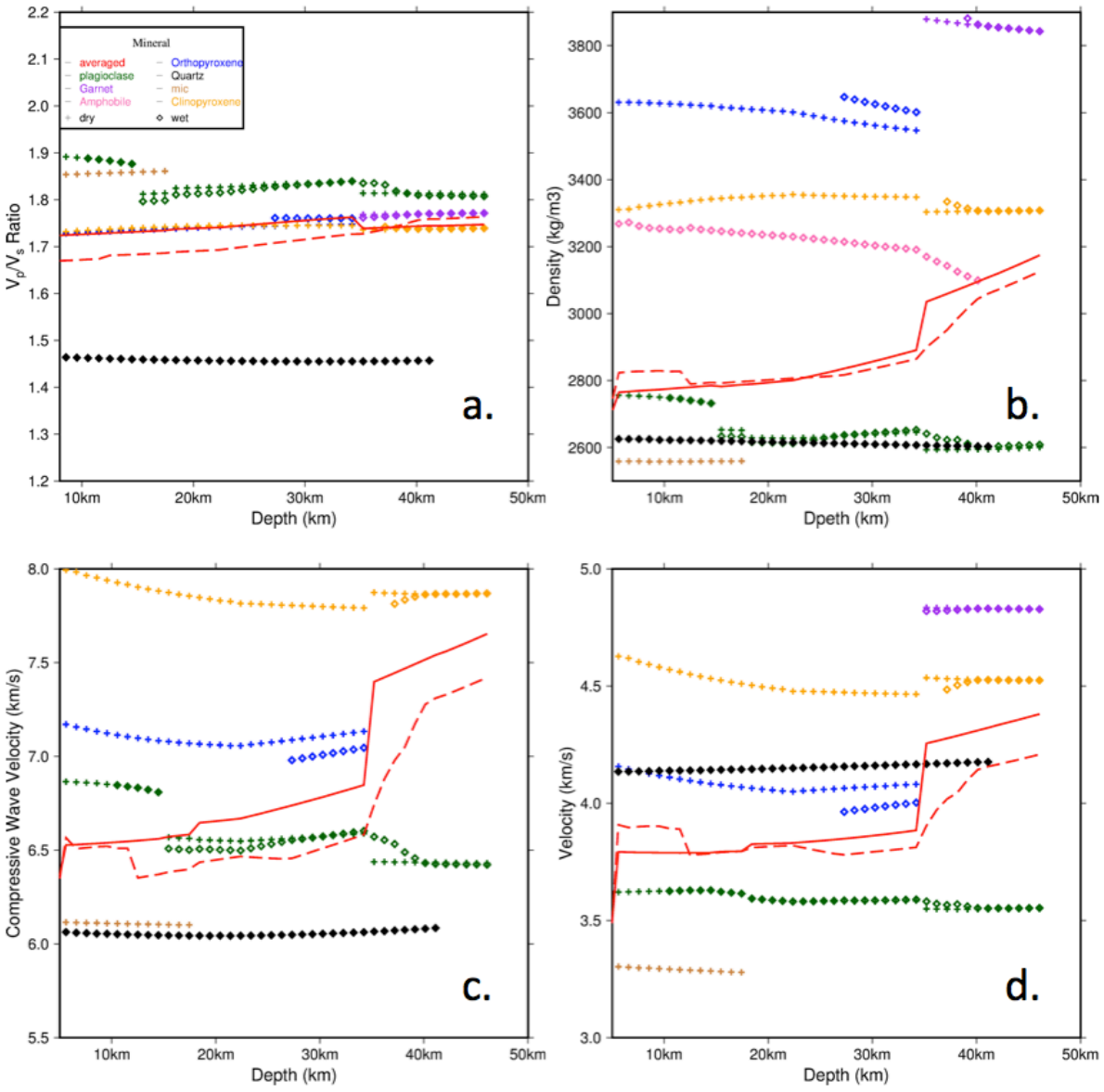

Figure 35: Mineral physics simulation of geophysical properties, assuming a gradual change in major-element crustal chemistry, with and without a 1-wt% hydrous volatile constituent. Red line is aggregate property without hydration; red dashed line is with hydration. (a) v_P/v_S. (b) Density. (c) Compressive wave velocity. (d) Shear wave velocity.

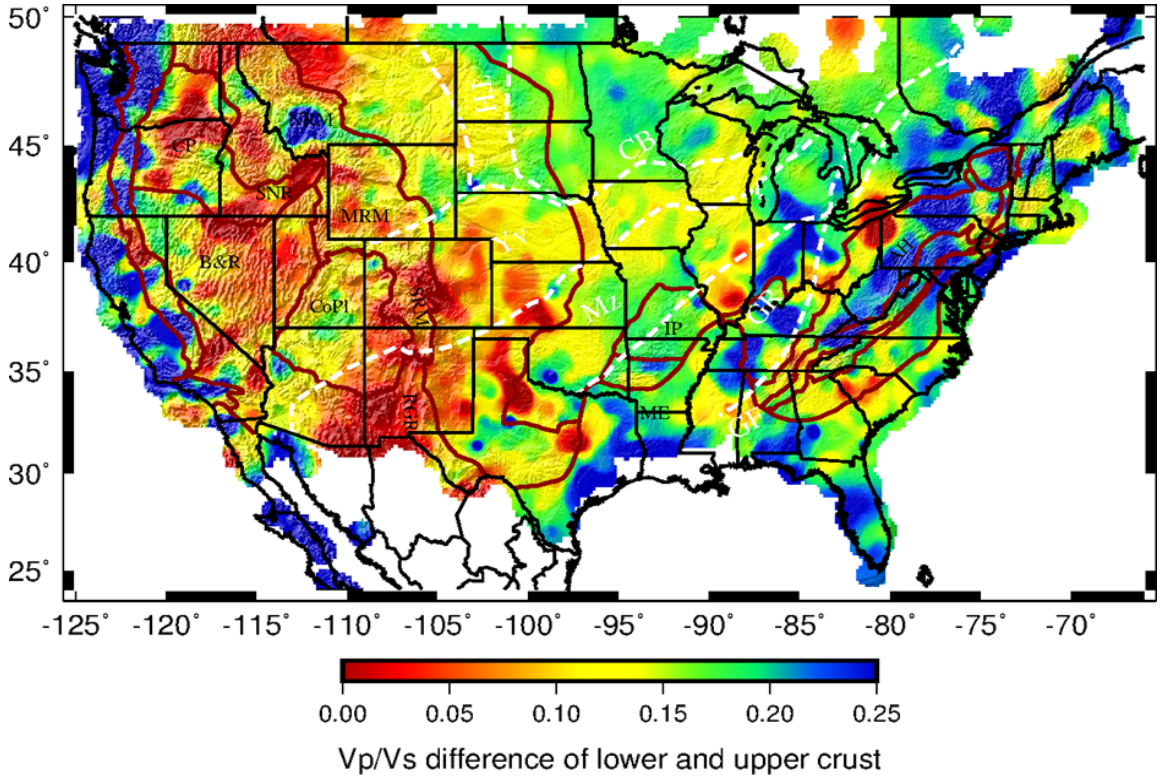

Figure 36: Seismic velocity ratio difference between lower crust (Figure 27) and upper crust (Figure 26).

3.14. Joint Inversion Model Interpretation

Averages of the v_P/v_S from the two-layer model are 1.72 for the upper crust and 1.88 for the lower crust. The lower crustal v_P/v_S of the continental interior U.S. is typically around 1.85, which is consistent with feldspar and pyroxene for crustal rocks from lab experiments (Christensen, 1996) but inconsistent with the v_P/v_S properties above and below the shallower (12–18 km) phase boundaries in Figure 35a. The model with three uniform chemical layers exhibits sharp discontinuities in

velocities and v_P/v_S at the chemical boundaries (Figure 37), and the observed change in v_P/v_S is arguably supported in the case of a dry chemistry. The two-layer model exhibits much smaller differences in v_P/v_S of the upper and lower crust in the western U.S. Cordillera, and much larger differences in the stable eastern U.S (Figure 36). For example, both upper and lower crust in the Snake River Plain and Columbia Plateau have relatively high v_P/v_S ~1.80–1.83, and low v_P/v_S ~1.7 occurs in both upper and lower crust of the Rocky Mountains, Basin and Range and other regions of the western U.S. Cordillera. The largest contrasts in western U.S. v_P/v_S occur in the relatively stable Colorado Plateau and Great Plains provinces. The low v_P/v_S of the Rocky Mountains and Basin and Range likely reflects higher quartz abundance (Lowry & Pérez-Gussinyé, 2011), which in turn is probably a result of hydration (Ma & Lowry, 2017) (see also Figure 35c). Regardless, the thermodynamical modeling suggests that the midcrustal impedance contrast imaged by our modeling more likely represents a chemical boundary than a phase change. There are alternative possibilities, including the possibilities that the impedance relates to anisotropy layering (e.g., Schulte-Pelkum & Mahan, 2014) or that phase behavior might be dramatically different with a different choice of geotherm and composition than we used in our modeling. But if our analysis is correct and a widespread, contiguous chemical boundary exists within the crust, this would imply there is some as-yet unrecognized fractionation dynamic that would be necessary to facilitate such differentiation.

The broader conclusion we draw from this is that much of the crust in the western U.S. Cordillera has experienced hydration at some point in its history, whereas most of the continental crust in the stable continental interior is relatively dry. There are exceptions to both of these generalizations: In the western U.S., oceanic-derived terranes have high v_P/v_S with strong midcrustal contrasts, and the Snake River plain also lacks evidence of hydration (possibly because of large quantities of CO_2 in the hotspot volatile mix, which buffers the aqueous constituent and prevents mineral reactions (e.g., Yardley, 2009)). Conversely, low lower-crustal v_P/v_S in places such as Illinois-Wisconsin and some states along the Atlantic coastal plain (Figure 27) may hint at past subduction-related volatile flux. The utility of v_P/v_S to infer hydration history is liable to be valid regardless of chemistry: Hydration of the deep crust increases the abundance of quartz, consumes pyroxenes, feldspars and garnets, and consequently reduces bulk v_P/v_S and density, which is then reflected in bulk crustal v_P/v_S (Ma & Lowry, 2017).

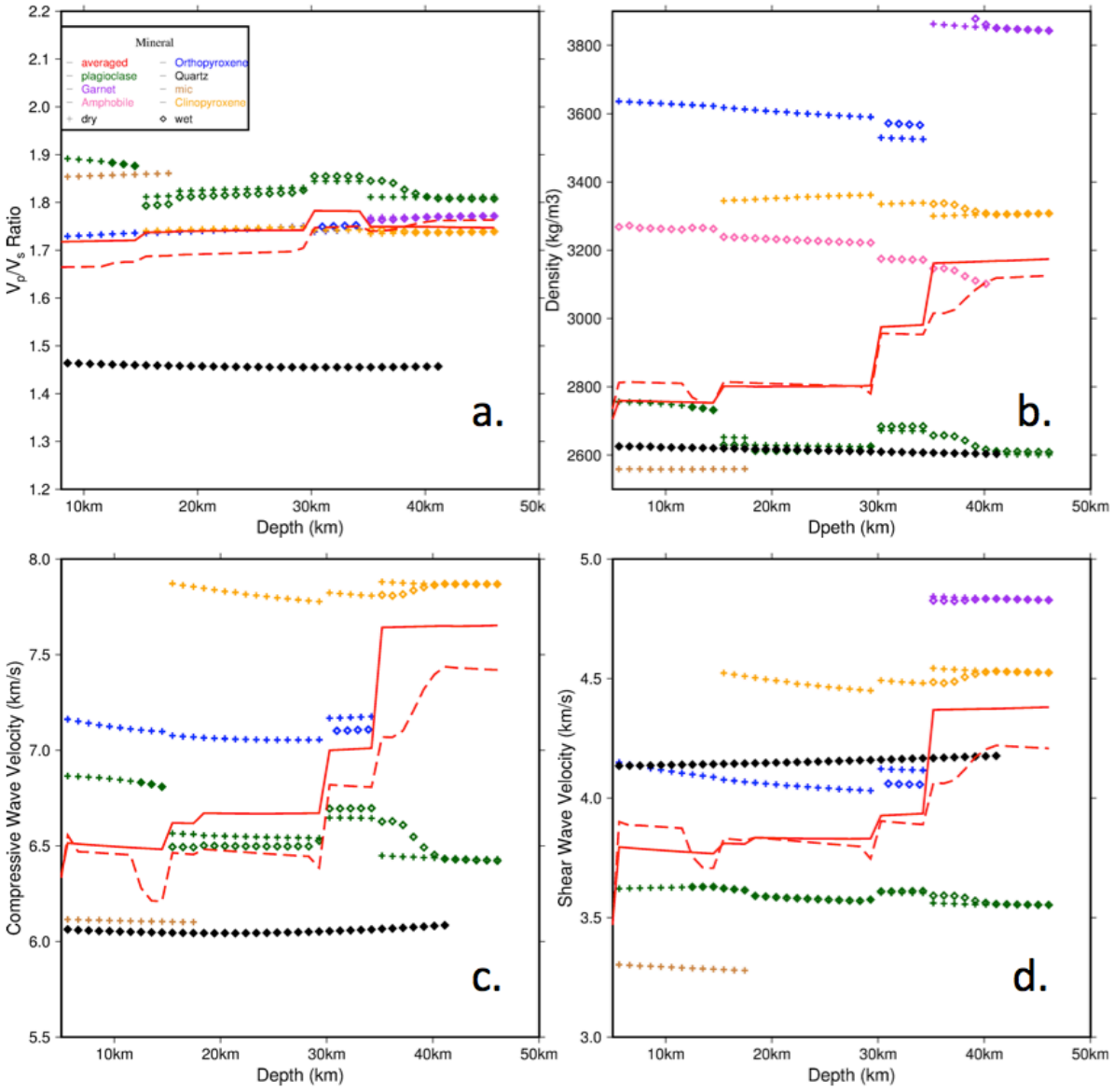

Figure 37: Thermodynamical modeling of mineralogy and geophysical properties assuming three distinct layers with uniform major-element chemistry as described in Table 2, with and without a hydrous volatile constituent (a) v_P/v_S. (b) Density. (c) Compressional seismic wave velocity. (d) Shear wave velocity.

3.15. Discussion

The chemistry of the upper crust is relatively well-sampled from surface exposures (Rudnick & Fountain, 1995; Hacker et al., 2015). Determining the lower crustal chemistry is more problematic due to paucity of surface exposures and sparse sampling by xenoliths, along with the ambiguous relationship between mineral composition and seismic velocity (e.g., Miller & Christensen, 1994; Sobolev & Bakeyko, 1994; Christensen & Mooney, 1995; Kern et al., 1996; Musacchio et al., 1997; Hacker et al., 2015). The seismic velocity ratio, v_P/v_S, is also non-unique with respect to chemistry, but its relative insensitivity to temperature, pressure and high sensitivity to quartz content makes it a potentially valuable tool for investigation of lower crustal mineralogy (Holbrook et al., 1992; Zandt et al., 1994; Christensen, 1996; Lowry & Pérez-Gussinyé, 2011; Ma & Lowry, 2017).

Crustal thickness and bulk v_P/v_S from a single-layer joint inversion shows intriguing relationships to surface geological provinces, and thermodynamical modeling indicates that bulk crustal v_P/v_S may largely reflect hydration history of the crust (Ma & Lowry, 2017). In this paper, we have extended our joint inversion method to image thicknesses and v_P/v_S of a two-layer crustal model. The difference in v_P/v_S of the upper and lower crustal layers was found to be large, ~0.15–0.2, over most of the stable interior of the United States but nearer zero in much of the deforming regions of the western U.S. Cordillera. Thermodynamical models of mineralogy with and without hydration present suggest that low bulk and lower-crustal v_P/v_S observed in the western U.S. may be indicative of hydration of the

crust, whereas the patterns of differences in upper- and lower-crustal v_P/v_S is more consistent with an impedance contrast corresponding to a change in major element chemistry than with a phase boundary. Guerri et al (2015) suggested a phase transition from plagioclase to clinopyroxene in the midcrust might be responsible for crustal seismic velocity discontinuities. Our analysis differs from theirs in that they varied temperature to match velocities and densities in Crust1.0, whereas we used a geotherm consistent with conductive thermal transfer through the lithosphere. As a result, we found the weight percentage of plagioclase slightly decreasing near 15 km, then gradual increasing down to 35 km, where plagioclase breaks down to clinopyroxene. The modeling of an ultra-fast seismic layer matches results from Guerri et al. (2015), but ours occurs at greater depth. The ultra-high seismic velocity might represent a lowermost crustal layer observed in some crustal-scale seismic refraction surveys (Braile, 1989; Prodehl & Lippman, 1989).

The observation that low v_P/v_S of the lower crust in the Rocky Mountain provinces might indicate a hydration event (Ma & Lowry, 2017) is consistent with Jones et al.'s (2015) interpretation that hydration observed in a handful of lower crustal xenoliths is evidence for widespread hydration of the Cordillera. Our thermodynamical modeling also supports their interpretation that hydration of the lower crust consumes garnet, reduces crustal density, and may have contributed to elevation of the western United States Cordillera following the Laramide flat slab episode. The elevation change associated with consumption of garnet can be calculated as $\Delta h = t\Delta\rho / \rho_a$, where h is elevation, t is thickness of the layer in which

density changed due to hydration, and ρ_a is density of the asthenosphere. The density change inferred from xenolith samples for complete consumption of garnet is 290 kg/m^3 (Jones et al., 2015), and assuming a ~15 km thick layer of garnet-grade crust, the elevation change would be about 1.2 km. The additional ~50 kg/m^3 density decrease our modeling suggests at midcrustal depths (Figure 30b) would add up to 160 m to the total, providing more than half the elevation change observed since Mesozoic.

3.16. Conclusions

Imaging of thicknesses and v_P/v_S of a two-layer crust across the United States has been achieved by joint inversion of seismic receiver functions with likelihoods derived from gravity modeling and spatial statistics. The upper crust has a thickness of 16.8 ± 3.8 km and v_P/v_S of 1.72 ± 0.03. The lower crust has thickness 22.4 ± 4.7 km and v_P/v_S 1.88 ± 0.11.

Crustal thickness (Figures 26 and 27) exhibits interesting relationships to physiographic and basement provinces. The upper crust is found to be thin wherever the whole crust is thin, including in extensional provinces of the western U.S., the Mississippi embayment and Atlantic coastal plains, and the southeastern Superior province. There is also an arcuate zone of thinner upper crust corresponding to the Great Plains states from North Dakota to Texas, roughly coincident with where Tikoff & Maxson (2001) inferred lithospheric buckling associated with Laramide flat-slab

subduction. The thickest upper crust occurs in the Rocky Mountains and Appalachian Highlands, consistent with earlier inferences from seismic refraction surveys (Braile et al., 1989; Taylor, 1989). These regions all have experienced significant contractional deformation and so the greater thickness may partly reflect that history.

Relative to the single-layer model of Ma & Lowry (2017), the contribution of crustal compositional mass to gravity anomalies is increased, making it unequivocally the largest seismically-imaged contributor to gravity. The estimated mean Moho density contrast in the eastern (193 kg/m^3) and western (256 kg/m^3) United States differs by 63 kg/m^3, which is about 20 kg/m^3 larger than inferred by Ma & Lowry (2017). Schmandt et al. (2015) calculated a much larger difference of 220 kg/m^3, but these estimates are not incompatible given that our $\Delta\rho_{\text{Moho}}$ estimates do not include east-to-west differences in mean lower crustal and upper mantle densities, which our approach estimates separately, and which our analyses show to predominantly reflect hydration-related consumption of garnet and lower upper mantle temperatures in the western U.S. After subtracting gravity anomalies due to crustal composition, thickness and thermal variation from measured Bouguer gravity, most of the residual gravity is likely related to asthenospheric mantle density variations (e.g., Becker et al., 2014), although some residual gravity anomalies may be amplified by the presence of crustal melt. Most of the whole-crustal variation of v_P/v_S relates to large variations of v_P/v_S in the lower crust, but large basaltic volcanic

provinces like the Columbia Plateau and Snake River plain also exhibit high upper crustal v_P/v_S anomalies.

Thermodynamical modeling of the equations of state for mineral formation and geophysical properties suggests the midcrustal impedance contrast imaged for this paper may represent a chemical boundary rather than a mineralogical phase change. Low v_P/v_S of the lower crust in the western U.S. Cordillera implies widespread hydration of the lower crust. Hydration increases the abundance of quartz (Figure 35c), which reduces the seismic velocity ratio throughout the crust (Figures 19 and 35a). Hydration also reduces density in the lower crust as it consumes garnet to produce partial melts (Figure 35b). The crustal density decrease associated with hydration derived from Farallon flat-slab subduction could be responsible for up to 1.4 km of post-Laramide elevation of the western U.S. Finally, crustal hydration may have the simultaneous effects of lowering the Moho temperature (by absorption of heat to accommodate latent heat of fusion in the lower crust) and increasing the surface heat flow (by a combination of hydration reaction enthalpy at shallower depths and migration of melts toward the surface). This phenomenon may explain large discrepancies observed between Pn-derived estimates of Moho temperature and predictions of deep temperature derived from surface heat flow in regions of high elevation (Berry et al., 2015).

Acknowledgments

Receiver functions used here were acquired from the EarthScope Automated Receiver Survey (EARS) (Crotwell & Owens, 2005; IRIS DMC, 2010; Trabant et al., 2012), including USArray and other seismic networks. Bouguer gravity data are from the WGM2012 International Gravimetric Bureau global map (Balmino et al., 2011; Bonvalot et al., 2012). This project was supported by National Science Foundation grants EAR-0955909, EAR-1246977, and EAR-1358622 from the Geophysics and EarthScope science programs.

References

Afonso, J. C., G. Ranalli, & M. Fernandez (2005). Thermal expansivity and elastic properties of the lithospheric mantle: results from mineral physics of composites. *Physics of the Earth and Planetary Interiors*, *149*(3), 279-306. https://doi.org/10.1016/j.pepi.2004.10.003.

Ammon, C. J. (1991). The isolation of receiver effects from teleseismic P waveforms. *Bulletin of the Seismological Society of America*, *81*(6), 2504-2510.

Balmino, G., N. Vales, S. Bonvalot, & A. Briais (2011). Spherical harmonic modeling to ultra-high degree of Bouguer and isostatic anomalies. *Journal of Geodesy*, *86*(7), 499-520. https://doi.org/10.1007/s00190-011-0533-4.

Beck, J. V., & K. J. Arnold (1977). *Parameter Estimation in Engineering and Science*. John Wiley & Sons, New York.

Becker, T. W., C. Faccenna, E. D. Humphreys, A. R. Lowry, & M. S. Miller (2014). Static and dynamic support of western United States topography. *Earth and Planetary Science Letters*, *402*, 234-246. https://doi.org/10.1016/j.epsl.2013.10.012.

Becker, T. W., A. R. Lowry, C. Faccenna, B. Schmandt, A. Borsa, & C. Yu (2015). Western US intermountain seismicity caused by changes in upper mantle flow. *Nature*, *524*(7566), 458-461. https://doi.org/10.1038/nature14867.

Berry, M. A., A. R. Lowry, & D. L. Schutt (2015). Cold and wet at the roots of U.S. Cordilleran high elevation. Abstr. #T11C-2910, AGU Fall Meeting, San Francisco CA.

Bonvalot, S., G. Balmino, A. Briais, M. Kuhn, A. Peyrefitte, N. Vales, R. Biancale, G. Gabalda, F. Reinquin, & M. Sarrailh (2012). World Gravity Map, *Bureau Gravimetrique International* (*BGI*), Map, CGMW-BGI-CNES728, IRD, Paris.

Braile, L. W., W. J. Hinze, R. R. B. Von Frese, & G. R. Keller (1989). Seismic properties of the crust and uppermost mantle of the conterminous United States and adjacent Canada. *Geological Society of America Memoirs*, *172*, 655-680. https://doi.org/10.1130/MEM172-p655.

Buehler, J. S., & P. M. Shearer (2017). Uppermost mantle seismic velocity structure beneath USArray. *Journal of Geophysical Research* in press. https://doi.org/10.1002/2016JB013265.

Bürgmann, R., & G. Dresen (2008). Rheology of the lower crust and upper mantle: Evidence from rock mechanics, geodesy, and field observations. *Annual Reviews of Earth and Planetary Sciences*, *36*, 531-567. https://doi.org/10.1146/annurev.earth.36.031207.124326.

Christensen, N. I. (1996). Poisson's ratio and crustal seismology. *Journal of Geophysical Research*, *101*(B2), 3139-3156. https://doi.org/10.1029/95JB03446.

Christensen, N. I., & D. M. Fountain (1975). Constitution of the lower continental crust based on experimental studies of seismic velocities in granulite. *Geological Society of America Bulletin*, *86*(2), 227-236. https://doi.org/10.1130/0016-7606(1975)86%3C227:COTLCC%3E2.0.CO;2

Christensen, N., & W. Mooney (1995). Seismic velocity structure and composition of the continental crust: A global view. *Journal of Geophysical Research*, *100*(B6), 9761-9788. https://doi.org/10.1029/95JB00259

Connolly, J. A. D. (2009). The geodynamic equation of state: what and how. *Geochemistry, Geophysics, Geosystems*, *10*(10). https://doi.org/10.1029/2009GC002540.

Cooper, G. R. J., & Cowan, D. R. (2005). Differential reduction to the pole. *Computers & Geosciences, 31*(8), 989-999. https://doi.org/10.1016/j.cageo.2005.02.005

Crotwell, H. P., & T. J. Owens (2005). Automated receiver function processing. *Seismological Research Letters*, *76*(6), 702-709. https://doi.org/10.1785/gssrl.76.6.702.

Davis, J. C. (1986). *Statistics and Data Analysis in Geology* (2nd edn). Wiley, New York.

Dziewonski, A. M., & D. L. Anderson (1981). Preliminary reference Earth model. *Physics of the Earth and Planetary Interiors*, *25*(4), 297-356. https://doi.org/10.1016/0031-9201(81)90046-7.

Geist, D., & Richards, M. (1993). Origin of the Columbia Plateau and Snake River plain: Deflection of the Yellowstone plume. *Geology, 21*(9), 789-792. https://doi.org/10.1130/0091-7613(1993)021%3C0789:OOTCPA%3E2.3.CO;2

Guerri, M., F. Cammarano, & J. A. Connolly (2015). Effects of chemical composition, water and temperature on physical properties of continental crust. *Geochemistry, Geophysics, Geosystems*, *16*(7), 2431-2449. https://doi.org/10.1002/2015GC005819.

Green, J. C. (1983). Geologic and geochemical evidence for the nature and development of the Middle Proterozoic (Keweenawan) Midcontinent Rift of North America. *Tectonophysics, 94*(1), 413-437. https://doi.org/10.1016/0040-1951(83)90027-6

Hacker, B. R., P. B. Kelemen, & M. D. Behn (2015). Continental lower crust. *Annual Reviews of Earth and Planetary Sciences*, *43*, 167-205. https://doi.org/10.1146/annurev-earth-050212-124117

Holbrook, W. S., W. D. Mooney, & N. I. Christensen (1992). The seismic velocity structure of the deep continental crust. In D. M. Fountain, R. Arculus, R. W. Kay (Eds.) *Continental Lower Crust*, pp. 1–43, Elsevier Sci., New York.

Humphreys, E., E. Hessler, K. Dueker, G. L. Farmer, E. Erslev, & T. Atwater (2003). How Laramide-age hydration of North American lithosphere by the Farallon slab controlled subsequent activity in the western United States. *International Geology Review, 45*(7), 575-595. https://doi.org/10.2747/0020-6814.45.7.575.

IRIS DMC (2010), Data Services Products: EARS EarthScope Automated Receiver Survey. https://doi.org/10.17611/DP/EARS.1

Ito, T., & M. Simons (2011). Probing asthenospheric density, temperature and elastic moduli below the western United States. *Science*, *332*(6032), 947-951. https://doi.org/10.1126/science.1202584

Jones, C. H., K. H. Mahan, L. A. Butcher, W. B. Levandowski, & G. L. Farmer (2015). Continental uplift through crustal hydration. *Geology*, *43*(4), 355-358. https://doi.org/10.1130/G36509.1

Julià, J. (2007). Constraining velocity and density contrasts across the crust—mantle boundary with receiver function amplitudes. *Geophysical Journal International*, *171*(1), 286-301. https://doi.org/10.1111/j.1365-2966.2007.03502.x

Kern, H., S. Gao, & Q. S. Liu (1996). Seismic properties and densities of middle and lower crustal rocks exposed along the North China Geoscience Transect. *Earth and Planetary Science Letters*, *139*(3-4), 439-455. https://doi.org/10.1016/0012-821X(95)00240-D

Kohlstedt, D. L. (2006). The role of water in high-temperature rock deformation. *Reviews of Mineralogy and Geochemistry*, *62*(1), 377-396. https://doi.org/10.2138/rmg.2006.62.16

Kono, Y., A. Miyake, M. Ishikawa, & M. Arima (2008). Temperature derivatives of elastic wave velocities in plagioclase (An51±1) above and below the order-disorder transition temperature. *American Mineralogist*, *93*(4), 558-564. https://doi.org/10.2138/am.2008.2591.

Laske, G., Masters, G., Ma, Z., & Pasyanos, M. (2013, April). Update on CRUST1. 0—A 1-degree global model of Earth's crust. *Geophysical Research Abstracts* (Vol. 15, p. 20132658abstrEGU).

Levander, A., & M. S. Miller (2012). Evolutionary aspects of lithosphere discontinuity structure in the western US. *Geochemistry, Geophysics, Geosystems*, *13*(7). https://doi.org/10.1029/2012GC004056.

Ligorría, J. P., & C. J. Ammon (1999). Iterative deconvolution and receiver-function estimation. *Bulletin of the Seismological Society of America*, *89*(5), 1395-1400.

Lin, F. C., B. Schmandt, & V. C. Tsai (2012). Joint inversion of Rayleigh wave phase velocity and ellipticity using USArray: Constraining velocity and density structure in the upper crust. *Geophysical Research Letters*, *39*(12). https://doi.org/10.1029/2012GL052196.

Lowry, A. R., & M. Pérez-Gussinyé (2011). The role of crustal quartz in controlling Cordilleran deformation. *Nature*, *471*(7338), 353-357. https://doi.org/10.1038/nature09912.

Lowry, A. R., N. M. Ribe, & R. B. Smith (2000). Dynamic elevation of the Cordillera, western United States. *Journal of Geophysical Research*, *105*(B10), 23371-23390. https://doi.org/10.1029/2000JB900182.

Ma, X, & A. R. Lowry (2017). USArray imaging of continental crust in the conterminous United States. *Tectonics*, in press. https://doi.org/10.1002/2017TC004540

Maggi, A., Jackson, J. A., Mckenzie, D., & Priestley, K. (2000). Earthquake focal depths, effective elastic thickness, and the strength of the continental lithosphere. *Geology, 28*(6), 495-498. https://doi.org/10.1130/0091-7613(2000)28%3C495:EFDEET%3E2.0.CO;2

Martinec, Z. (1994). The density contrast at the Mohorovičic discontinuity. *Geophysical Journal International*, *117*(2), 539-544. https://doi.org/10.1111/j.1365-246X.1994.tb03950.x

Meqbel, N. M., G. D. Egbert, P. E. Wannamaker, A. Kelbert, & A. Schultz (2014). Deep electrical resistivity structure of the northwestern US derived from 3-D inversion of USArray magnetotelluric data. *Earth and Planetary Science Letters, 402*, 290-304. https://doi.org/10.1016/j.epsl.2013.12.026

Miller, D. J., & N. L. Christensen (1994). Seismic signature and geochemistry of an island arc: A multidisciplinary study of the Kohistan accreted terrane, northern Pakistan. *Journal of Geophysical Research*, *99*(B6), 11623-11642. https://doi.org/10.1029/94JB00059

Musacchio, G., W. D. Mooney, J. H. Luetgert, & N. I. Christensen (1997). Composition of the crust in the Grenville and Appalachian Provinces of North America inferred from v_P/v_S ratios. *Journal of Geophysical Research*, *102*(B7), 15225-15241. https://doi.org/10.1029/96JB03737.

Niu, F., & D. E. James (2002). Fine structure of the lowermost crust beneath the Kaapvaal craton and its implications for crustal formation and evolution. *Earth and Planetary Science Letters*, *200*(1), 121-130. https://doi.org/10.1016/S0012-821X(02)00584-8

Pakiser, L. C. (1989). Geophysics of the Intermontane system. *Geological Society of America Memoirs*, *172*, 235-248. https://doi.org/10.1130/MEM172-p235.

Prodehl, C., & Lipman, P. W. (1989). Crustal structure of the Rocky Mountain region. *Geological Society of America Memoirs, 172*, 249-284. https://doi.org/10.1130/MEM172-p249

Ravat, D., C. Finn, P. Hill, R. Kucks, J. Phillips, R. Blakely, C. Bouligand, T. Sabaka, A. Elshayat, A. Aref, & E. Elawadi (2009). A preliminary, full-spectrum, magnetic anomaly grid of the United States with improved long wavelengths for studying continental dynamics. *U. S. Geological Survey Open-File Report 2009-1258*.

Rudnick, R. L., & D. M. Fountain (1995). Nature and composition of the continental crust: a lower crustal perspective. *Reviews of Geophysics*, *33*(3), 267-309. https://doi.org/10.1029/95RG01302.

Rudnick, R. L., & S. Gao (2003). The composition of the continental crust. In R. L. Rudnick (Ed.) *The Crust*, pp. 1–64, Elsevier-Pergamon, Oxford, U. K., https://doi.org/10.1016/B0-08-043751-6/03016-4

Schmandt, B., F. C. Lin, & K. E. Karlstrom (2015). Distinct crustal isostasy trends east and west of the Rocky Mountain Front. *Geophysical Research Letters*, *42*(23), 10290-10298.https://doi.org/10.1002/2015GL066593.

Schulte-Pelkum, V., & Mahan, K. H. (2014). A method for mapping crustal deformation and anisotropy with receiver functions and first results from USArray. *Earth and Planetary Science Letters, 402*, 221-233. https://doi.org/10.1016/j.epsl.2014.01.050

Schutt, D. L., A. R. Lowry, & J. S. Buehler (2017). Moho temperature and mobility of lower crust in the western United States. *Geology*, accepted for publication.

Shen, W., & M. H. Ritzwoller (2016). Crustal and uppermost mantle structure beneath the United States. *Journal of Geophysical Research*, *121*(6), 4306-4342. https://doi.org/10.1002/2016JB012887.

Smith, R. B., W. C. Nagy, K. A. S. Julander, J. J. Viveiros, C. A. Barker, & D. G. Gants (1989). Geophysical and tectonic framework of the eastern Basin and Range-Colorado Plateau-Rocky Mountain transition. *Geological Society of America Memoirs*, *172*, 205-234. https://doi.org/10.1130/MEM172-p205.

Sobolev, S. V., & A. Y. Babeyko (1994). Modeling of mineralogical composition, density and elastic wave velocities in anhydrous magmatic rocks. *Surveys of Geophysics*, *15*(5), 515-544. https://doi.org/10.1007/BF00690173.

Taylor, S. R. (1989). Geophysical framework of the Appalachians and adjacent Grenville Province. *Geological Society of America Memoirs*, *172*, 317-348. https://doi.org/10.1130/MEM172-p317.

Tenzer, R., P. Novák, V. Gladkikh, & P. Vajda (2012). Global crust-mantle density contrast estimated from EGM2008, DTM2008, CRUST2.0, and ICE-5G. *Pure and Applied Geophysics*, 169(9), 1663-1678. https://doi.org/10.1007/s00024-011-0410-3.

Trabant, C., A. R. Hutko, M. Bahavar, R. Karstens, T. Ahern, & R. Aster (2012). Data Products at the IRIS DMC: Stepping Stones for Research and Other Applications, *Seismological Research Letters*, *83*(5), 846–854. https://doi.org/10.1785/0220120032.

Wagner, L. S., M. J. Fouch, D. E. James, & S. Hanson-Hedgecock (2012). Crust and upper mantle structure beneath the Pacific Northwest from joint inversions of ambient noise and earthquake data. *Geochemistry, Geophysics, Geosystems*, *13*(12). https://doi.org/10.1029/2012GC004353.

Watts, A. B., & Burov, E. B. (2003). Lithospheric strength and its relationship to the elastic and seismogenic layer thickness. *Earth and Planetary Science Letters, 213*(1), 113-131. https://doi.org/10.1016/S0012-821X(03)00289-9.

Whitmeyer, S. J., & K. E. Karlstrom (2007). Tectonic model for the Proterozoic growth of North America. *Geosphere*, *3*(4), 220-259. https://doi.org/10.1130/GES00055.1.

Zandt, G., S. C. Myers, & T. C. Wallace (1995). Crust and mantle structure across the Basin and Range ‐ Colorado Plateau boundary at 37 N latitude and implications for Cenozoic extensional mechanism. *Journal of Geophysical Research*, *100*(B6), 10529-10548. https://doi.org/10.1029/94JB03063

Zhu, L., & H. Kanamori (2000). Moho depth variation in southern California from teleseismic receiver functions. *Journal of Geophysical Research*, *105*(B2), 2969-2980. https://doi.org/10.1029/1999JB900322.

CHAPTER 4

SIMULATION OF THERMAL TRANSFER PROCESSES ASSOCIATED WITH CRUSTAL HYDRATION

Abstract

Expressions of tectonism in the western U.S. Cordillera, including Cenozoic uplift to high elevations, high surface heat flow, and broadly distributed faulting and magmatism, have diverse possible causes that remain enigmatic. The Cordilleran lower crust has low seismic velocities and low electrical resistivity that, coupled with low v_P/v_S and xenolith samples, suggest hydration following Laramide flat-slab subduction may be an important contributor to lithospheric buoyancy, high surface elevation and lithospheric weakening. Here we simulate hydration processes and associated thermal transfer in the crust using thermodynamical modeling of temperature changes associated with hydration, and conductive thermal transfer of the resulting anomalies. We find that the unusually high surface heat flow in the Cordillera cannot be explained solely by thermal conduction of heat released by upper crustal hydration reactions, implying that advective heat transfer by movement of melts and/or volatiles up the crustal column must contribute a significant fraction of observed surface heat flow. Modeling of the timescales on which perturbations to Moho temperature and surface heat flow would grow and attenuate by thermal conduction further suggest that the hydration and associate melt/advection

processes must have continued until very recently, at least within the last 10–15 million years.

4.1. Introduction

Among the important goals identified for the EarthScope Major Research Facilities and Equipment project is an improved understanding of the mechanisms and dynamical processes responsible for continental deformation (Williams et al., 2010). The structure and deformation of the tectonically active western U.S. Cordillera has been studied intensively from both geophysical and geological perspectives for decades (Burchfiel et al., 1992; Humphreys & Dueker, 1994; Lowry & Smith, 1995; Tikoff & Maxson, 2001; Bennett et al., 1998). As EarthScope has grown to play an increasingly important role in imaging of the region, however, it has become increasingly apparent that Laramide flat slab subduction and associated processes of volatile flux, melt flux and thermal transfer played a very important role in the modern expressions of Cordilleran tectonism (Humphreys et al., 2003; Frassetto et al., 2009; Roy & Pederson, 2009; Lowry & Pérez-Gussinyé, 2011; Becker et al., 2015; Jones et al., 2015; Ma & Lowry, 2017). Specifics of how these processes influenced the region, however, including timing and the relative roles of temperature, volatiles and melts, remains poorly constrained. Berry et al. (2015) inferred a colder than expected mantle under high elevations of the western U.S. Cordillera based on discrepancies between temperature from mineral physics

modeling of Pn velocity and steady-state conductive forward modeling of surface heat flow. Ma & Lowry (2017) found, based on thermodynamical modeling of mineral equations of state, that hydration of crustal rocks would release heat in the mid-to upper-crust but absorbs heat in garnet grade by consumption of garnet into melts. Surface heat flow in the U.S. Cordillera commonly exceeds 80 mW/m^2, which is too high to attribute to extensional strain advection at Cordilleran strain rates, but both melt advection and hydration reactions might increase surface heat flow. Given observations of low lower-crustal v_P/v_S and low electrical resistivity, we hypothesize that hydration might play an important role for tectonism of the region.

Rock rheology controls deformation and the interactions of the crust and mantle, and is similarly determined by mineralogy, temperature, pressure and hydration state (Bürgmann & Dresen, 2008). Teasing apart the contributions of hydration state and temperature variations to rheology and buoyancy is key to understanding tectonism, uplift, and earthquake hazard (e.g., Becker et al., 2015). High elevation of the Cordillera beyond 1000 km from the plate margin, particularly in regions like the Colorado Plateau that were at sea level in the Cretaceous, has been a controversial research topic for decades. The uplift is attributed to four different processes, each associated with flat-slab subduction during the Laramide orogeny. Dynamical surface subsidence associated with slab negative buoyancy was likely small (of order a few hundred m, neglecting isostatic response to sediment loads (Pang & Nummedal, 1985; Liu et al., 2011)) but its recovery contributed to total uplift. Minor amounts of crustal thickening by structural

contraction and magmatic addition likely contributed up to a few hundred meters more (Bird, 1988; Humphreys, 1995). Thermal expansion associated with both convective and advective warming following Farallon slab detachment has been suggested to contribute more significantly (Roy et al., 2009, 2016), and dewatering of the slab far inland of the plate boundary hydrated the lithosphere, causing regional uplift associated with consumption of garnet that is evident in lower crustal xenoliths (Humphreys et al., 2003; Jones et al., 2015).

Each of these processes would have a potentially different time-history that might help with attribution. Dynamical uplift would commence immediately following steepening of the slab ~55-50 Ma, while Laramide contraction continued to about 35 Ma (Livaccari, 1991) and voluminous Tertiary magmatism to ~25 Ma (Humphreys, 1995). The timing of thermal uplift would depend on whether it is driven primarily by conductive or advective warming following removal of the Laramide slab, and the amount depends on how much the slab cooled the overriding lithosphere. Dynamical modeling suggests relatively little cooling because the slab remains separated from the base of continental lithosphere by a chilled and sluggish asthenospheric wedge (Kanda et al., 2017). Hydration contributions to uplift are especially enigmatic because the equations of state for buoyancy associated with hydration are somewhat poorly constrained, and the timing depends on mechanisms of transfer (i.e., in melts versus strain-driven diffusion) that are also poorly known. However, diffusion coefficients in olivine are extremely high (Demouchy & Mackwell, 2006), and high $^{3}He/^{4}He$ ratios over Peruvian flat-slab also suggest volatile flux is

contemporaneous with flat-slab subduction (Newell et al., 2015), consistent with hydration-related uplift occurring during and/or soon after flat-slab subduction.

Observations of timing from paleoelevation and surface process indicators of uplift/subsidence have not reached consensus (e.g., McMillan et al., 2006), but observations that speak to timing and mechanisms of hydration might be extremely valuable in constraining the problem of Cordilleran uplift. Imaging of low modern seismic velocity and electrical resistivity in the lower crust throughout the Cordillera has been variously interpreted in terms of hydration state (Jones et al., 2015; Porter et al., 2017) or partial melts (Meqbel et al., 2014; Lin et al., 2014). Imaging and mineral physics modeling of v_P/v_S of the lower crust suggests that the anomalies can be at least partially attributed to hydration state, but that this should produce signatures in lower crustal melting and heat transfer as well (Ma & Lowry, 2017a; 2017b). Here we examine geothermal temperature and surface heat flow variations expected as a function of time following hydration, by modeling the time-dependence of conductive thermal transfer following hydration perturbations.

4.2 Thermal Modeling

A role for hydration in uplift and magmatism of the western U.S. Cordillera, as a direct result of Farallon flat-slab dynamics, has been speculated about for decades (Humphreys et al*.,* 2003; Levander et al., 2011; Jones et al*.*, 2015; Roy et al*.,* 2016). The hypotheses have been largely qualitative because hydration mechanisms, equations of state and relevant observations of subsurface properties have all been

poorly constrained or ambiguous. The seismic velocity ratio, v_P/v_S, from joint inversion of seismic receiver functions and Bouguer gravity has shown promise for determining both the lateral and vertical spatial distribution of crustal hydration (Ma & Lowry, 2017a; 2017b), but the timing of past hydration is indeterminate from v_P/v_S alone (for example, low v_P/v_S observed in the eastern United States likely dates back to initiation of Atlantic rifting and earlier). A potentially important clue is provided by observations of discrepancies between surface heat flow measurements and mineral physics estimates of Moho temperature from Pn which show Moho temperatures to be much colder than expected beneath Cordilleran high elevations (Berry et al., 2015). Ma & Lowry (2017a; 2017b) suggest that crustal hydration is a process by which such a discrepancy can be generated, but any such mismatch between surface heat flow and deep temperature must be inherently transient, suggesting that conductive modeling of thermal re-equilibration can provide bounds on the timing of hydration. Other processes by which thermal re-equilibration might occur (including advective transfer by melts or by flux of the volatile phase itself) would be more time-efficient than thermal conduction, so results derived from conductive modeling can be considered an upper-bound on the time from hydration to observation of a thermal perturbation in surface heat flow or Moho temperature.

We use estimates of the temperature change associated with crustal hydration (Ma & Lowry, 2017a, 2017b) derived from thermodynamical modeling using Perple_X (Connolly, 2009). Hydration reactions for a 1 wt-% water constituent release heat to produce 15–20°C of temperature increase in the upper crust, but

latent heat of fusion to produce melting in the garnet-grade lower crust reduces temperatures by up to 50°C. We note that larger temperature changes are possible if more water is present, as suggested by the complete consumption of garnet in Cordilleran lower crustal xenoliths (Jones et al., 2015). We model the crustal temperature change associated with three different wt-% hydration scenarios (Figure 38) using the crustal chemistries and thermodynamics described Ma & Lowry (2017a, 2017b), then forward model the conductive propagation of the geotherm perturbations to get changes in surface heat flow and Moho temperature as a function of time.

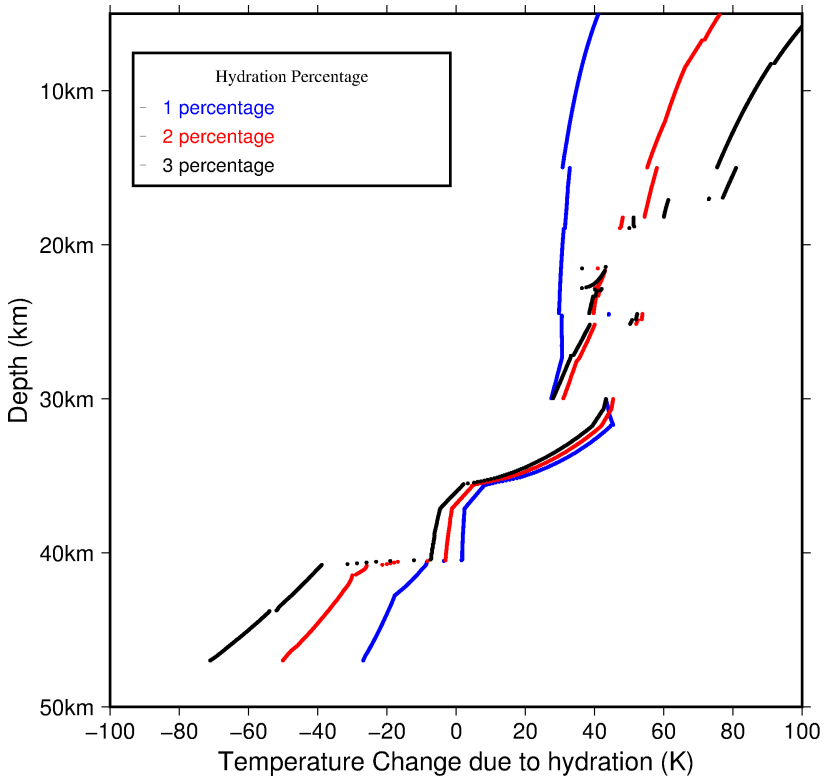

Figure 38: Crustal temperature changes that accompany enthalpy change during hydration. Blue, red and black curves reflect 1, 2 and 3 wt-% hydration respectively.

The initial geotherm used to model mineral thermodynamical reactions is a steady-state conductive geotherm that incorporates a depth-dependent crustal heat production model and temperature-dependent thermal conductivity (Lowry et al., 2000). However, for computational simplicity, the time-dependent modeling assumes linearity of the problem that would accompany uniform thermal transfer properties, and examines propagation only of the hydration-related perturbation relative to an unperturbed geotherm, ΔT = 0, in a 100 km-thick lithosphere with boundary conditions $\Delta T|_{x = 0} = \Delta T|_{x = 100\ \text{km}} = 0$ °C. We model changes in surface heat flow and temperature following hydration with the one-dimensional heat equation:

$$\kappa \frac{\partial T^2}{\partial^2 x} = \frac{\partial T}{\partial t} + Q(x,t) \qquad (1)$$

in which κ is thermal diffusivity (approximated to be 10^{-6}), and Q is heat production. Temperature is perturbed in the medium at time t = 0 (the time of hydration) as:

$$\Delta T\left(x, t = 0\right) = \Delta T_1\left(H\left(d_1\right) - H\left(d_2\right)\right) + \Delta T_2\left(H\left(d_2\right) - H\left(d_3\right)\right)$$

where H is the Heaviside function, ΔT_1 is the ~100°C exothermic temperature change from depths d_1 = 1 km to d_2 = 35 km, and ΔT_2 is the –100°C endothermic temperature change from depths d_2 = 35 km to d_3 = 45 km approximating temperature changes modeled in Ma & Lowry (2017a) (Figure 18d).

The perturbation of the geotherm and heat flow depends in part on the time- and depth-dependence of hydration reactions, in addition to the mechanism of

crustal heat transfer. We examine conductive thermal transfer here because it is the slowest process of heat transfer, giving an upper bound on the time from hydration reaction to a given observed change in Moho temperature, surface heat flow or elevation. We consider three cases: (1) an instantaneous hydration of the entire crust; (2) a pulse of hydration that diffuses through the crust, and (3) a uniform hydration of the crust that continues over a period of time. In the second case of a pulse diffusing through the crust, we assume the diffusion coefficient *D* of hydration in the crust to be ~10^{-7} m^2/s (Watson & Baxter, 2007). The characteristic diffusion distance $x \approx \sqrt{Dt}$ is then about 1.7 km/Myr, and the model approximates the hydration process as the aqueous phase moving through crust and absorbing or releasing heat as it goes.

4.3 Results

The geothermal profile attributed to thermal conduction was calculated at 0.2 Myr intervals. The heat source/sink due to enthalpy change as hydration diffuses upward through the crust expresses in the geotherm (Figure 39) as a pulse that travels upward through time and switches sign once it gets above the garnet phase transition. Temperatures are perturbed lower for the first 8 Myr, while heat is absorbed by melting of the lower crust. At 10 Myr the pulse diffuses above the garnet transition and the temperature perturbations are positive. By 15 Myr, the hydration front has moved above our assumed 15-km brittle-ductile transition and

temperature peaks at 50 °C near 17 km depth, after which the thermal transient decays. By 20 Myr, the perturbation is nearly zero.

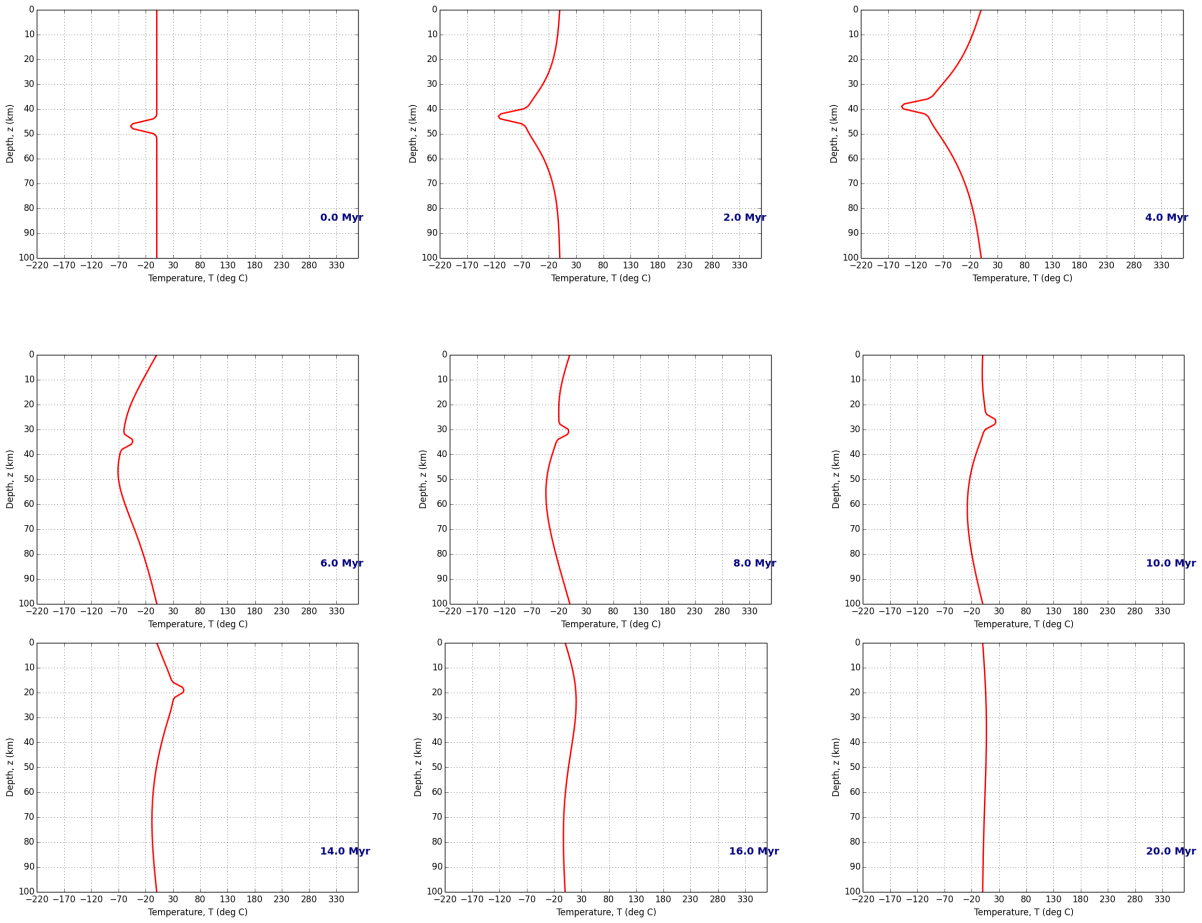

Figure 39: Geotherm perturbation by a pulse of hydration diffusing from the Moho to the surface. Thermal transfer assumes conduction only. The pulse on the profile represents the enthalpic heat source as hydration diffuses upward through the crust.

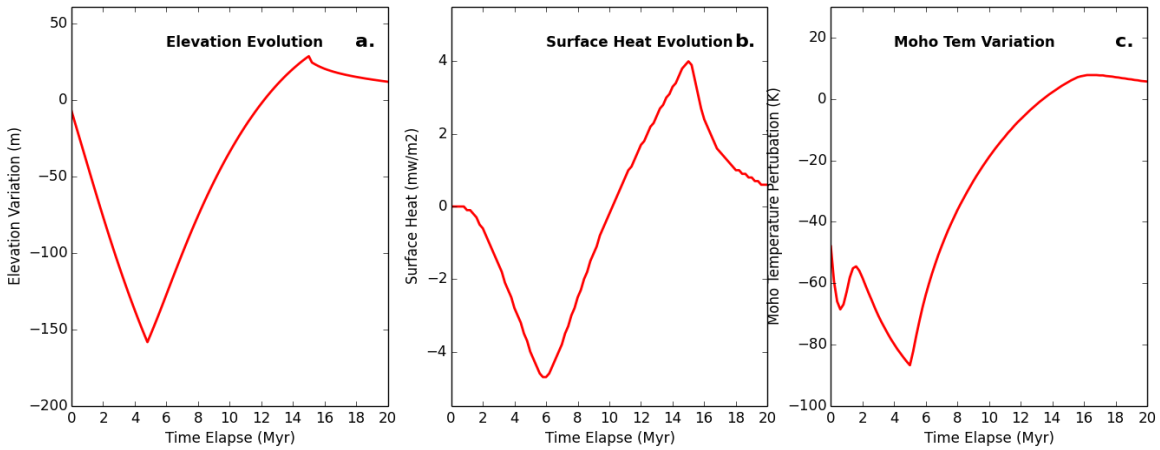

Figure 40: Evolution of (a) thermal elevation; (b) surface heat flow; and (c) Moho temperature associated with a diffusing hydration pulse (see Figure 39). Elevation changes consider only density changes associated with thermal expansion and neglect the density variation associated with mineral phase due to hydration.

The surface heat flow through time is shown in Figure 40. Heat flow decreases for the first 6 Myr while being perturbed by absorption of heat in the lower crust, reaching a nadir of –6.4 mW/m^2 at about 5.8 Myr. Heat flow then increases monotonically to a peak of 5.6 mW/m^2 at ~15 Myr, when the enthalpy change due to hydration ends and the heat flow transient returns to near zero. The maximum surface heat flow perturbation is a small fraction of the 20–50 mW/m^2 discrepancy between measured surface heat flow and heat flow predicted from Pn temperature found over most of the Cordillera (Berry et al., 2017) (Figure 41).

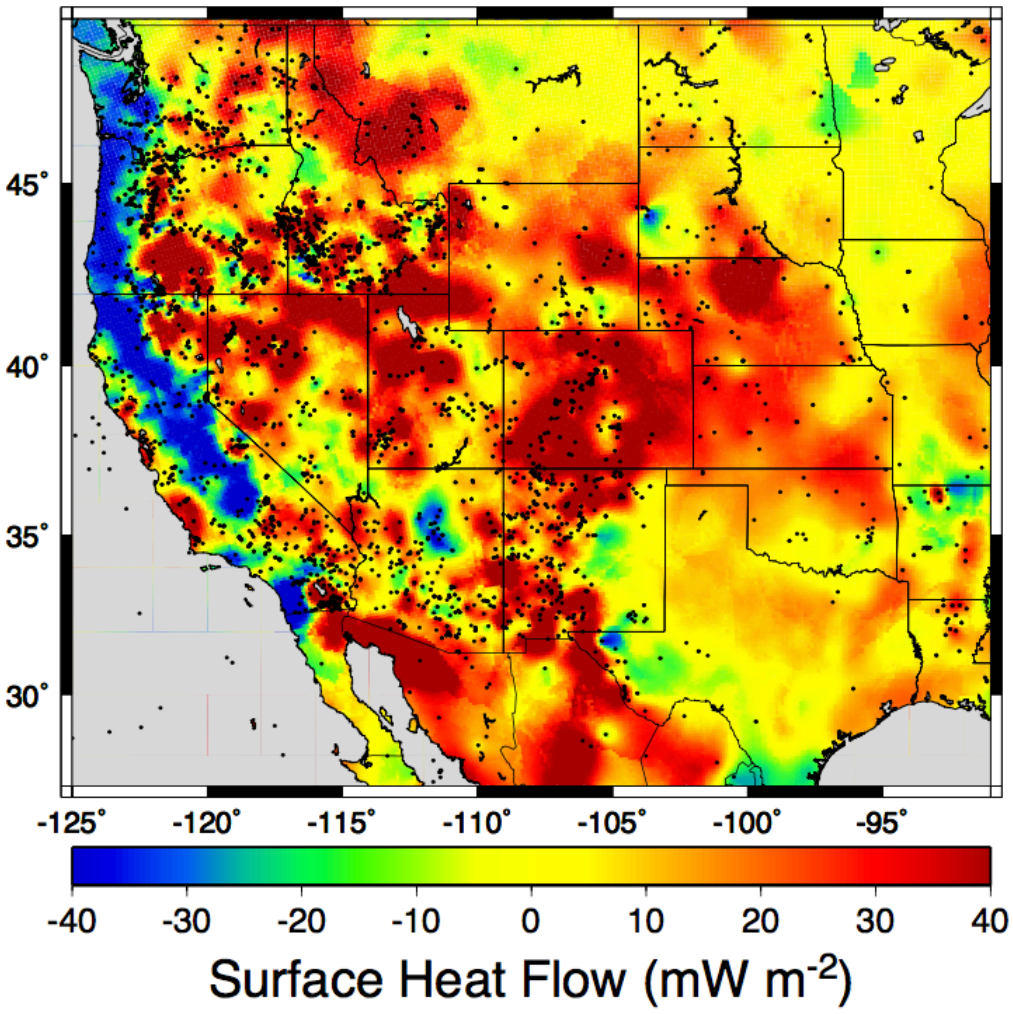

Figure 41: Surface heat flow anomaly in the western United States. A model of surface heat flow conductively projected to the surface from measurements of Moho temperature was subtracted from observed surface heat flow to approximate the perturbation of heat flow from a conductive steady-state (after *Berry et al*., 2017).

We also modeled the geothermal expression expected for a larger amount of hydration of 3 wt-% (Figure 42). Although the temperature perturbations are larger,

the temporal evolution is similar and the perturbation is nearly negligible after 20 Myrs. This calculation produces anomalous surface heat flow as high as 30 mW/m^2.

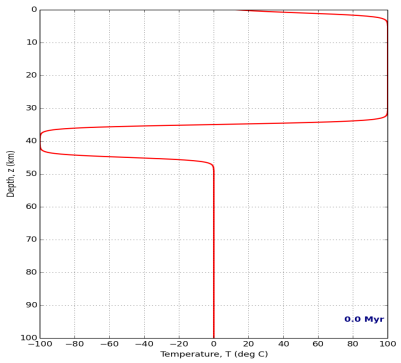

Figure 42: Geothermal pertubation given 3% hydration at time zero. The initial temperature variation is 100°C for upper crust and –100°C for upper crust.

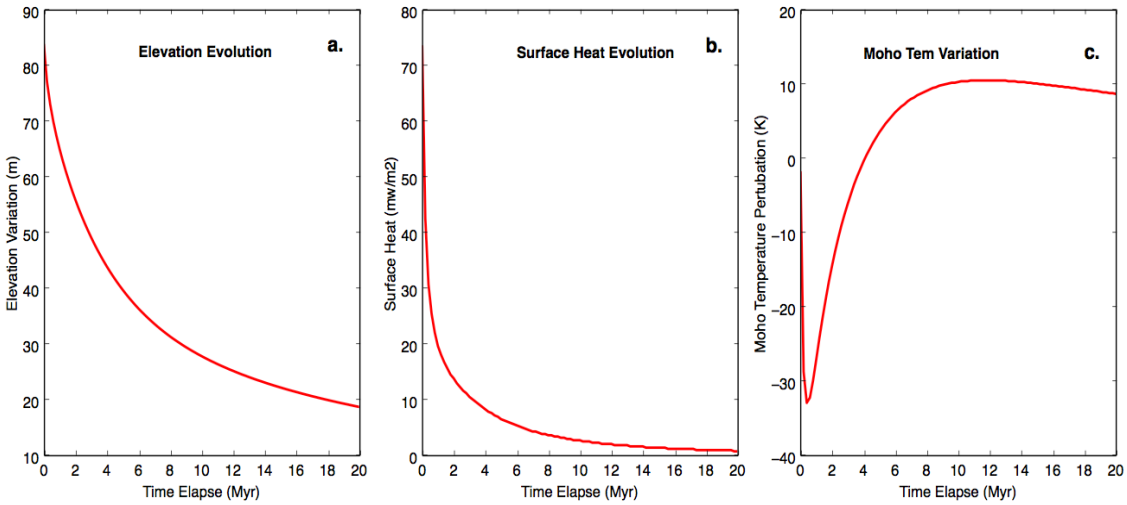

Figure 43: Evolution of (a) elevation, (b) surface heat flow and (c) Moho temperature due to 3 wt-% instantaneous hydration of the whole crust (see Figure 42).

4.4 Discussion

The pattern of anomalous surface heat flow in Figure 41 is related to thermal transients and advective transfer mechanisms in the crust (e.g., subduction heat mining along the Pacific coast), and the region of high heat flow closely matches the region thought to have been influenced by Laramide flat slab subduction. Our modeling calculations suggest hydration can both increase surface heat flow and decrease the Moho temperature, making it a strong candidate for explaining the perturbations. However, hydration can reproduce the observations only if a significant wt-% of hydration occurred and hydration reactions continued until the geologically recent past. We also note that, although advective processes were ignored in our calculations, advective heat transfer in this scenario would accompany diffusion of the aqueous constituent in the ductile regime, aqueous fluid flow in the higher permeability brittle upper crust, and migration of melts toward the surface. Advective heat transfer is generally more efficient than conductive transfer and so these would be expected to decrease the timescale of the transient perturbation.

Berry et al. (2015; 2017) also found that the non-steady-state perturbation of Moho temperature/heat flow is strongly correlated with elevation, with highest elevations occurring where the Moho is colder than expected. This is also consistent with lower crustal melting as a consequence of hydration, and the consumption of garnet by the melts would be expected to dominate the uplift (e.g., Jones et al.,

2015). The modeling described here can also be used to calculate the time-dependence of uplift, including that due to thermal perturbation, via:

$$\Delta h = \alpha_v \int_0^L \Delta T \, \rho_c / \rho_a \, dz$$

in which α_V is the coefficient of thermal expansion (3.5×10^{-5} K^{-1}), ρ_l is density of the lithosphere (depth-dependent), and ρ_a is density of asthenosphere (3230 kg/m^3 (Becker et al., 2014)).

Because the thermal expansion coefficient is small, the temperature changes are only of order tens to 100 degrees and the upper and lower crust experience temperature changes of opposite sign, the elevation changes expected from reaction enthalpy are small (Figure 43a). Density changes associated with hydrated mineral assemblages and melting predicted by the thermodynamical modeling (Connolly, 2009) will be much larger. Partial melt in the lower crust can be as high as 7% (Ma & Lowry, 2017). Assuming a melt density of 2500 kg/m^3, asthenospheric density of 3207 kg/m^3, lower crustal density of 3000 kg/m^3 and lower crustal thickness of 10 km, this would allow for a maximum $\Delta h = \int \Delta\rho / \rho_a \, dz$ of about 100 m.

4.5. Conclusions

Our thermal model indicates that conductive transfer of a thermal perturbation accompanying 3 wt-% hydration could increase surface heat flow quickly by 70 mW/m^2, then quickly drop to 10 mW/m^2 after 2 myr. The timing and amplitude of the

perturbation depends on the time history of hydration, but in our models the perturbation begins to decay quickly once the hydration ends, even when thermal transfer is purely conductive. Advective thermal transfer by fluid flux or melts could be expected to decrease the timescale and increase the amplitude of the transient thermal perturbations. The current discrepancy between Cordilleran heat flow measurements and heat flow predicted from Moho temperatures is 20–30 mW/m^2. If hydration is the mechanism for that discrepancy, part of it may be attributed to cooling of the Moho by the hydration process, and part to increased surface heat flow, but it would imply that hydration and melting of the lower crust must be an ongoing process in the Cordillera. Magnetotelluric imaging of the lower crust in the Cordillera reveals very low electrical resistivities that are almost certainly a result of melts (Meqbel et al*.,* 2014), which is consistent with this interpretation. Tomographic imaging also shows low shear velocity in the lower crust of these same regions (Lin et al., 2014; Porter et al., 2017). Ma & Lowry (2017a; 2017b) find low v_P/v_S throughout the Cordilleran lower crust that they interpret as evidence of past hydration by Farallon flat slab subduction. The expression of low bulk-crustal v_P/v_S was shown by Berry et al. (2015; 2017) to be nearly as strongly correlated with anomalously cold Moho temperatures as with elevation, so this would suggest that hydration reactions in crustal rocks, associated with aqueous fluids derived from Laramide flat-slab subduction of the Farallon plate, continues to the present day.

References

Becker, T. W., C. Faccenna, E. D. Humphreys, A. R. Lowry, & M. S. Miller (2014). Static and dynamic support of western United States topography. *Earth and Planetary Science Letters*, *402*, 234-246, https://doi.org/10.1016/j.epsl.2013.10.012.

Becker, T.W., A.R. Lowry, C. Faccenna, B. Schmandt, A. Borsa, & C. Yu (2015). Western U.S. intermountain seismicity caused by changes in upper mantle flow. *Nature, 524*(7566), 458-461. https://doi.org/10.1038/nature14867

Berry, M. A., A. R. Lowry, & D. L. Schutt (2015). Cold and wet at the roots of U.S. Cordilleran high elevation. Abstr. #T11C-2910, AGU Fall Meeting, San Francisco CA.

Berry, M. A., A. R. Lowry, D. L. Schutt, J. S. Buehler, & X. Ma (2017). Cold and wet at the roots of U.S. Cordilleran high elevation. In preparation.

Bennett, R. A., Wernicke, B. P., & Davis, J. L. (1998). Continuous GPS measurements of contemporary deformation across the northern Basin and Range province. *Geophysical Research Letters*, *25*(4), 563-566. https://doi.org/10.1029/98GL00128

Bird, P. (1988). Formation of the Rocky Mountains, western United States– A continuum computer model. *Science, 239*(4847), 1501-1507. https://doi.org/10.1126/science.239.4847.1501

Burchfiel, D. C., D. S. Cowan, & G. A. Davis (1992). Tectonic overview of the Cordilleran orogen in the western United States. In Burchfiel, W.C., P. W. Lipman M. L. Zoback (Eds.), *The Cordilleran Orogen: Conterminous U.S.*, Geological Society of America v. G-3, 407-480. https://doi.org/10.1130/DNAG-GNA-G3.407

Bürgmann, R., & G. Dresen (2008). Rheology of the lower crust and upper mantle: Evidence from rock mechanics, geodesy, and field observations. *Annual Reviews of Earth and Planetary Sciences*, *36*, 531-567. https://doi.org/10.1146/annurev.earth.36.031207.124326

Caldwell, W. B., Klemperer, S. L., Rai, S. S., & Lawrence, J. F. (2009). Partial melt in the upper-middle crust of the northwest Himalaya revealed by Rayleigh wave dispersion. *Tectonophysics, 477*(1), 58-65. https://doi.org/10.1016/j.tecto.2009.01.013

Demouchy, S., & Mackwell, S. (2006). Mechanisms of hydrogen incorporation and diffusion in iron-bearing olivine. *Physics and Chemistry of Minerals*, *33*(5), 347-355. https://doi.org/10.1007/s00269-006-0081-2

Hamilton, W. B. (1989). Crustal geologic processes of the United States. *Geological Society of America Memoirs, 172*, 743-782.

Humphreys, E. D. (1995). Post-Laramide removal of the Farallon slab, western United States. *Geology, 23*(11), 987-990. https://doi.org/10.1130/MEM172-p743

Humphreys, E. D., & Dueker, K. G. (1994). Western U.S. upper mantle structure. *Journal of Geophysical Research*, *99*(B5), 9615-9634. https://doi.org/10.1029/93JB01724

Humphreys, E., Hessler, E., Dueker, K., Farmer, G. L., Erslev, E., & Atwater, T. (2003). How Laramide-age hydration of North American lithosphere by the Farallon slab controlled subsequent activity in the western United States. *International Geology Review, 45*(7), 575-595. https://doi.org/10.2747/0020-6814.45.7.575

Jones, C. H., K. H. Mahan, L. A. Butcher, W. B. Levandowski, & G. L. Farmer (2015). Continental uplift through crustal hydration. *Geology*, *43*(4), 355-358. https://doi.org/10.1130/G36509.1

Kanda, R. V. S., A. R. Lowry, S. J. H. Buiter, & S. M. Ellis (2017). Flat-slab subduction from cradle to grave: the case for a strong lithosphere. In preparation.

Levander, A., Schmandt, B., Miller, M. S., Liu, K., Karlstrom, K. E., Crow, R. S., ... & Humphreys, E. D. (2011). Continuing Colorado Plateau uplift by delamination-style convective lithospheric downwelling. *Nature, 472*(7344), 461-465. https://doi.org/10.1038/nature10001

Levander, A., & Miller, M. S. (2012). Evolutionary aspects of lithosphere discontinuity structure in the western U.S. *Geochemistry, Geophysics, Geosystems, 13*(7). https://doi.org/10.1029/2012GC004056

Lin, F. C., Tsai, V. C., & Schmandt, B. (2014). 3-D crustal structure of the western United States: application of Rayleigh-wave ellipticity extracted from noise cross-correlations. *Geophysical Journal International*, *198*(2), 656-670. https://doi.org/10.1093/gji/ggu160

Liu, S., D. Nummedal, & L. Liu (2011). Migration of dynamic subsidence across the Late Cretaceous United States Western Interior basinin response to Farallon plate subduction. *Geology*, *39*(6), 555-558. https://doi.org/10.1130/G31692.1

Livaccari, R. F. (1991). Role of crustal thickening and tensional collapse in the tectonic evolution of the Sevier-Laramide orogeny, western United States. *Geology*, 19(11), 1104-1107. https://doi.org/10.1130/0091-7613(1991)019%3C1104:ROCTAE%3E2.3.CO;2

Lowry, A. R., & M. Pérez-Gussinyé (2011). The role of crustal quartz in controlling Cordilleran deformation. *Nature*, 471(7338), 353-357. https://doi.org/10.1038/nature09912.

Lowry, A. R., & Smith, R. B. (1995). Strength and rheology of the western US Cordillera. *Journal of Geophysical Research*, *100*(B9), 17947-17963. https://doi.org/10.1029/95JB00747

Ma, X., & A.R. Lowry (2017a). USArray imaging of continental crust in the conterminous United States. *Tectonics*, in press. https://doi.org/10.1002/2017TC004540

Ma, X., & A.R. Lowry (2017b). A two-layer mode of continental crust in the conterminous United States. In preparation.

Meqbel, N. M., Egbert, G. D., Wannamaker, P. E., Kelbert, A., & Schultz, A. (2014). Deep electrical resistivity structure of the northwestern US derived from 3-D inversion of USArray magnetotelluric data. *Earth and Planetary Science Letters, 402*, 290-304. https://doi.org/10.1016/j.epsl.2013.12.026

McMillan, M. E., Heller, P. L., & Wing, S. L. (2006). History and causes of post-Laramide relief in the Rocky Mountain orogenic plateau. *Geological Society of America Bulletin, 118*(3-4), 393-405. https://doi.org/10.1130/B25712.1

Newell, D. L., Jessup, M. J., Hilton, D. R., Shaw, C. A., & Hughes, C. A. (2015). Mantle-derived helium in hot springs of the Cordillera Blanca, Peru: Implications for mantle-to-crust fluid transfer in a flat-slab subduction setting. *Chemical Geology*, *417*, 200-209. https://doi.org/10.1016/j.chemgeo.2015.10.003

Pang, M., & D. Nummedal (1995). Flexural subsidence and basement tectonics of the Cretaceous western interior basin. *Geology*, 23(2), 173-176. https://doi.org/10.1130/0091-7613(1995)023%3C0173:FSABTO%3E2.3.CO;2

Porter, R., Hoisch, T., & Holt, W. E. (2017). The role of lower-crustal hydration in the tectonic evolution of the Colorado plateau. *Tectonophysics*, in press. https://doi.org/10.1016/j.tecto.2017.05.025

Roy, M., Jordan, T. H., & Pederson, J. (2009). Colorado Plateau magmatism and uplift by warming of heterogeneous lithosphere. *Nature, 459*(7249), 978-982. https://doi.org/10.1038/nature08052

Roy, M., Gold, S., Johnson, A., Osuna Orozco, R., Holtzman, B. K., & Gaherty, J. (2016). Macroscopic coupling of deformation and melt migration at continental interiors, with applications to the Colorado Plateau. *Journal of Geophysical Research, 121*(5), 3762-3781. https://doi.org/10.1002/2015JB012149

Schmandt, B., & Lin, F. C. (2014). P and S wave tomography of the mantle beneath the United States. *Geophysical Research Letters, 41*(18), 6342-6349. https://doi.org/10.1002/2014GL061231

Schmandt, B., Lin, F. C., & Karlstrom, K. E. (2015). Distinct crustal isostasy trends east and west of the Rocky Mountain Front. *Geophysical Research Letters, 42*(23). https://doi.org/10.1002/2015GL066593

Tikoff, B., & Maxson, J. (2001). Lithospheric buckling of the Laramide foreland during Late Cretaceous and Paleogene, western United States. *Rocky Mountain Geology, 36*(1), 13-35. https://doi.org/10.2113/gsrocky.36.1.13

Wagner, L. S., Fouch, M. J., James, D. E., & Hanson‐Hedgecock, S. (2012). Crust and upper mantle structure beneath the Pacific Northwest from joint inversions of ambient noise and earthquake data. *Geochemistry, Geophysics, Geosystems, 13*(12). https://doi.org/10.1029/2012GC004353

Watson, E. B., & Baxter, E. F. (2007). Diffusion in solid-Earth systems. *Earth and Planetary Science Letters, 253*(3), 307-327. https://doi.org/10.1016/j.epsl.2006.11.015

Whitmeyer, S. J., & K. E. Karlstrom (2007). Tectonic model for the Proterozoic growth of North America. *Geosphere, 3*(4), 220-259, https://doi.org/10.1130/GES00055.1.

Williams, M. L., et al. (2010), *Unlocking the Secrets of the North American Continent: An EarthScope Science Plan for 2010–2020*.

CHAPTER 5

SUMMARY

The Gyr history of accretion and magmatism recorded in the North American continental crust, coupled with the current dynamics of the western U.S. Cordillera, afford an ideal laboratory for studies of processes related to tectonics, mass transfer and lithospheric dynamics. Using the densely-sampled seismic data collected by EarthScope's Transportable Array, permanent regional seismic networks, and temporary deployments of PASSCAL and FLEXArray instruments, we implemented an advanced joint inversion algorithm to model crustal structure and bulk v_P/v_S. Both thickness and v_P/v_S were estimated from joint inversion of Bouguer gravity, seismic receiver functions and spatial statistics. The crustal layer thicknesses are consistent with results from seismic refraction profiling and other studies of TA data, and they delineate geological province boundaries. The crustal v_P/v_S measured for both single layer and two-layer models suggests, based on modeling of of mineral thermodynamics, that the crust of the U.S. Cordillera has been modified by hydration following Laramide flat-slab subduction. Gravity anomalies associated with crustal thickness, bulk v_P/v_S and geothermal variations are calculated and suggest that compositional variations within the crust dominate the lithospheric mass variation. The lowered v_P/v_S expected of crustal mineral assemblages and patterns of crustal v_P/v_S variation we find in the western United States supports inferences based on xenolith sampling that high Cordilleran elevations are partially supported by decreased density of hydrated crust (Jones et al., 2015). Simulations of conductive

thermal transfer of the enthalpy changes associated with hydration indicate that hydration is ongoing and that advective transfer by volatile constituents and/or partial melt contributes to high surface heat flow anomalies in the Cordillera.

In Chapter 2, we modeled crustal thickness and bulk v_P/v_S over the conterminous United Stated, extending an earlier analysis by Lowry & Pérez-Gussinyé (2011). The main differences from the earlier study is an approximate doubling of the area covered by the TA to that time, the implementation of a cross-correlation analysis relating synthetic and observed receiver functions instead of amplitude stacking (Zhu & Kanamori, 2000; Crotwell & Owens, 2005), and implementation of a stochastic inversion to estimate density parameters associated with Moho depth, bulk composition and thermal variation. The final density parameters from our joint inversion is much more similar to those expected based on laboratory and other geophysical analyses of rock properties. The crustal thickness variations show strong relationships to surface geology and are consistent with results from other passive seismic studies using different approaches and seismic refraction surveys (Smith et al., 1989; Pakiser, 1989; Braile et al., 1989; Schmandt et al., 2015; Shen & Ritzwoller, 2016). The western U.S. has predominantly thin crust (less than 40 km) with the exception of the Cascade and Sierra-Nevada ranges. The crust in the stable cratonic middle and eastern U.S. is generally thicker, with the thickest (>50 km) crust under the Middle and Southern Rocky Mountains and Appalachian Highlands. Eastern North and South Dakota, the Mississippi embayment and the Atlantic coast all have relatively thin crust. Crustal v_P/v_S is

lowest in the Basin and Range and southern Rocky Mountains of the Cordillera, while the Snake River Plain, Columbia Plateau, Northern Interior Plain and Mid-Continent rift is characterized by high v_P/v_S. We interpret low v_P/v_S to result from abundant quartz that thermodynamical modeling of mineral formation suggests is favored by hydration. Regions with low v_P/v_S in the western U.S. are also characterized by high surface heat flow and a much cooler Moho than the heat flow would predict. We interpret tectonism in the western U.S. to be significantly modified by hydration following Farallon subduction, consistent with earlier analyses of xenolith samples (Jones et al., 2015).

Chapter 3 was an extension of the method developed for our one-layer model to estimate thickness and v_P/v_S of a more complex two-layer crustal model. We used a very similar procedure to model the thickness and v_P/v_S of the upper and lower crust. The synthetic model used results of the prior inversion for a one-layer model to reduce the parameter-space to thickness and v_P/v_S of the upper crust (with lower crustal thickness and velocity being that required to match the total one-layer crustal properties). The joint inversion of seismic, gravity and spatial statistics was run for more than 50 iterations. The final density parameters were slight different than those of the one-layer analysis, with about 100 kg/m^3 lower bulk crustal compositional density parameter $\partial\rho/\partial\kappa$, and about 12 kg/m^3 higher Moho density contrast. The model finds the thickest upper crust in the Rocky Mountains and Appalachian Highlands. Interestingly, the Great Plains region of the U.S., including North Dakota, South Dakota and Nebraska, is an arcuate-shaped region of thin upper crust. Most

of the upper crust has low v_P/v_S excepting the Columbia Plateau, Snake River Plain and Northern Interior Plains. The lower crust is thinnest in the extending provinces and near the western and eastern coasts, with thickness in the central U.S. ranging from 20–30 km. v_P/v_S of the lower crust is generally much higher than in the upper crust. In the Cordilleran western U.S., the change in v_P/v_S between the upper and lower crust is small whereas it is ~0.15–0.25 in stable crust of the central and eastern U.S. Thermodynamical modeling of the *P-T-X* dependence of v_P/v_S suggests the mid-crustal impedance contrast is more likely to represent a chemical boundary than a phase boundary. Extremely low v_P/v_S (consistent with bulk crustal v_P/v_S of the one-layer model) is observed in the lower crust of the Cordilleran extending provinces including the northern Rocky Mountains, Basin and Range and Rio Grande rift. Xenolith sampling of these regions suggest hydration of the deep crust (Jones et al., 2015) consistent with inferences from our two-layer model.

Chapter 4 describes a simulation of crustal conductive heat transfer associated with hydration processes inferred in the earlier chapters. The discrepancy between observed surface heat flow and heat flow predicted from Pn-derived Moho temperatures in the western U.S. Cordillera is generally 20–50 mW/m^2. Our modeling of conductive thermal transfer of temperature anomalies expected from hydration reaction enthalpy suggests that the surface heat flow perturbation ranges from 5 to 80 mW/m^2 depending on the time-evolution and total amount of hydration assumed, but the largest observed heat flow perturbations would require the hydration event to have occurred in the geologically very recent

past (<10 Myr). Advective processes associated with hydration (including upward flux of the volatile constituent and of melts produced in the lower crust) can amplify the heat flow perturbation but also would shorten the timescale of transient thermal perturbation.

References

Braile, L. W., W. J. Hinze, R. R. B. Von Frese, & G. R. Keller (1989). Seismic properties of the crust and uppermost mantle of the conterminous United States and adjacent Canada. *Geological Society of America Memoirs, 172*, 655-680, doi:10.1130/MEM172-p655. https://doi.org/10.1130/MEM172-p655

Crotwell, H. P., & T. J. Owens (2005). Automated receiver function processing, *Seismological Research Letters*, *76*(6), 702-709, doi:10.1785/gssrl.76.6.702. https://doi.org/10.1785/gssrl.76.6.702

Jones, C. H., K. H. Mahan, L. A. Butcher, W. B. Levandowski, & G. L. Farmer (2015). Continental uplift through crustal hydration. *Geology, 43*(4), 355-358. https://doi.org/10.1130/G36509.1

Lowry, A. R., & M. Pérez-Gussinyé (2011). The role of crustal quartz in controlling Cordilleran deformation. *Nature, 471*(7338), 353-357, https://doi.org/10.1038/nature09912

Pakiser, L. C. (1989). Geophysics of the Intermontane system. *Geological Society of America Memoirs, 172*, 235-248, doi:10.1130/MEM172-p235. https://doi.org/10.1130/MEM172-p235

Schmandt, B., Lin, F. C., & Karlstrom, K. E. (2015). Distinct crustal isostasy trends east and west of the Rocky Mountain Front. *Geophysical Research Letters*. https://doi.org/10.1002/2015GL066593

Shen, W., & Ritzwoller, M. H. (2016). Crustal and uppermost mantle structure beneath the United States. *Journal of Geophysical Research*. https://doi.org/10.1002/2016JB012887

Smith, R. B., W. C. Nagy, K. A. S. Julander, J. J. Viveiros, C. A. Barker, & D. G. Gants (1989). Geophysical and tectonic framework of the eastern Basin and Range-Colorado Plateau-Rocky Mountain transition. *Geological Society of America Memoirs, 172*, 205-234. https://doi.org/10.1130/MEM172-p205

Zhu, L., & H. Kanamori (2000). Moho depth variation in southern California from teleseismic receiver functions. *Journal of Geophysical Research, 105*(B2), 2969- https://doi.org/10.1029/1999JB900322

APPENDICES

Appendices

Table 3

Sources of the solution model used in Perple_X modeling.

Solution	Symbol	Source
Amphibole	Amph (DHP)	Dale et al. (2000)
Biotite	Bio (HP)	Powell & Holland (1999)
Clinopyroxene	Cpx (HP)	Holland & Powell (1996)
Orthopyroxene	Opx (HP)	Holland & Powell (1996)
Garnet	Gt (HP)	Holland & Powell (1998)
Feldspar	Pl (I1,HP), Fsp (C1)	Holland & Powell (2003)
Melt	Melt (HP)	Holland & Powell (2001); White et al. (2001)
Spinel	Sp (HP)	Holland & Powell (1998)

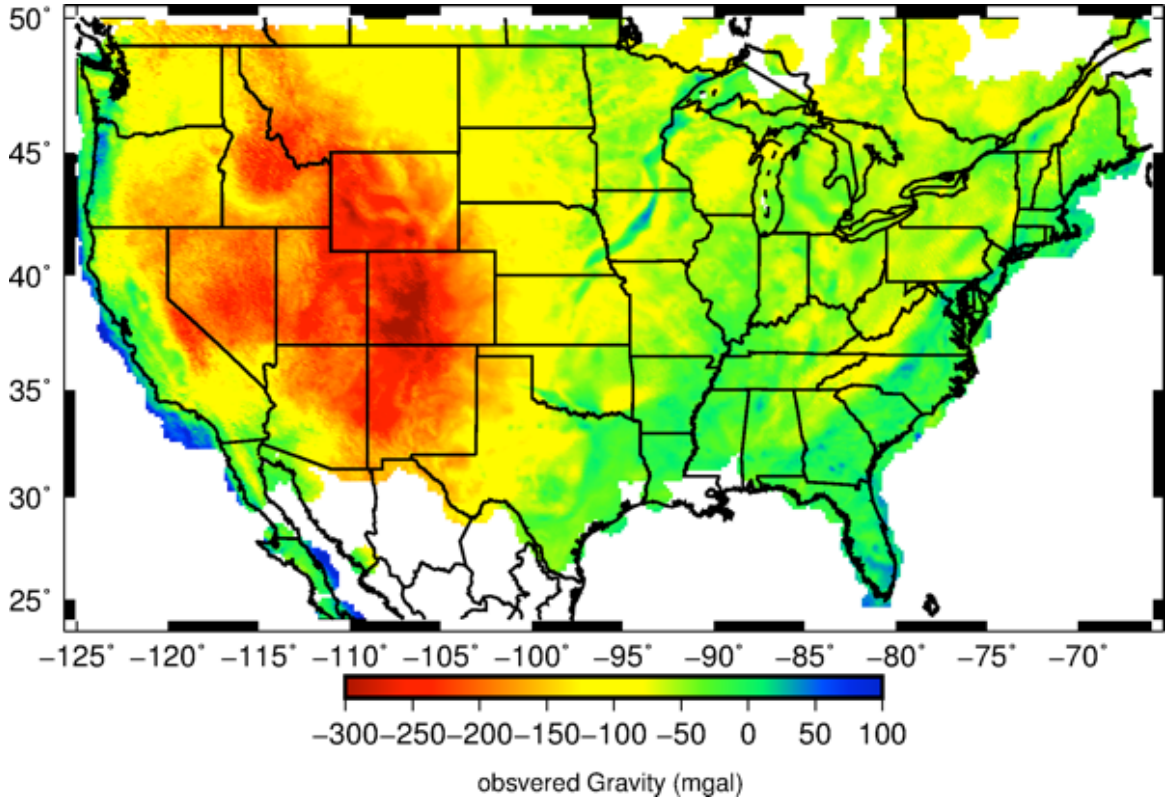

Figure 44: Observed Bouguer gravity of the United States.

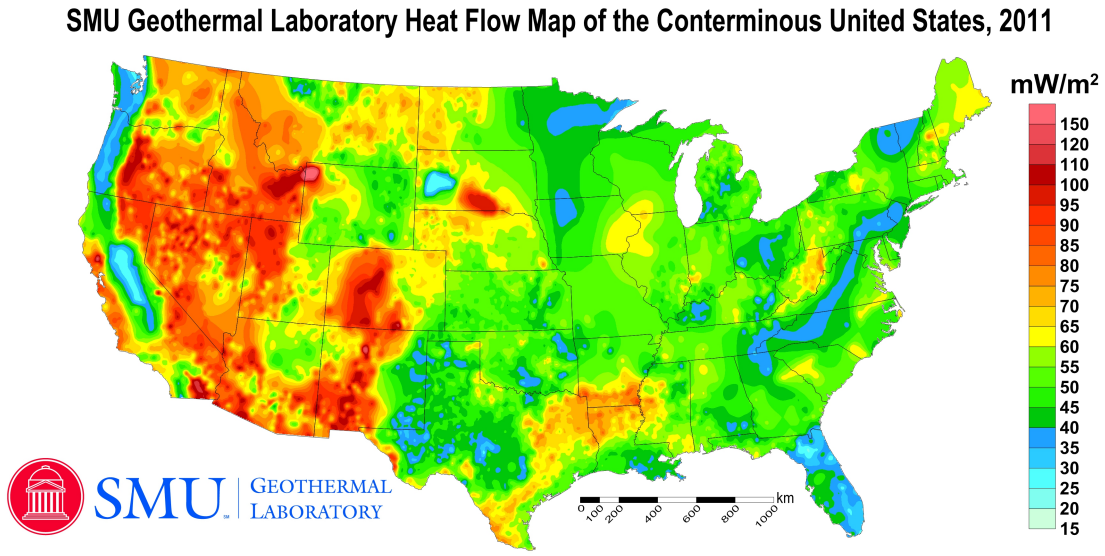

Figure 45: Heat flow map of U.S. (Blackwell et al., 2011). The southern Rocky Mountains has high heat flow coincident with lower averaged v_P/v_S ratio.